A dissertation for doctor's degree

Combined Experimental and Computational Studies on Electrochemical Oxidation of Formic Acid over Pt- and Pd-Based Alloys

The Graduate School

University of Ulsan

Department of Chemical Engineering

Lijun Sui

Combined Experimental and Computational Studies on Electrochemical Oxidation of Formic Acid over Pt- and Pd-Based Alloys

Author: Lijun Sui
Speciality: Chemical Engineering
Supervisors: Prof. Seung Hyun Hur, Prof.Wei An
Finished time: May 2020

A dissertation for doctor's degree

University of Ulsan

Combined Experimental and Computational Studies on Electrochemical Oxidation of Formic Acid over Pt-and Pd-Based Alloys

Thesis for the degree of Doctor of Philosophy by

Lijun Sui

has been approved

Committee Chair Prof. Kang, Sung-Gu

Committee Member Prof. Chung, Jin-Suk

Committee Member Prof. An, Wei

Committee Member Prof. Hur, Seung-Hyun

Committee Member Prof. Choi, Won-Mook

Department of Chemical Engineering

University of Ulsan

June 2020

Abstract

Direct formic acid fuel cell (DFAFC) can be regarded as the clean and green energy source, in which develop high-efficiency and cheap anode catalysts is important. Palladium and platinum are well noted as anode catalyst for promoting electrochemical oxidation of formic acid (FAO) in DFAFC thanks to their good performance. In here, we study the Pt- and Pd-based alloy catalysts for FAO.

The PtBi/C and PtBiPd/C electrocatalysts were synthesized via the irreversible adsorption of Pd and Bi ions precursors on commercial Pt/C catalysts. XRD and XPS revealed the formation of an alloy structure among Pt, Bi, and Pd atoms. The current of direct formic acid oxidation increased ~ 8 and 16 times for the PtBi/C and PtBiPd/C catalysts than commercial Pt/C. In addition, the increased ratio between the current of direct formic acid oxidation and the current of indirect formic acid oxidation for the PtBi/C and PtBiPd/C catalysts suggest that the dehydrogenation pathway is dominant with less CO formation on these catalysts. Furthermore, Pd modified the BiPt/C improve the potential of Bi leaching to keep catalysts activity.

We have found that RuPdPt/C has a best performance with less Ru and a large number of Pd than the PtPd/C and Pt/C by experiments results with the density functional theory (DFT), in which RuPdPt/C not only improve the direct formic acid oxidation, but also increase current of indirect formic acid oxidation by the OH of water dissociation as the oxidizing agent.

Furthermore, using combined approach of DFT calculations and microkinetic modelling (MK), we investigated the fundamental aspects of FAO catalysed by bimetallic M@Pd(111) single-atom surface alloys (where M = Fe, Cu, Zn, Ru, Co, Mo). Our results suggest that M@Pd(111) are highly stable and outperforms Pd(111) for FAO via primarily the direct mechanism: HCOOH → *HCOO (formate) → $CO_2 + 2H^+ + 2e^-$. It is revealed that the decoordination of *HCOO from bidentate to monodentate adsorption mode (i.e., *bH$_u$COO → *mH$_d$COO) followed via the facile carbonyl-H abstraction forming $CO_2 + (H^+ + e^-)$ could be the potential-determining steps. Moreover, Mo@Pd(111) is predicted to be the most promising bimetallic Pd-based catalyst for FAO based on the weakest *CO binding and the strongest *OH binding with alloyed Mo, which therefore can be used as an effective descriptor for designing FAO catalysts with high activity.

For studying the effects of ensemble Mo on the Pd(111) surface, We added the explicit solvation model is closer to the real condition of FAO. Monomers, dimers, trimers, and tetramers are selected as typical Mo ensembles. Meanwhile, interval and adjacent Mo atom have been investigated, we have verified that interval Mo atoms decorated have a better per-

formance than adjacent structures. Mo_1Pd is the best profit catalyst for FAO as a direct reaction by intermediates *HCOO, $bH_uCOO \rightarrow *mH_dCOO$ as potential-determining step (PDS). Meanwhile, the binding strength of OH can be a descriptor to redefect the barrier of PDS, Mo_1Pd is a potential catalyst due to the moderate binding energy of OH.

In this work, Pt-based and Pd-based tri-metallic and di-metallic metal even single atom catalysts were studied by experiment and DFT calculation, we found that Pt or Pd can be modified by other metal can get higher performance for FAO due to the electronic, geometric, and third body effects, PtBiPd/C and RuPdPt/C the promising tri-metallic catalysts and the single atom catalyst have valuable catalytic activity, Mo, Ru, Fe, Co, Ni can be combined with Pd as he potential catalyst for FAO.

Key word: FAO, Pd-based, Pt-based, PtBiPd/C, RuPdPt/C, Mo@Pd(111), catalytic activity, DFT , experiments.

Attestation

I understand the nature of plagiarism, and I am aware of the University's policy on this.

I certify that this dissertation reports original work by me during my University project except for the following (*adjust according to the circumstances*):

Signature Sui Lijun/ 수리준 **Date** 2020.07.03

Acknowledgements

This work was supported by NSFC (21673137), STCSM (16ZR1413900) and SUES(0234-A1-0902-19-01603). The DFT calculations were performed using resources of the Center for Functional Nanomaterials, which is a U.S. DOE Office of Science Facility, and the Scientific Data and Computing Center, a component of the Computational Science Initiative, a Brookhaven National Laboratory under Contract No. DE-SC0012704. SHH acknowledges support from the Basic Science Research Program through the National Research Foundation of Korea (NRF) funded by The Ministry of Science, ICT and Future Planning (2019R1A2B5B02069683).

Table of Contents

List of Figures

1 Introduction

We are interested in developing new green energy resources due to depletion of energy, environmental pollution, as well as the cost these factors are not ignored. Fuel cells provide cheaper, high-efficiency and non-pollution raw material and various new materials have been researched, such as solar energy, windy energy and tidal energy in which direct liquid fuel cells are wildly studied, for instance, methanol, ethanol or formic acid, etc. The electrodes of anode oxidation and cathode reduction still are tough points, where the electrode catalysts play an important role has been modified continuously. The catalyst reaction mechanism has been explored by experiment analysis and theoretical calculation. Modified Pt-based and Pd-based electrode catalysts have a good prospect to study further.

1.1 Direct formic acid fuel cell

Direct formic acid fuel cells (DFAFCs) is proton exchange membrane fuel cells where chemical transfer to electric energy via anode formic acid oxidation (FAO) and cathode oxygen reduction, the final production is water and carbon dioxide at low temperature as shown in Figure 1.1. The anode, cathode and total reaction equation and potential as

Anode: $HCOOH \rightarrow CO_2 + 2H^+ + 2e^-$ $E^0 \sim -0.25$ V (vs. SHE)

Cathode: $1/2O_2 + 2H^+ + 2e^- \rightarrow H_2O$ $E^0 = 1.23$ V (vs. SHE)

Overall: $HCOOH + 1/2O_2 \rightarrow CO_2 + H_2O$ OCV ~1.48V

DFAFCs was putted forward by Savinell group in 1996 [1], Richard Masel's group found the formic acid is the better fuel and made the first machine of DFAFCs [2]. Hereafter, the reports have been increased, in which their applications include small, portable electronics such as phones and laptop computers as well as larger fixed power applications and vehicles.

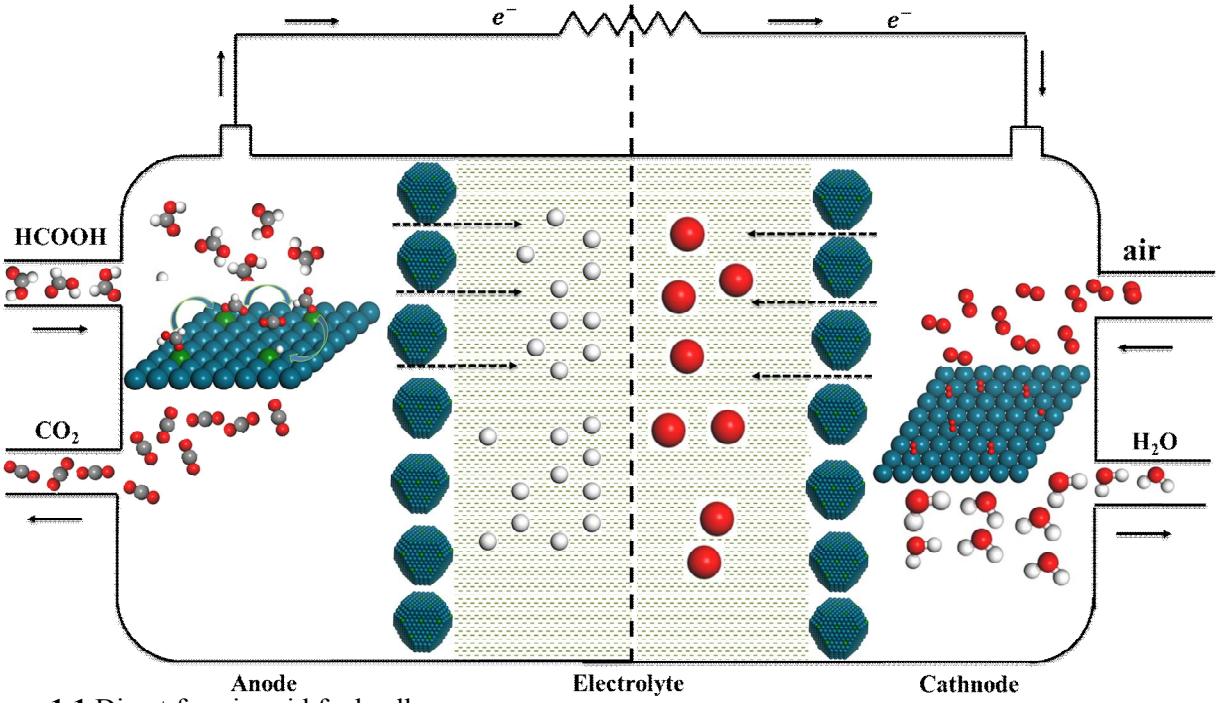

Figure 1.1 Direct formic acid fuel cell

1.1.1 Formic acid

Formic acid (methanoic acid) is the simplest structure of alkyl carboxylic acid, which can be found from some insects in nature, such as ant. Formic acid is extensively used in industrial production and the capacity of formic acid climbed to 137.1 million tons in 2017 what can be utilized in fabric processing, leather tanning, textile printing and dyeing and grass silage, also can be used as metal surface treatment agent, rubber additives and industrial solvents. Various formate esters acridine dyes and formamide series pharmaceutical intermediates are synthesized in organic synthesis. Its downstream consumption is mainly used for pharmaceutical, chemical, pesticide, rubber products, etc.

Formic acid (HCOOH) is a colourless, clear liquid and can be miscible with water, ethanol, ether and glycerol, etc. It is flammable and highly corrosive with intense and pungent smell. Solved with water but dissolved in hydrocarbons. The freezing point diagram for the formic acid binary mixture has a eutectic point at -48.5 ℃ and 41.0 mol% of HCOOH. The basic physical properties are shown in Table 1.1.

Formic acid is relatively stable in room temperature, unstable decomposition was divided in dehydration (CO, H_2O) or dehydrogenation (CO_2, H_2) [3] So it is a superior kind of hydrogen storage material. Esterification and amidation are typical chemical as same as other aliphatic carboxylic acids. Formic acid comes from a wide range of sources, in which production mainly are from naphtha partial oxidation and methanol carbonylation/methyl formate hydrolysis [4]. Recently, biomass and CO_2 hydrogenation have been studied extensively [5].

Table 1.1 Physical properties of pure formic acid

Property	Value
molecular weight	46.026
melting point, ℃	8.4
boiling point, ℃	100.7
density, g/cm^3 at 20℃	1.220
refractive index n_{D}^{20}	1.3714
surface tension at 20℃, mN/m(= dyn/cm)	37.67
viscosity at 20℃, mPa · s(= cP)	1.784
specific conductance, Ω/m	$6.08*10^{-3}$
dielectric constant at 20℃	57.9
latent heat of vaporizationat boiling point, kJ/kg[a]	483
free energy of formation, ΔG_f^0 (g), kJ/kg[a]	-351
enthalpy of formation, ΔH_f^0 (g), kJ/kg[a]	-377

1.1.2 Fundamentals of DFAFCs chemistry

The formic acid has a high open circuit voltage (OCV) up to 1.48V, this means a higher electromotive. In the direct liquid fuel cell, formic acid is a small organic molecule that do not need complicated catalyst reaction. Formic acid is non-toxic and diluted formic acid is on the U.S. Food and Drug Administration list of food additives. It is easier to transfer due to convenience store [3]. Formic acid does not cross over the polymer membrane result in its higher efficiency. The theoretical energy density of formic acid is determined as: $2F\times OCV\times(MW)^{-1}$. From the molecular weight MW (kg mol^{-1}), open circuit potential OCV (V) and the Faraday constant (F=96,485C mol^{-1}), formic acid has the intrinsic energy density of 1725Wh kg^{-1}. Considering the density of this liquid (1.22kg L^{-1}), the theoretical energy density of formic acid can also be expressed as 2104Wh L^{-1} [4]. Formic acid alter the chemical energy to the electric energy by electronic and proton transport within the electrodes of fuel cell, in which convert formic acid and oxygen into carbon dioxide and water to produce energy [5].

1.1.3 Cathnode electro-reduction of direct formic acid fuel cell

Direct formic acid fuel cell uses the air at cathode side like all polymer electrolyte membrane fuel cell, oxygen reduction reaction (ORR) by transfer 4 electrons at cathode. The reaction acidic aqueous solution dissociative mechanism follow as [6]:

$$O_2 + 4(H^+ + e^-) \rightarrow 2{}^*O + 4(H^+ + e^-) \rightarrow 2{}^*OH + 2(H^+ + e^-) \rightarrow H_2O$$

Associative mechanism:

$$O_2 + 4(H^+ + e^-) \rightarrow {}^*OOH + 3(H^+ + e^-) \rightarrow {}^*O + {}^*OH + 3(H^+ + e^-)$$

$$\rightarrow {}^*O + H_2O + 2(H^+ + e^-) \rightarrow {}^*O + H_2O + 2(H^+ + e\text{-})$$

$$\rightarrow {}^*OH + H_2O + (H^+ + e^-) \rightarrow H_2O$$

In non-aqueous aprotic solvents and/or in alkaline solutions, the 1-electron reduction pathway from O_2 to superoxide (O_2^-) can also occur. In the alkaline aqueous solution as:

$$O_2 + H_2O + 4e^- \rightarrow 4OH^-$$

$$O_2 + H_2O + 2e^- \rightarrow OH_2^- + OH^-$$

$$OH_2^- + H_2O + 2e^- \rightarrow 3OH^-$$

In the non-aqueous aprotic solvents as:

$$O_2 + e^- \rightarrow O_2^-$$

$$O_2 + e^- \rightarrow O_2^{2-} + OH^-$$

In the DFAFCs, the 4-electrons transfer is easier than 2-electrons and 1-electron. Oxygen is extremely stable in the nature lead to getting proton oxygen is difficult in the whole fuel cell reaction, so the slow oxygen reduction was studied uninterruptedly as the technological difficulty. ORR need high loading Pt (~0.4 mg cm^{-2}) and Pd to achieve catalyze the reaction due to they are the best catalyst at the cathode [7]. The development of less cost and high-efficiency catalysts is an important research for DFAFCs cathode, in which include alloys, core-shell structure, transition metal oxidation and chalcogenides, and carbon based non-noble metal composite catalysts. On another hand, increasing the catalyst performance were studied by modified the carbon-support [8, 9]. But Pt still have a high price, but non-Pt, nanoparticle-based and molecular-level catalysts have been studied increasingly due to high catalytic activities such as: cheap metal (Fe, Cu) and relatively expensive metal (Ag, Au) [13].

1.1.4 Anode electro-reduction of direct formic acid fuel cell

Electro-oxidation of formic acid occurs at the anode side of fuel cell, the mechanism of reaction is controversial due to HCOOH small and flexible on the surface of catalysts, but it is widely believed that has dual pathways as direct oxidation reaction and indirect oxidation, the direct reaction equation is:

$HCOOH \rightarrow CO_2 + 2H^+ + 2e^-$

They suggested that the oxidation current of FA through the direct pathway may be described by the following equation [10]:

$$i \propto -\frac{\mathrm{d}\theta_{formate}}{\mathrm{d}t} = k\theta_{formate}\left(1-\theta_{CO}-2\theta_{formate}\right)$$

indirect reaction equation forms the CO firstly further oxidation to CO_2 as:

$HCOOH \rightarrow {}^*CO + H_2O$

$H_2O \rightarrow {}^*OH + H^+ + e^-$

${}^*CO + {}^*OH \rightarrow CO_2 + H^+ + e^-$

The direct formation of CO_2 is benefited for the fuel cell performance rather formation of CO will make the catalyst poison and less the efficiency of cell. The dissociation mechanism of HCOOH have been reported that routes formate (HCOO) as the main intermediate by DFT calculation [11] and are observed by using surface-enhanced infrared absorption spectroscopy in the attenuated total reflection mode (ATR-SEIRAS) [12] The HCOOH oxidation by 2 steps follow as:

$HCOOH \rightarrow {}^*HCOO + H^+ + e^-$

$^{*}HCOO \rightarrow CO_2 + H^+ + e^-$

With the development of research, HCOO as intermediate existent of structure has been discussed, in which were divided into bidentate formate (*b*HCOO) and decoordination monodentate formate (*m*HCOO), the equation can be written detail as [13-15]:

$HCOOH \rightarrow {}^{*}bHCOO + H^+ + e^- \rightarrow {}^{*}mHCOO + H^+ + e^-$

$^{*}HCOO \rightarrow CO_2 + H^+ + e^-$

On the other hand, carboxy (*COOH) species is also kind of intermediate for formation of CO_2 and CO, though CO can be created by HCOO, COOH is easier to form CO rather than HCOO [16, 17]. It has been confirmed that HCOOH transfer 2-electrons directly on the surface of calalysts there the adsorption of HCOOH in a CH-down configuration, which is a reactive precursor leading to CO_2 [18]. It is also illustrated that interaction between 2 molecules of HCOOH on the ensemble closed 3 Pt atoms as [19]:

$2\ HCOOH \rightarrow CO_2 + CO + H_2O + 2H^+ + 2e^-$

$CO + H_2O \rightarrow CO_2 + 2H^+ + 2e^-$

There is no universal conclusion as result in HCOOH molecule is small and reaction is very fast so that It is difficult to capture for the real process of the FAO. Anode catalysts of formic acid electro-oxidation

1.2 Catalysts of formic acid oxidation

1.2.1 Pt-based catalyst

Formic acid as fuel for DFAFCs were observed in 1996, gradually pay attention to the research of formic acid until 2002 when the Masel's group presented FAO has a high electrocatalytic activity on the Pt surface [2]. FAO includes two steps electron transaction that is broken H-O and C-H bonds, in which O-H is broken easily in the acid-based equilibrium around pH=4 owing to the HCOOH is a weak acid with pK_a=3.75 [20]. However, C-H cleavage is probably the most difficult step, Pt promote dehydrogenize because of the strong adsorption energy with hydrogen [21]. Some studies are represented the HCOO is intermediate by the ATR-SEIRAS [20], and there remains an on-going debate about intermediate of FAO, in which COOH as the intermediate instead of HCOO due to the strong adsorption energy of Pt-C [10]. Meanwhile, COOH is a critical species to form CO. Therefore, Pt has an excellent property for carbon adsorption lead to CO-poison. The formation of CO cover on the catalystic surface and take up the activity sites even make catalyst lost the activity and decreasing the cell performance [22]. Moreover, CO is created at the low potential rather oxidized at high potential [23]. To explore the structure sensitivity of this reaction on the fcc metals, Pt(100)

facet also was studied that the open facets of Pt are more energy-efficient (i.e. require less overpotential) for formic acid electrooxidation when compared to their close-packed facets. The order is Pt(111) < Pt(100) < Pt(110) [17]. But Pt (111) lowest miller index and good performance still was studied.

However, high concentrate of Pt is expensive noble metal and CO of formation decreasing the activity and stability. Bimetallic and of various forms (e.g., surface, near-surface, core shell) have attracted much attention a trimetallic alloys advanced catalyst due to primarily the three unique effects, i.e., geometric, electronic and strain, introduced by the secondary or tertiary metal [24-26]. In the experiment, Bi as a secondary have been verified superior electrocatalystic activity due to Bi can promote the cleavage of O-H bond with Pt favor the session of C-H bond, in which the efficiency of HCOOH oxidation was improved in the cell anode by promotion of HCOOH oxidation directly [27-29]. Ru also a good modifier of Pt, nevertheless, alloy RuPt enhance activity via supporting the OH further the CO oxidation that enhance the high potential CO oxidation rather direct oxidation [26]. Other relativity expensive like Au and Ag often used loading metal [30, 31]. The cheaper metal Cu, Fe and Co [32-35] have been proved for FAO as well as Pd, Mn, Pb, Sn, etc. Trimetallic alloy PtPdAu [36], PtCuBi [37], and PtRuSn [38] have been studied widely to overcome such problems. Alloy change the electronic structure by electron exchange of catalyst interior to change the adsorption energy make the catalyst close the volcano top of Sabatier. Core shell also is excellent structure to enhance stability and activity by the change the stain.

Modified and found the suitable support of noble metal improve the attractive features of high electrical conductivity, chemical stability and low cost, in which carbon materials as supports have been applied extensively due to high surface-area carbon materials and stability for fuel cell catalysts, beside carbon materials, TiO_2, SiO_2, WO_3 as supports were used for holding up the noble metal [39-41].

1.2.2 Pd-based catalyst

Pd as the catalyst of DFAFCs were indicated pensively after Pt, Pd have been researched the Pd more suitable for FAO owing to Pd live in main group of elements of periodic table, in which Pd can reduce the formation of CO [42]. Compared Pd and Pt, Pd has a higher activity for electro-oxidation HCOOH, but Pt is more stable [43]. It has been revealed an oleylamine-mediated synthesis of monodisperse Pd NPs for catalytic oxidation of formic acid under fuel cell reaction conditions, in which solved the previously identified problem associated with the low catalytic activity of high-quality Pd NPs [37]. Considerable research efforts have been devoted to the low-index surfaces of crystal Pd, following the order of Pd(110) < Pd (111) < Pd(100) [44]. The size of catalyst was demonstrated in a study show that the optimal Pd parti-

cle size for CO oxidation based on computer simulation using the mesoscopic stochastic model and Langevin equations was found to be in the range of 5-7 nm [34, 45]. Though Pd have a better performance still can form CO, which produced H_2 with <100 ppm CO under ambient conditions for decomposition of HCOOH [13]. This is still matter of debate for origins of CO, some authors pointed out that the formation of CO is owing to the HCOOH oxidation [35], other authors proposed that the CO is result from CO_2 reduction in the H^+ abundant environment [14, 46]. And Pd is an excellent material for CO_2 reduction [47].

In hence, highly efficient novel Pd-based nanocatalysts have been synthesized to overcome this problem. Such as Pd-M (M=Cu, Co, Fe, Pt, Au, Ru, Ag, etc.) [33, 48-51]. It has been confirmed that Ag-Pd core-shell nanocatalyst is an excellent material for HCOOH decomposition at room temperature by the experiment evidences with d-band center theory, in which the d-band closer the Fermi-level the stronger adsorption energy. Modified Ag is not only improve the stability but also enhance the activity by changing the electronic structure of Pd [49]. Another interesting finding is that P, N, B non-metal used in modifying the Pd for FAO were described for HCOOH electro-oxidation [52]. Pd-B have been proved that exist high electrocatalytic activity [53], which is consistent with the observation from DFT model of the Pd-B [54]. We aim to find the catalyst of high-efficiency and low cost, so doping the non-metal material continues to be a great impetus to research effectors for the application of catalyst. Pd and Pt both are the best noble metal as the electrocatalytic of FAO, however, they will be CO-poison during the reaction. What is surprising is that the Pt-Pd is especially important as alloying, except obvious change in surface composition, low loading Pt can improve the performance since material with modified electronic properties, which can potentially be responsible for the synergistic effect of both metals on FAO [55].

The support plays an important role for the Pd catalyst, common supports include Vulcan XC-72, carbon black, ordered mesoporous carbon (OMC), carbon nanotubes (MWCNTs), graphene ,graphene oxide (GO) have been applied in the synthetized catalyst [10]. rGO has been supposed as a promising support for anodic catalyst of DFAFCs, in which rGO possesses a large surface area, outstanding electron conductivity, and may also have significant effects on the chemical reaction parameters on the surface of metallic nanoparticles [56].

1.2.3 Single atom alloy (SAA) catalyst

Recently, SAA were fabricated and employed for various types of reactions in heterogeneous catalysis. SAA have been stimulated wildly studies effectors owing to their unique properties and utmost utilization of metal atoms, Decreasing the size like SAA has some advantages including: low–coordination environment of metal centers to the unsaturated metal atoms exposed on the small-sized particles, quantum size effects, where confinement of elec-

trons leads to a discrete energy level distributions and a distinctive HOMO-LUMO gap, metal support interactions, which originate from the chemical bonding effect between metal and supports and the associated interface, as well as the charge transfer between metal species and supports [57]. The development of SAA benefited from the improvement of the nanotechnology and experimental characterization methods rocketly, harder to be observed than alloy or core-shell structure, thus the special characterization such as subang-strom-resolution aberration-corrected scanning transmission electron microscopy (AC-STEM). In addition, with the combination of state-of-the-art experimental techniques such as X-ray absorption spectroscopy and advanced modeling and simulation methods in computational chemistry [57-60]. The activity sites usually are an atom of unreached saturation coordination on the surface of catalyst.

In 2011, Tao Zhang' group synthezied the single catalyst Pt_1/FeO_X for CO oxidation that was more stable and improved 2-3 fold activity than before [61]. This a great discover for reducing the cost and evidenced the feasibility of single atom catalyst. For example, single-atom Pt sites on AuPt alloy surface

greatly promote FAO via the direct mechanism meanwhile inhibiting the *CO formation in indirect mechanism mainly through the ensemble effect, resulting in superior catalytic activity and selectivity [62]. Theoretically, bimetallic SAA models allow one to study the unique effects of alloyed single atom on catalytic properties by exploiting their structural uniformity and simplicity.

1.2.4 Synthetic method

There are many works were established for syntheses capable of generating alloy nanocrystals with well-controlled properties. The common synthetic approaches display the following methods: (1) coreduction is the most straightfoeard method, where the simultaneous reduction of two metal containing precursors to zerovalent atoms and grow together to form alloy catalyst; (2) thermal decomposition have been verified alloy nanocrystals semiconducting and metal−oxide nanocrystals, where are used for some precursors what cannot be reduction easily and have low reduction potential; (3) seed-mediated growth is the foremost synthetic route to the generation of well-defined alloy nanocrystals, where preformed nanocrystals (or seeds) with well-defined characteristics serve as primary sites for the heterogeneous nucleation of newly formed atoms generated from the reduction or thermal decomposition of a metal precursor, the structure of surface of seed deposition and recombination of atoms is controlled the both kinetics and thermodynamics. When the temperature is high and the deposition is relative slow, a thermodynamic production will be the main production but a kinetically controlled product is one that deviates from the shape prescribed by the thermodynamics, core-shell nanocrystals, dendritic nanocrystal and core-frame nano-

crystals is a kind of typical special structure by the seed-mediated growth; (4) galvanic replacement is an electrochemical process involving the oxidation of one metal by the ions of another metal having a more positive reduction potential. If this condition is met, the metal ions will remove electrons from the template, become reduced, and then plate the exterior of the template, while its interior dissolves into the solution. The final structure is characterized by a hollow alloy nanostructure that takes on the shape of the initial template [63].

1.3 Theoretical basis and calculation

Quantum chemistry is an extremely important branch in the field of theoretical chemistry, which aims to explore some basic problems in chemical systems by using the relevant basic principles and methods in the discipline of quantum mechanics. The earliest quantum chemical calculation originated in the 1930s. German physicists Heitler and London creatively used the basic principles of quantum mechanics to calculate the structure of H_2 molecule, and used a fairly approximate and reasonable calculation method to give its binding energy, thus opening the door of quantum chemistry. Among them, valence bond theory, molecular orbital theory and coordination field theory are the main representative theoretical achievements in the early development of quantum chemistry. In addition, the Schrodinger equation is an essential fundamental assumption of quantum mechanics. Because schrodinger equation can well express the state law of microscopic particles changing with time, it can reflect the quantum behavior of wave function very accurately, which is specifically expressed as:

$$-\frac{h}{i}\frac{\partial\psi}{\partial t} = \hat{H}\Psi \qquad (1\text{-}1)$$

In addition, when the potential function no longer changes with time t, the schrodinger equation is expressed as:

$$\hat{H}\psi(q) = E\psi(q) \qquad (1\text{-}2)$$

In equation 2-2, E is the eigenvalue of the equation, and it is also a stationary energy. Independent of time t wave function Ψ (q), also known as the equation E eigenfunction. Ĥ Hamiltonian operator is not t.

In fact, it is almost impossible to solve the schrodinger equation for the material structure of the multi-electron system. Therefore, the scientists conducted in-depth research on the calculation methods of quantum chemistry on this basis, and introduced various approximations to simplify the solution of the schrodinger equation in the actual calculation process. Therefore, they successfully developed ab initio, semi-empirical full differential overlap method and inter-differential overlap method. The establishment of these theoretical methods not only

expands the application of quantum chemistry in chemical systems, but also greatly improves the accuracy of calculation.

1.3.1 Basic introduction to density functional theory

Density functional theory (DFT) is a quantum mechanical method widely used in the field of physics and chemistry for in-depth study of the electronic structure of practical multi-electron systems [64].The theoretical concept of DFT first originated in the 1920s. Thomas and Fermi first proposed the Thomas-Fermi model [65] in which electrons are not subjected to any external force and there is no interaction between them, and successfully simplified the Schrodinger equation describing electron motion into a wave equation. Although the establishment of Thomas-Fermi model is the most important step for the development of DFT theory, the accuracy of calculation is limited considering that the model does not actually introduce the atomic exchange energy involved in Hartree-Fock theory. In 1928, the British physicist Paul Adrien Maurice Dirac proposed the famous Dickard equation in the history of quantum chemistry and introduced a functional term of exchange energy on the basis of the Thomas-Fermi model, thus successfully improving the theoretical defects of it. In 1964, based on Hohenberg-Kohn theorem [66, 67], Hohenberg and Kohn went on the deep research furtherly as well as Kohn and Sham had some breakthroughs based on Kohn-Sham equation [68], they established the electronic density as the research of the basic variables clearly and then put forward to describe the actual electronic system of DFT, which was improving the precision of maximum extent with the low degrees of freedom and supporting the reasonable computation make quantum chemistry get the fast development and application. Since then, the new functional and other theoretical improvements have been put forward in terms of localization and non-localization, which makes the connotation of DFT be completed gradually.

1.3.2 Hohenberg–Kohn (HK) theorems

DFT originated from the Thomas-Fermi model but until Hohenberg and Kohn proposed hohenberg-kohn (HK) theorems that the DFT was applied in the research [58, 59]. Hohenberg-kohn theorem was reported that only the electron density is used as the basic quantity of the multi-electron system as result in lessen the computation. Moreover, the second Hohenberg-Kohn theorem illustrated that the ground-state energy was determined to the regulation ground state density, furthermore ensuring the variational principle of DFT, in which can gain the ground state density and energy of electron by minimizing total system energy $E[\rho]$ (integration $E[\rho]$ with the number of electrons).

In summary, the total energy of the system for the multi-electron system is as follows:

$$E[\rho] = T[\rho] + E_{ee}[\rho] + \int \rho(r)V(r)dr \qquad (1\text{-}3)$$

Where is $T[\rho]$ and $E_{ee}[\rho]$ are the kinetic energy and interaction of electrons in multiple electron system, respectively.

1.3.3 Kohn-Sham（K-S）equation

The distribution function of electron density is used for solving the ground state wave function of multi-electron systems by Hohenberg-Kohn theorem. However, it cannot express the specific relationship of them. A hypothetical that is multi-electron system with the same electron density but only non-interaction was added on the basis of HK theorem. The electron density is expressed as orbitals, thus calculated the sum of the kinetic energy of each single electron by calculating the expected value of the kinetic energy operator of the proposed multi-electron system. This is famous Kohn-Sham（K-S）[68] equation as:

$$[-\frac{h^2}{2m_e}\nabla^2 + V_{ext}(r) + V_H(r) + V_{xc}(r)] = \varepsilon_i \varphi_i(r) \qquad (1\text{-}4)$$

Where *Vext(r)*, *VH(r)* and *Vxc(r)* are external potential, Hartree potential and exchange correlation potential, respectively. Effective potential is decided in electron density and expressed as : *Veff(r)= Vext(r)+ VH(r)+ Vxc(r)*。

Herein, ensuring the ground state energy and density, making the whole ground state energy instead of the single by solving the KS equation, so that the complex problems are greatly simplified.

1.3.4 Exchange correlation energy functional

Exchange correlation potential is essential for solving the K-S equation.Accordingly, it is necessary to define an appropriate exchange correlation approximation like: local density approximation (LDA), generalized gradient approximation (GGA), hybrid functional and LDA (GGA) + U, etc.

(1) LDA is suitable for homogeneous electron gas, where exchange correlation energy functional only has a relationship with the electron density depends on the value of each point in space. It is assumed that the changing of electronic density $\rho(r)$ is very slow to make the space of electronic density cut into some micro unit d^3r; $\rho(r)$ was regraded a constant but is a function of location *(r)*. LDA can be expressed as:

$$E_{xc}^{LDA}[\rho] = \int \rho(r)\varepsilon_{xc}[\rho]d^3r \qquad (1\text{-}5)$$

$\varepsilon_{xc}[\rho]$ is an exchange correlation energy as densityρ with homogeneous and non-interacting electron gas, so the corresponding local exchange correlation function can

be expressed as:

$$E_{xc}^{LDA} = \frac{\delta E_{xc}^{LDA}[\rho]}{\delta\rho} = \varepsilon_{xc}[\rho] + \rho(r)\frac{\delta\varepsilon_{xc}[\rho]}{\delta\rho} \qquad (1\text{-}6)$$

(2) GGA is used for non-homogeneity of the true electron density, thus $\varepsilon_{xc}[\rho]$ is not only a function of electronic density but also electronic density gradient, specifically expressed as:

$$E_{xc}^{GGA}[\rho] = \int \rho(r)\varepsilon_{xc}[\rho(r), |\nabla\rho(r)|]d^3r \qquad (1\text{-}7)$$

GGA is rooted the LDA and more close the real condition [90]. GGA method is widely used in the calculation of chemistry and materials, there are many forms of GGA functional, such as the common perdew-wang (PW91) and perdew-burke-ernzerhof (PBE).

(3) Hybrid functional is used for the addition of intermolecurlar forces, GGA method cannot gain the idea results, but the Hartree-Fock theory combine with the rest of the exchange–correlation energy from other sources (ab initio or empirical) to modify the defects of GGA. Linear combination the exchange correlation energy of Hartree-Fock theory with the DFT method to get the hybrid functional, in which can control ration of the them that is closer the ture experiments' data. But using the hybrid functional tends to increase the computation that is more satiable for the calculation of small molecule system.

(4) LDA(GGA)+U is developed for d electrons or f electrons in the system results in strong electron exchange interactions that cannot be ignored such as transition metal oxides and rare earth chemicals. As the basis of LDA (GGA) foundation, added a parameter of Hubbard is U to define the LDA(GGA)+U, follow as:

$$E_{LDA(GGA)+U}[\rho(r)] = E_{LDA(GGA)}[\rho(r)] + \frac{U-J}{2}\sum_{\sigma}\mathrm{Tr}[\rho^{\sigma} - \rho^{\sigma}\rho^{\sigma}] \qquad (1\text{-}8)$$

This foundation can describe materials those have the d or f electronic orbits better lead to the theoretical calculation value of the transition metal oxide semiconductor band gap is close to the experimental value so that the reasonable theoretical calculation value can be used to predict the optical properties of the system reliably.

1.3.5 The choice of *k* point in Brillouin zone

In the calculating the charge density distribution and the total energy of the system, where make the integration for the Brillouin zone by the first-principles method. Assuming that the selecting uniform grid of k point in Brillouin zone, the calculation result will be more accurate

when choose the larger k point, which will lead to the increase computation and low calculation efficiency. Therefore, a method of efficient integration for Brillouin zone is needed in the calculation process, so as to achieve a higher calculation accuracy with a smaller k point density. In this regard, Chadi and Cohen proposed a Chadi-Cohen method based on the determination of two special k points [69]. Although this method is great, the accuracy and computational efficiency of the calculated results are closely dependent on the special k points, which has certain limitations. After this, Monkhorst and Pack proposed the Monkhorst-Pack method [70], which make the three-directions change the three one-dimensionals as a result of achieving a kind of simple method.

1.3.6 Overview of computing software

The rapidly development of software in the computer field make the many computational chemistry software have a giant improvement, the commercial software VASP (Vienna ab-initio simulation package) was applied extensively [71, 72]. This is developed by the Hafner's group of the University of Vienna in Austria, based on CASTEP, added the plane wave group and pseudopotential to make the Ab initio molecular dynamics simulation. The principle is that solve the Schrödinger equation by the sloving the K-S equation and introduced projector augmented wave (PAW) and the ultrasoftsoft pseudopotential (USPP) to realize the interaction between electrons and ions. In addition, the improved tetrahedron - integral method is used in the Brillouin zone to achieve a faster calculation convergence.

1.4 Other direct liquid fuel cells (DLFCs)

Direct liquid fuel cells (DLFCs) are one of the most promising types of fuel cells due to their high energy density, simple structure, small fuel cartridge, instant recharging, and ease of storage and transport. DFAFCs is one of them, methanol, ethanol, ethylene glycol, glycerol, dimethyl ether etc. Their cathodes are same with DFAFCs by the oxygen oxidation, but anode use different sources lead to different reaction. Among that, methanol and ethanol were the most common types of fuel used I will cover this DLFCs in the following text.

1.4.1 Direct methanol fuel cells (DMFCs)

Methanol is fed directly into the anode in liquid, it has good electrochemical activity, is consistently available, is biodegradable, and is relatively cheap. It can be easily handled, transported and stored, which makes it a good fuel [5, 73, 74]. It also has a high energy density of 4820 Wh L^{-1} compared to that of hydrogen. The reaction follows as:

Anode: $CH_3OH + H_2O \rightarrow CO_2 + 6H^+ + 6e^-$

Cathode: $3/2O_2 + 6H^+ + 6e^- \rightarrow 3H_2O$

Overall: $CH_3OH + 3/2O_2 \rightarrow CO_2 + 2H_2O$ OCV ~1.21V

The anode catalysts of DMFCs have been showed in previous researches, different types of catalysts have been explored to increase the electrochemical activity of the anode, like Pt-Ru [75, 76], Pt-Pd [77, 78], Pt-Ni [79], Pd-Ni [80], Pt-Au [81] Pt-Ru-Ni [82] and Pt-TiO2[83, 84]. Pt-Ru is synthetized by urea-assisted homogeneous deposition coupled with H_2 reduction, which is a simple method and has been investigated for getting high-performance supported high metal loading Pt-Ru anode catalyst for DMFCs [75].

1.4.2 Direct ethanol fuel cells (DMFEs)

Ethanol is safer, it is easy to get for the fuel cell, which can be produced from the agriculture like corn and wheat. It cheaper than other raw material and non-toxic, meanwhile, it has a high density of 8030 Wh kg^{-1}. Nonetheless, the key point is that C-C bond is extremely stable so it is difficult to break and has to skip a high barrier. For example, increasing the temperature or enhance the pressures. The reaction is following as:

Anode: $C_2H_5OH + 3H_2O \rightarrow 2CO_2 + 12H^+ + 12e$-

Cathode: $3O_2 + 12H^+ + 12e^- \rightarrow 6H_2O$

Overall: $C_2H_5OH + 3O_2 \rightarrow 2CO_2 + 3H_2O$ OCV ~1.15V

Anode catalysts include bimetallic and trimetallic alloy have been confirmed for the ethanol oxidation, for instance, Pt-Ni [85], Pt-Au [86], Pt-TiO_2 [87], Pt-Re-Sn [88], Pt-Sn-Ce [89], Pt-Sn-Pr [90], Pt-Ir and Pt-Ir-Sn [91]. Pt-Ir-Sn alloy has the highest power density of anode oxidation, in which Sn or its alloys provide oxygen-containing species, while Ir helps in ethanol oxidation by giving OH_{ads} species in ethanol electrooxidation. Pt-d states down shift owing to add Ir decreasing Pt-CO bond energy.

1.4.3 Direct ethylene glycol fuel cells (DEGFCs)

Ethylene glycol is an alcohol with 2 hydroxyl groups, it is easy to gain the materials due to it is used for an antifreeze in the automobile industry. The overall reaction as:

Anode: $C_2H_6O_2 + 2H_2O \rightarrow 2CO_2 + 10H^+ + 10e$-

Cathode: $5/2O_2 + 10H^+ + 10e^- \rightarrow 5H_2O$

Overall: $C_2H_5OH + 5/2O_2 \rightarrow 2CO_2 + 3H_2O$ OCV ~1.22V

The catalyst shows the performance for the DEGFCs anode oxidation. For example, including Pt-Ru-W [92], Pt-Sn [93], Pt-Sn-Ni [94], Pd and Pd-Ag [95]. Compared with the PtSn/C and PtRu/C, The former as electrocatalysts are better for ethylene glycol oxidation than

PtRu/C electrocatalysts because the oxidation starts at lower potentials and high current values are obtained in the region of interest for DEGFCs [93].

1.4.4 Direct dimethyl ether fuel cells (DDEFCs)

Direct dimethyl ether is the simplest ether. It has less toxic than the methanol. It can be used as gas or liquid in the fuel cell [96-98]. There were 12 electrons transferred in the dimethyl ether oxidation, more than methanol's 6 electrons, the reaction is:

Anode: $(CH_3)_2O + 3H_2O \rightarrow 3CO_2 + 12H^+ + 12e^-$

Cathode: $3O_2 + 12H^+ + 12e^- \rightarrow 3H_2O$

Overall: $(CH_3)_2O + 3O_2 \rightarrow 2CO_2 + 3H_2O$ OCV ~1.20V

Pt also common catalyst for dimethyl ether oxidation as other direct liquid fuel cell. Direct dimethyl ether mixes with other raw material as fuel is a potential direct liquid fuel cell [99].

1.4.5 Direct glycerol fuel cells (DGFCs)

Glycerol was the main by-product in the production of biodiesel that was considered a kind of waste in the biodiesel industry so its prices is extremely low. The nature of glycerol, which is non-toxic, non-volatile, non-flammable, bio-renewable and cheap, makes it a potentially promising fuel for fuel cell systems. It also has a high theoretical energy density of 6.4 kWh L^{-1} [100]. The catalysts usually are used what are Pd, Pt and Au [101]. The whole reaction is:

Anode: $C_3H_8O_3 + 3H_2O \rightarrow 3CO_2 + 14H^+ + 14e^-$

Cathode: $7/2O_2 + 14H^+ + 14e^- \rightarrow 3H_2O$

Overall: $C_3H_8O_3 + 7/2O_2 \rightarrow 3CO_2 + 3H_2O$ OCV ~1.21V

1.5 Motivation

In recent years, depletion of energy resources leads us to develop renewable, environmental and low-cost raw material for electronic energy. The formic acid not only was used in the hydrogen storage but also studied in the direct formic acid fuel cell. Formic acid as fuel is safer, clear and cheaper, which has proved promising new energy. Anode catalyst plays an indispensable role in the formic acid oxidation as a result of improving cell performance and enhances the feasibility of an application.

There is thereby an urgent need but it is still significant to find cheap and high-efficiency anode catalysts. It is generally accepted that noble Pt and Pd have a good performance for the

formic acid oxidation, the disadvantages are too expensive and easy to CO-poisoning. The CO will take up the reaction sites and make the catalyst loss activity. We have to consider the reasons for this and come over these though points.

Herein, I will modify Pt- and Pd-based alloy catalysts to improve their performance by simple synthetic method, meanwhile, analysis the reaction mechanism at the atom level by the DFT calculation. At the same time, we will give a guide for the choosing of catalyst in the experiment to achieve a better performance of direct formic acid fuel cells.

References

[1] M. Weber, J.T. Wang, S. Wasmus, R. Savinell, Formic acid oxidation in a polymer electrolyte fuel cell: a real‐time mass‐spectrometry study, Journal of the Electrochemical Society, 143 (1996) L158.

[2] C. Rice, R.I. Ha, R.I. Masel, P. Waszczuk, A. Wieckowski, T. Barnard, Direct formic acid fuel cells, J. Power Sources, 111 (2002) 83–89.

[3] U.B. Demirci, Direct liquid-feed fuel cells: Thermodynamic and environmental concerns,J. Power Sources 169 (2007) 239-246.

[4] X. Yu, P.G. Pickup, Recent advances in direct formic acid fuel cells (DFAFC), J. Power Sources, 182 (2008) 124-132.

[5] B.C. Ong, S.K. Kamarudin, S. Basri, Direct liquid fuel cells: A review, Int. J. Hydrogen Energy, 42 (2017) 10142-10157.

[6] W.A. H. Wang, X. Liu, C. Heath Turner b, Oxygen reduction reaction on Pt(1 1 1), Pt(2 2 1), and Ni/Au_1Pt_3(2 2 1) surfaces: Probing scaling relationships of reaction energetics and interfacial composition, Chem. Eng. Sci., (2018) 239–250.

[7] M. Shao, Q. Chang, J.-P. Dodelet, R. Chenitz, Recent advances in electrocatalysts for oxygen reduction reaction, Chem. Rev., 116 (2016) 3594-3657.

[8] A. Rabis, P. Rodriguez, T.J. Schmidt, Electrocatalysis for polymer electrolyte fuel cells: recent achievements and future challenges, Acs Catalysis, 2 (2012) 864-890.

[9] B. Wang, Recent development of non-platinum catalysts for oxygen reduction reaction,J. Power Sources 152 (2005) 1-15.

[10] K. Jiang, H.X. Zhang, S. Zou, W.B. Cai, Electrocatalysis of formic acid on palladium and platinum surfaces: from fundamental mechanisms to fuel cell applications, Phys. Chem. Chem. Phys., 16 (2014) 20360-20376.

[11] L. Ou, J. Chen, Y. Chen, J. Jin, Mechanistic Study of Pt-Catalyzed Electrooxidation of HCOOH in Acid Medium: Kinetic Considerations on the Effect of Solvation, J. Phys. Chem. C, 122 (2018) 24871-24884.

[12] M.D. Obradović, S.L. Gojković, HCOOH oxidation on thin Pd layers on Au: Self-poisoning by the subsequent reaction of the reaction product, Electrochim. Acta, 88 (2013) 384-389.

[13] J.S. Yoo, F. Abild-Pedersen, J.K. Nørskov, F. Studt, Theoretical Analysis of Transition-Metal Catalysts for Formic Acid Decomposition, ACS Catal., 4 (2014) 1226-1233.

[14] J.Y. Wang, H.X. Zhang, K. Jiang, W.B. Cai, From HCOOH to CO at Pd electrodes: a surface-enhanced infrared spectroscopy study, JACS, 133 (2011) 14876-14879.

[15] W. Gao, J.A. Keith, J. Anton, T. Jacob, Theoretical elucidation of the competitive electro-oxidation mechanisms of formic acid on Pt (111), JACS, 132 (2010) 18377-18385.
[16] R. Zhang, H. Liu, B. Wang, L. Ling, Insights into the preference of CO2 formation from HCOOH decomposition on Pd surface: a theoretical study, J. Phys. Chem. C, 116 (2012) 22266-22280.
[17] A.O. Elnabawy, J.A. Herron, J. Scaranto, M. Mavrikakis, Structure Sensitivity of Formic Acid Electrooxidation on Transition Metal Surfaces: A First-Principles Study, J. Electrochem. Soc., 165 (2018) J3109-J3121.
[18] H.-F. Wang, Z.-P. Liu, Formic acid oxidation at Pt/H2O interface from periodic DFT calculations integrated with a continuum solvation model, J. Phys. Chem. C, 113 (2009) 17502-17508.
[19] W. Zhong, Y. Qi, M. Deng, The ensemble effect of formic acid oxidation on platinum–gold electrode studied by first-principles calculations,J. Power Sources 278 (2015) 203-212.
[20] J. Joo, T. Uchida, A. Cuesta, M.T. Koper, M. Osawa, Importance of acid-base equilibrium in electrocatalytic oxidation of formic acid on platinum, JACS, 135 (2013) 9991-9994.
[21] E. Herrero, J.M. Feliu, Understanding formic acid oxidation mechanism on platinum single crystal electrodes, Curr. Opin. Electrochem., 9 (2018) 145-150.
[22] M. Neurock., M. Janikb., A. Wieckowskic., A first principles comparison of the mechanism and site requirements for the electrocatalytic oxidation of methanol and formic acid over Pt, Faraday Discuss., 140 (2008) 363-378.
[23] W. Gao, J.E. Mueller, Q. Jiang, T. Jacob, The Role of Co‐Adsorbed CO and OH in the Electrooxidation of Formic Acid on Pt (111), Angew. Chem. Int. Ed., 51 (2012) 9448-9452.
[24] S. Daniele, S. Bergamin, Preparation and voltammetric characterisation of bismuth-modified mesoporous platinum microelectrodes. Application to the electrooxidation of formic acid, Electrochem. Commun., 9 (2007) 1388-1393.
[25] W. Chen, S. Chen, Iridium-platinum alloy nanoparticles: Composition-dependent electrocatalytic activity for formic acid oxidation, J. Mater. Chem. A, 21 (2011) 9169-9178.
[26] E.N. El Sawy, P.G. Pickup, Formic Acid Oxidation at Ru@Pt Core-Shell Nanoparticles, Electrocatalysis, 7 (2016) 477-485.
[27] J.V. Perales-Rondon, A. Ferre-Vilaplana, J.M. Feliu, E. Herrero, Oxidation mechanism of formic acid on the bismuth adatom-modified Pt(111) surface, JACS, 136 (2014) 13110-13113.
[28] J.D. Lović, S.I. Stevanović, D.V. Tripković, A.V. Tripković, R.M. Stevanović, V.M. Jovanović, K.D. Popović, Insight into electrocatalytic stability of low loading Pt-Bi/GC and Pt/GC clusters in formic acid oxidation, J. Solid State Electrochem., 19 (2015) 2223-2233.
[29] F.J. DiSalvo Jr, H.D. Abruna, Intermetallic compounds for use as catalysts and catalytic systems, Google Patents, 2008.

[30] G. You, J. Jiang, M. Li, L. Li, D. Tang, J. Zhang, X.C. Zeng, R. He, PtPd(111) Surface versus PtAu(111) Surface: Which One Is More Active for Methanol Oxidation?, ACS Catal., 8 (2017) 132-143.
[31] J.K. Yoo, M. Choi, S. Yang, B. Shong, H.-S. Chung, Y. Sohn, C.K. Rhee, Formic acid electrooxidation activity of Pt and Pt/Au catalysts: Effects of surface physical properties and irreversible adsorption of Bi, Electrochim. Acta, 273 (2018) 307-317.
[32] J. Klein, S. Brimaud, A.K. Engstfeld, R.J. Behm, Atomic scale insights on the electronic and geometric effects in the electro-oxidation of CO on PtxRu1-x/Ru(0001) surface alloys, Electrochim. Acta, (2019).
[33] S. Hu, F. Che, B. Khorasani, M. Jeon, C.W. Yoon, J.-S. McEwen, L. Scudiero, S. Ha, Improving the electrochemical oxidation of formic acid by tuning the electronic properties of Pd-based bimetallic nanoparticles, Appl. Catal., B, 254 (2019) 685-692.
[34] W. Zhou, J.Y. Lee, Particle size effects in Pd-catalyzed electrooxidation of formic acid, J. Phys. Chem. C, 112 (2008) 3789-3793.
[35] R. Larsen, S. Ha, J. Zakzeski, R.I. Masel, Unusually active palladium-based catalysts for the electrooxidation of formic acid, J. Power Sources, 157 (2006) 78-84.
[36] C. Li, H. Wang, Y. Li, H. Yu, S. Yin, H. Xue, X. Li, Y. Xu, L. Wang, Tri-metallic PtPdAu mesoporous nanoelectrocatalysts, J. Nanotechnol., 29 (2018) 11762-117625.
[37] M.A. Ud Din, F. Saleem, B. Ni, Y. Yong, X. Wang, Porous Tetrametallic PtCuBiMn Nanosheets with a High Catalytic Activity and Methanol Tolerance Limit for Oxygen Reduction Reactions, Adv. Mater., 1604994 (2017) 1-8.
[38] J.S. Yoo, H.T. Kim, H.-I. Joh, H. Kim, S.H. Moon, Preparation of a CO-tolerant PtRuxSny/C electrocatalyst with an optimal Ru/Sn ratio by selective Sn-deposition on the surfaces of Pt and Ru, Int. J. Hydrogen Energy, 36 (2011) 1930-1938.
[39] C. Tao, W. Guopeng, F. Zhaochi, H. Gengshen, S. Weiguang, Y. Pinliang, L. Can, In situ FT-IR study of photocatalytic decomposition of formic acid to hydrogen on Pt/TiO_2 catalyst, Chinese J. Catal., 29 (2008) 105-107.
[40] S. Guenais-Langlois, C. Bouyer, J.-C. Broudic, B. Coq, The role of Pt/SiO_2 in the catalytic denitration by HCO_2H of HNO_3 concentrated media, Appl. Catal. B, 27 (2000) 199-204.
[41] K. Chen, P. Shen, A. Tseung, Anodic Oxidation of Formic Acid on Electrodeposited Pt/WO 3 Electrode at Room Temperature, J. Electrochem. Soc., 142 (1995) L54.
[42] Z. Liu, L. Hong, M.P. Tham, T.H. Lim, H. Jiang, Nanostructured Pt/C and Pd/C catalysts for direct formic acid fuel cells, J. Power Sources, 161 (2006) 831-835.
[43] P. Hong, F. Luo, S. Liao, J. Zeng, Effects of Pt/C, Pd/C and PdPt/C anode catalysts on the performance and stability of air breathing direct formic acid fuel cells, Int. J. Hydrogen Energy, 36 (2011) 8518-8524.

[44] N. Hoshi, K. Kida, M. Nakamura, M. Nakada, K. Osada, Structural effects of electrochemical oxidation of formic acid on single crystal electrodes of palladium, J. Phys. Chem. B, 110 (2006) 12480-12484.
[45] Y. Kim, D.H. Kim, Understanding the effect of Pd size on formic acid dehydrogenation via size-controlled Pd/C catalysts prepared by NaBH4 treatment, Appl. Catal., B, 244 (2019) 684-693.
[46] Y. Wang, Y. Qi, D. Zhang, C. Liu, New Insight into the Decomposition Mechanism of Formic Acid on Pd(111): Competing Formation of CO2 and CO, J. Phys. Chem. C, 118 (2014) 2067-2076.
[47] H.A. Hansen, J.B. Varley, A.A. Peterson, J.K. Norskov, Understanding Trends in the Electrocatalytic Activity of Metals and Enzymes for CO2 Reduction to CO, J. Phys. Chem. Lett., 4 (2013) 388-392.
[48] Z. Zhang, Y. Liu, B. Chen, Y. Gong, L. Gu, Z. Fan, N. Yang, Z. Lai, Y. Chen, J. Wang, Y. Huang, M. Sindoro, W. Niu, B. Li, Y. Zong, Y. Yang, X. Huang, F. Huo, W. Huang, H. Zhang, Submonolayered Ru Deposited on Ultrathin Pd Nanosheets used for Enhanced Catalytic Applications, Adv. Mater., 28 (2016) 10282-10286.
[49] K. Tedsree, T. Li, S. Jones, C.W.A. Chan, K.M.K. Yu, P.A.J. Bagot, E.A. Marquis, G.D.W. Smith, S.C.E. Tsang, Hydrogen production from formic acid decomposition at room temperature using a Ag–Pd core–shell nanocatalyst, Nat. Nanotechnol., 6 (2011) 302-307.
[50] K. Mori, H. Tanaka, M. Dojo, K. Yoshizawa, H. Yamashita, Synergic Catalysis of PdCu Alloy Nanoparticles within a Macroreticular Basic Resin for Hydrogen Production from Formic Acid, Chem. Eur. J., 21 (2015) 12085-12092.
[51] M.A. Matin, J.-H. Jang, Y.-U. Kwon, PdM nanoparticles (M= Ni, Co, Fe, Mn) with high activity and stability in formic acid oxidation synthesized by sonochemical reactions, J. Power Sources, 262 (2014) 356-363.
[52] S. Wang, J. Chang, H. Xue, W. Xing, L. Feng, Catalytic stability study of a Pd‐Ni2P/C catalyst for formic acid electrooxidation, ChemElectroChem, 4 (2017) 1243-1249.
[53] K. Jiang, K. Xu, S. Zou, W.-B. Cai, B-Doped Pd catalyst: boosting room-temperature hydrogen production from formic acid–formate solutions, JACS Society, 136 (2014) 4861-4864.
[54] J.S. Yoo, Z.-J. Zhao, J.K. Nørskov, F. Studt, Effect of boron modifications of palladium catalysts for the production of hydrogen from formic acid, ACS Catalysis, 5 (2015) 6579-6586.
[55] B. Gralec, A. Lewera, Catalytic activity of unsupported Pd-Pt nanoalloys with low Pt content towards formic acid oxidation, Appl. Catal., B, 192 (2016) 304-310.

[56] Y. She, Z. Lu, W. Fan, S. Jewell, M.K.H. Leung, Facile preparation of PdNi/rGO and its electrocatalytic performance towards formic acid oxidation, J. Mater. Chem. A, 2 (2014) 3894.
[57] X.-F. Yang, A. Wang, B. Qiao, J. Li, J. Liu, T. Zhang, Single-atom catalysts: a new frontier in heterogeneous catalysis, Acc. Chem. Res., 46 (2013) 1740-1748.
[58] S. Liang, C. Hao, Y. Shi, The Power of Single-Atom Catalysis, ChemCatChem, 7 (2015) 2559-2567.
[59] C. Zhu, S. Fu, Q. Shi, D. Du, Y. Lin, Single-Atom Electrocatalysts, Angew. Chem. Int. Ed., 56 (2017) 13944-13960.
[60] Y. Chen, S. Ji, C. Chen, Q. Peng, D. Wang, Y. Li, Single-Atom Catalysts: Synthetic Strategies and Electrochemical Applications, Joule, 2 (2018) 1242-1264.
[61] B. Qiao, A. Wang, X. Yang, L.F. Allard, Z. Jiang, Y. Cui, J. Liu, J. Li, T. Zhang, Single-atom catalysis of CO oxidation using Pt1/FeOx, Nat. Chem., 3 (2011) 634-641.
[62] P.N. Duchesne, Z.Y. Li, C.P. Deming, V. Fung, X. Zhao, J. Yuan, T. Regier, A. Aldalbahi, Z. Almarhoon, S. Chen, D.E. Jiang, N. Zheng, P. Zhang, Golden single-atomic-site platinum electrocatalysts, Nat. Mater., 17 (2018) 1033-1039.
[63] K.D. Gilroy, A. Ruditskiy, H.C. Peng, D. Qin, Y. Xia, Bimetallic Nanocrystals: Syntheses, Properties, and Applications, Chem. Rev., 116 (2016) 10414-10472.
[64] E. Runge, E.K. Gross, Density-functional theory for time-dependent systems, Phys. Rev. Lett., 52 (1984) 997.
[65] E. Fermi, Magnetic moments of atomic nuclei, Nature, 125 (1930) 16-16.
[66] P. Hohenberg, W. Kohn, Inhomogeneous electron gas, Phys. Rev., 136 (1964) B864.
[67] W. Kohn, L.J. Sham, Self-consistent equations including exchange and correlation effects, Phys. Rev., 140 (1965) A1133.
[68] J.P. Perdew, K. Burke, M. Ernzerhof, Generalized gradient approximation made simple, Phys. Rev. Lett., 77 (1996) 3865.
[69] D. Chadi, Special points for Brillouin-zone integrations, Phys. Rev. B, 16 (1977) 1746.
[70] H.J. Monkhorst, J.D. Pack, Special points for Brillouin-zone integrations, Phys. Rev. B, 13 (1976) 5188.
[71] G. Kresse, J. Furthmüller, Efficient iterative schemes for ab initio total-energy calculations using a plane-wave basis set, Phys. Rev. B, 54 (1996) 11169.
[72] G. Kresse, J. Hafner, Ab initio molecular dynamics for liquid metals, Phys. Rev. B, 47 (1993) 558.
[73] R. Dillon, S. Srinivasan, A. Arico, V. Antonucci, International activities in DMFC R&D: status of technologies and potential applications,J. Power Sources 127 (2004) 112-126.
[74] A. Zainoodin, S.K. Kamarudin, M. Masdar, W.R.W. Daud, A.B. Mohamad, J. Sahari, Investigation of MEA degradation in a passive direct methanol fuel cell under different modes of operation, Appl. Energy, 135 (2014) 364-372.

[75] M.-S. Kim, B. Fang, N.K. Chaudhari, M. Song, T.-S. Bae, J.-S. Yu, A highly efficient synthesis approach of supported Pt-Ru catalyst for direct methanol fuel cell, Electrochim. Acta, 55 (2010) 4543-4550.
[76] W. Tokarz, G. Lota, E. Frackowiak, A. Czerwiński, P. Piela, Fuel cell testing of Pt–Ru catalysts supported on differently prepared and pretreated carbon nanotubes, Electrochim. Acta, 98 (2013) 94-103.
[77] T. Arikan, A.M. Kannan, F. Kadirgan, Binary Pt–Pd and ternary Pt–Pd–Ru nanoelectrocatalysts for direct methanol fuel cells, Int. J. Hydrog. Energy, 38 (2013) 2900-2907.
[78] F. Alcaide, G. Álvarez, P.L. Cabot, H.-J. Grande, O. Miguel, A. Querejeta, Testing of carbon supported Pd–Pt electrocatalysts for methanol electrooxidation in direct methanol fuel cells, Int. J. Hydrog. Energy, 36 (2011) 4432-4439.
[79] Y. Wang, J. Zang, L. Dong, H. Pan, Y. Yuan, Y. Wang, Graphitized nanodiamond supporting PtNi alloy as stable anodic and cathodic electrocatalysts for direct methanol fuel cell, Electrochim. Acta, 113 (2013) 583-590.
[80] Z. Qi, H. Geng, X. Wang, C. Zhao, H. Ji, C. Zhang, J. Xu, Z. Zhang, Novel nanocrystalline PdNi alloy catalyst for methanol and ethanol electro-oxidation in alkaline media,J. Power Sources 196 (2011) 5823-5828.
[81] W. Xiuyu, J. Zhang, Z. Hong, Pt-Au/CNT@ TiO2 as a high-performance anode catalyst for direct methanol fuel cells, Chinese J. Catal., 32 (2011) 74-79.
[82] Y. Zhao, L. Fan, J. Ren, B. Hong, Electrodeposition of Pt–Ru and Pt–Ru–Ni nanoclusters on multi-walled carbon nanotubes for direct methanol fuel cell, Int. J. Hydrog. Energy, 39 (2014) 4544-4557.
[83] N. Abdullah, S.K. Kamarudin, Titanium dioxide in fuel cell technology: an overview, J. Power Sources, 278 (2015) 109-118.
[84] L. Xing, J. Jia, Y. Wang, B. Zhang, S. Dong, Pt modified TiO2 nanotubes electrode: preparation and electrocatalytic application for methanol oxidation, Int. J. Hydrog. Energy, 35 (2010) 12169-12173.
[85] D. Soundararajan, J. Park, K. Kim, J. Ko, Pt–Ni alloy nanoparticles supported on CNF as catalyst for direct ethanol fuel cells, Curr Appl Phys, 12 (2012) 854-859.
[86] S.G. da Silva, J.C.M. Silva, G.S. Buzzo, R.F. De Souza, E.V. Spinacé, A.O. Neto, M.H. Assumpção, Electrochemical and fuel cell evaluation of PtAu/C electrocatalysts for ethanol electro-oxidation in alkaline media, Int. J. Hydrog. Energy, 39 (2014) 10121-10127.
[87] S. Meenakshi, K. Nishanth, P. Sridhar, S. Pitchumani, Spillover effect induced Pt-TiO2/C as ethanol tolerant oxygen reduction reaction catalyst for direct ethanol fuel cells, Electrochim. Acta, 135 (2014) 52-59.

[88] J. Goel, S. Basu, Pt-Re-Sn as metal catalysts for electro-oxidation of ethanol in direct ethanol fuel cell, Phys. Procedia, 28 (2012) 66-77.
[89] J.M. Jacob, P.G. Corradini, E. Antolini, N.A. Santos, J. Perez, Electro-oxidation of ethanol on ternary Pt–Sn–Ce/C catalysts, Applied Catalysis B: Environmental, 165 (2015) 176-184.
[90] P.G. Corradini, E. Antolini, J. Perez, Electro-oxidation of ethanol on ternary non-alloyed Pt–Sn–Pr/C catalysts,J. Power Sources 275 (2015) 377-383.
[91] J. Tayal, B. Rawat, S. Basu, Bi-metallic and tri-metallic Pt–Sn/C, Pt–Ir/C, Pt–Ir–Sn/C catalysts for Int. J. Hydrog. Energy electro-oxidation of ethanol in direct ethanol fuel cell, Int. J. Hydrog. Energy, 36 (2011) 14884-14897.
[92] R. Chetty, K. Scott, Catalysed titanium mesh electrodes for ethylene glycol fuel cells, J Appl Electrochem, 37 (2007) 1077-1084.
[93] A. Neto, T.R. Vasconcelos, R. Da Silva, M. Linardi, E. Spinacé, Electro-oxidation of ethylene glycol on PtRu/C and PtSn/C electrocatalysts prepared by alcohol-reduction process, J Appl Electrochem, 35 (2005) 193-198.
[94] A.O. Neto, M. Linardi, E.V. Spinacé, Electro-oxidation of ethylene glycol on PtSn/C and PtSnNi/C electrocatalysts, Ionics, 12 (2006) 309-313.
[95] Y. Yang, W. Wang, Y. Liu, F. Wang, Z. Zhang, Z. Lei, Carbon supported heterostructured Pd–Ag nanoparticle: Highly active electrocatalyst for ethylene glycol oxidation, Int. J. Hydrog. Energy, 40 (2015) 2225-2230.
[96] S. Ueda, M. Eguchi, K. Uno, Y. Tsutsumi, N. Ogawa, Electrochemical characteristics of direct dimethyl ether fuel cells, Solid State Ionics, 177 (2006) 2175-2178.
[97] J.O. Jensen, A. Vassiliev, M. Olsen, Q. Li, C. Pan, L.N. Cleemann, T. Steenberg, H.A. Hjuler, N. Bjerrum, Direct dimethyl ether fueling of a high temperature polymer fuel cell, J. Power Sources 211 (2012) 173-176.
[98] K. Cai, C. Wang, W. Pu, Y. Gao, Z. Mao, Investigation of anode flow field for direct dimethyl ether fuel cell, Int. J. Hydrog. Energy, 37 (2012) 12605-12608.
[99] J.-H. Yoo, H.-G. Choi, C.-H. Chung, S.M. Cho, Fuel cells using dimethyl ether, J. Power Sources 163 (2006) 103-106.
[100] Z. Zhang, L. Xin, W. Li, Supported gold nanoparticles as anode catalyst for anion-exchange membrane-direct glycerol fuel cell (AEM-DGFC), Int. J. Hydrog. Energy, 37 (2012) 9393-9401.
[101] Z. Zhang, L. Xin, J. Qi, D.J. Chadderdon, W. Li, Supported Pt, Pd and Au nanoparticle anode catalysts for anion-exchange membrane fuel cells with glycerol and crude glycerol fuels, Appl. Catal. B, 136 (2013) 29-39.

2 Irreversibly Adsorbed Tri-metallic PtBiPd/C Electrocatalyst for the Efficient Formic Acid Oxidation Reaction

2.1 Introduction

Direct formic acid fuel cells (DFAFCs) are considered promising alternative power sources for portable power devices because of their significant advantages, including high theoretical open circuit voltage (1.45 V), low crossover through the polymer membrane, high fuel concentration, low toxicity, and ambient temperature operability [1,2]. A wide range of sources of formic acid production have been mainly from fossil feedstock, but recently, biomass and CO_2 hydrogenation have been studied extensively [3].

The electrocatalysts for both the anode and cathode electrodes are the most important factors affecting the final performance of DFAFCs, and Pt- and Pd based catalysts have been studied widely because of their excellent catalytic activity and long term stability. In particular, Pt is considered the most suitable electrocatalyst among all metals because of its excellent stability [4, 5]. On the other hand, CO-poisoning on the Pt surface by the dehydration pathway of HCOOH oxidation degrades its catalytic activity, which limits its use. The strong CO adsorption energy at low potential is responsible for the abundant CO adsorbed on the Pt surface [6, 7]. The introduction of second metals, such as Bi [8], Ir [9], and Ru [10], can enhance the tolerance of Pt from CO poisoning by promoting CO_2 formation directly or facilitating the CO oxidation reaction, which is due to either the synergistic catalytic effect or electronic structural effect.

Bismuth (Bi) is considered the most efficient modifier of the Pt catalyst for the HCOOH oxidation because of its third-body effect and electronic effect on the Pt surface [11-14]. Herrero et al. reported that Bi-modified Pt exhibited improved electrocatalytic activity and stability because of the synergistic effects of Bi in cleaving the O-H bond and Pt causing C-H bond scission [14]. In addition, Bi can promote the direct pathway (dehydrogenation) of HCOOH, which can reduce the extent of CO poisoning of Pt. On the other hand, Bi can be easily leached out from the electrode surface or oxidized to Bi_2O_3 at potentials over 0.8 V (vs. Ag/AgCl) in acid solution, which means that the Bi-modified Pt catalyst is so unstable when used at high potentials [12, 15]. Recently, Pt-based tri-metal electrocatalysts, including PtPdAu [16], PtCuBi [17], and PtRuSn [18], have been studied widely to overcome such problems. Pd can be a good choice for the third element of the PtBi catalyst because Pd is very stable under acid conditions because of its stable electronic structure. In addition, BiPd [19,20], PdPt [21,22], and BiPt [13] catalysts could prevent the poisoning of Pt by CO due to the less CO chemisorption by the downshift of the d-band center.

In this study, PtBi/C and PtBiPd/C electrocatalysts were synthesized by the irreversible adsorption of Pd and Bi on a 10 wt. % commercial Pt/C catalyst followed by the $NaBH_4$ reduction. The irreversible adsorption is a simple preparation process that can avoid the complicated alloying procedures. In addition, alloy structures can be easily prepared without altering the bulk properties [10, 11]. The introduction of Bi enhanced the direct formic acid oxidation over the indirect oxidation pathway. In addition, Pd increased the oxidation potential of Bi from 0.9 to 1.2 V (vs. Ag/AgCl), which resulted in highly improved electrocatalytic activity in HCOOH oxidation.

2.2 Experiment

2.2.1 Catalyst synthesis

The PtBi/C and PtBiPd/C electrocatalysts were synthesized by the irreversible adsorption of Pd and Bi ions to commercial Pt/C followed by the reduction of metal ions. First, a 10 mM Bi solution was prepared by dissolving bismuth oxide (Sigma-Aldrich, USA) with 20 ml of 0.1 M $HClO_4$. To synthesize the PtBiPd/C, mixed solutions of 10 mM of Bi and 0.5 mM of Pd ions were prepared by dissolving bismuth oxide and $Pd(NO_3)_2$ (Sigma-Aldrich, USA) with 20 mL of 0.1 M $HClO_4$. The above solutions were kept at room temperature for 10 days to stabilize them. The irreversible adsorption of Bi ions or Pd and Bi ions was performed by adding 50 mg of commercial 10 wt. % Pt/C (Alfar Aesar, UK) to the above solutions with stirring (400 rpm) using a hotplate stirrer for 10 hours at 40^{o}C and then were reduced by 0.019 M $NaBH_4$ (Dae-Jung Chemicals & Metals Co., Ltd, Korea) for 30 min. It was washed several times with 0.1 M $HClO_4$ solution followed by a drying at 70^{o}C for 3 h in a vacuum oven.

2.2.2 Instrumental analysis

X-ray diffraction (XRD PANalytical X'Pert Pro MPD, Malvern Panalytical, USA) of the commercial Pt/C, PtBi/C, and PtBiPd/C was performed using 40 kV Cu Kα radiation. The scanning rate and 2θ range was 10^{o}/min and 0–100^{o}, respectively. The morphology was examined by high-resolution transmission electron microscopy (HR-TEM, JEOL JEM-2100F, USA). X-ray photoelectron spectroscopy (XPS, ESCALAB 250Xi Thermo Fisher Scientific, USA) was performed using an Al Kα X-ray source. Cyclic voltammetry (CV) was recorded on a SP-50 (Bio-Logic, USA).

2.2.3 Electrochemical evaluation

Catalyst ink was prepared by mixing 0.5 mg of catalyst powder with 1 ml of ethanol and 1 mg of Nafion (5 wt. %, Sigma-Aldrich, USA). After 30 min sonication, 10 μL of the paste was spread on the GC electrode with a micropipette and dried using a hot air drier for 15 min.

Electrochemical tests were conducted at room temperature in a three-electrode-system using an Ag/AgCl (sat. KCl) reference electrode and a Pt wire counter electrode. H_2SO_4 (0.5 M) was used as an electrolyte solution and the electrode was subjected to potential cycling from -0.2 V to 1.2 V with a 10 mVs^{-1} scan rate. The 0.1 M formic acid oxidation was performed in 0.5 M H_2SO_4 with potential cycling from -0.25 V to 1.2 V at 20 mVs^{-1} scan rate.

2.3 Results and Discussion

As shown in Figure 2.1 and summarized in Table 2.1, the metal nanoparticles were anchored evenly over the carbon support and the particle size Pt/C did not change significantly after the irreversible adsorption of Bi, or Pd and Bi, which suggests that Pd and Bi are only slightly adsorbed on the Pt surface. Figure 2.2 presents XRD patterns of the Pt/C, PtBi/C, and PtBiPd/C. The broad XRD peaks at approximately 40, 46, 67, and 80° 2θ were assigned to the Pt(111), (200), (220), and (311) planes, respectively. The XRD patterns of PtBi/C were similar because the characteristic peaks of Bi almost overlapped with (Figure 2.2b) [20, 23]. The lattice parameters of the catalysts were calculated based on Bragg's law and the Scherrer formula using the (111) XRD peak, as summarized in Table 2.2.

The lattice constant of the PtBi/C was larger than that of Pt/C because of the larger atomic size of Bi than Pt (Table 2.2). Similarly, the smaller lattice constant of PdBiPt/C than that of PtBi/C can be due to the smaller atomic size of Pd than Pt and Bi. The variations of the lattice constant and crystallite size of various catalysts suggest the formation of alloy structures in the PtBi/C and PdBiPt/C catalysts [24].

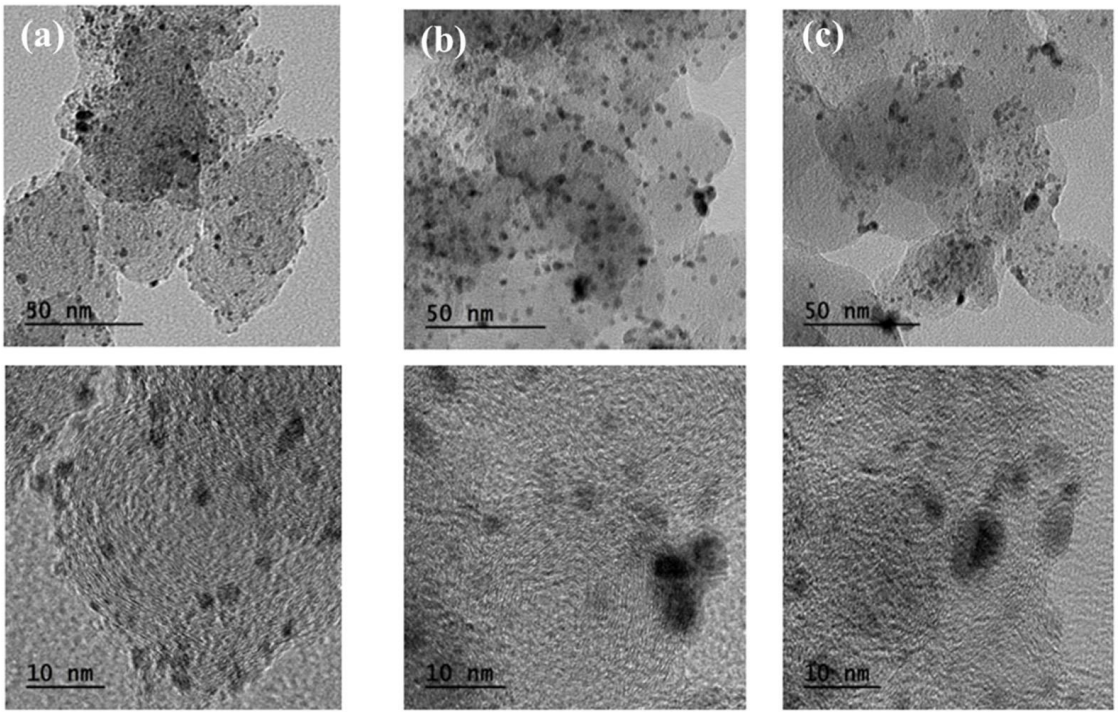

Figure 2.1 TEM images of (a)Pt/C, (b)PtBi/C and (c)PtBiPd/C.

Table 2.1 Particle size of metal nanoparticles in the Pt/C, BiPt/C and PdBiPt/C.

Catalyst	Particle size (nm)
Pt/C	2.5±0.5
PtBi/C	2.8±0.4
PtBiPd/C	2.4±0.8

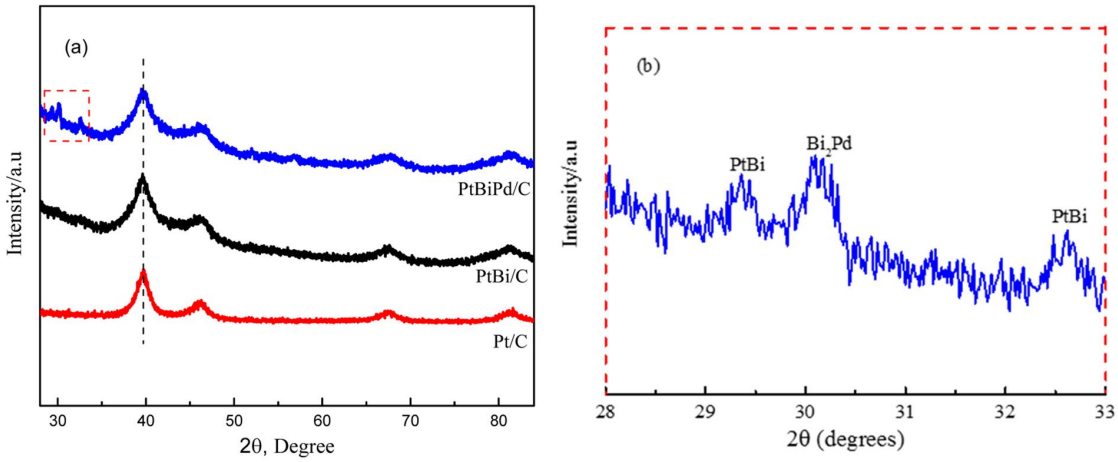

Figure 2.2 (a) XRD patterns of Pt/C, PtBi/C, PtBiPd /C. (b) Enlarged XRD pattern of the red box of (a).

Table 2.2 Crystalline sizes and lattice constants of the various catalysts based on XRD.

Catalyst	Particle size (nm)	Lattice constant(Å)
Pt/C	5.8	3.936
PtBi/C	3.5	4.058
PtBiPd/C	3.4	3.983

XPS was performed to examine the chemical structures of various catalysts. As shown in the XPS survey spectra of Figure 2.3, Pt, Bi, and C peaks except for Pd were observed in each corresponding catalyst. Generally, it is very difficult to observe the Pd peak, particularly when the content is very small because its position overlaps with those of Pt and C. As shown in Figures 2.3b-3d, the Pt 4f7/2 peak can be deconvoluted to two sub-peaks at approximately 71.5 and 72.9 eV, corresponding to Pt (0) and Pt(II), respectively [25]. The Bi 4f7/2 also can be deconvoluted into two sub-peaks at approximately 158 and 160 eV, which correspond to Bi(0) and Bi(III), respectively [26]. As summarized in Table 2.4, Bi(0) is dominant in both PtBi/C and PtBiPd/C, which indicates that Bi_2O_3 was almost reduced to Bi. Therefore, metallic Bi can be dominant on the catalyst surface. Interestingly, the Pt 4f peak shifted slightly toward a higher binding energy, as shown in Figure 2.4a, indicating the formation of an alloy structure between Pt and Bi. Similarly, the peak shift of Bi 4f to a lower binding energy indicated the formation of an alloy structure between Pd and Bi, as shown in Figure 2.4b [27].

The electrochemical performance was examined by CV. As shown in Figure 2.5, the hydrogen region below 0.0 V and Pt oxidation/reduction peak at ~ 0.8 and ~0.5 V were observed clearly for the Pt/C catalyst. When Bi was adsorbed on the Pt/C catalyst, the current related to the hydrogen region and Pt oxidation/reduction decreased because Bi atoms cover the Pt sites. The PtBiPd/C catalyst showed a further decrease in the current of the hydrogen region and a shift of the reduction potential to a lower potential than that of BiPt/C, which indicates alloy formation in the PdBiPt/C. The formic acid oxidation reaction was performed using a range of catalysts in a 2 M HCOOH and 0.5 M H_2SO_4 solution. Generally, formic acid is oxidized to CO_2 via two pathways [1].

i) Direct oxidation pathway (dehydrogenation)

$$HCOOH \rightarrow CO_2 + 2H^+ + 2e^-$$

ii) Indirect oxidation pathway (dehydration, poisoning)

$$HCOOH \rightarrow CO_{ads} + H_2O$$

$$CO_{ads} + H_2O \rightarrow CO_2 + 2H^+ + 2e^-$$

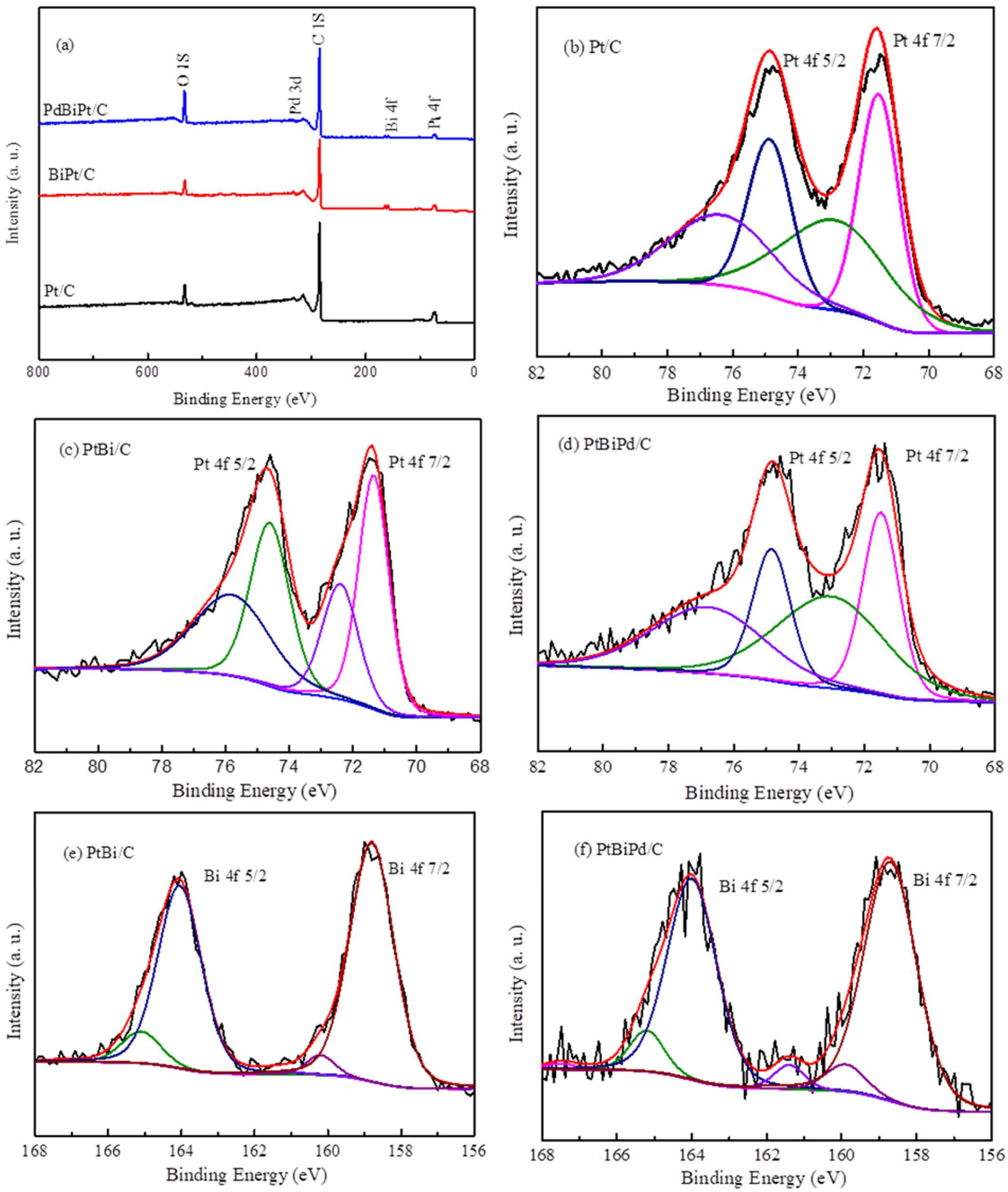

Figure 2.3 (a) XPS survey spectra of Pt/C, PtBi/C and PtBiPd/C. High resolution XPS Pt 4f spectra of (b) Pt/C, (c) PtBi/C and (d) PtBiPd/C. High resolution XPS Bi 4f spectra of (e) PtBi/C and (f) PtBiPd/C.

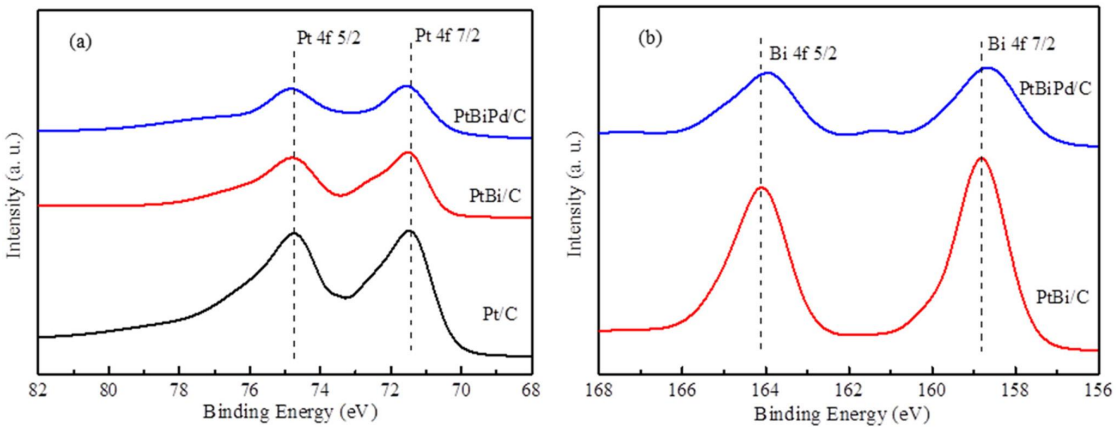

Figure 2.4 (a) High resolution Pt 4f XPS peaks of various catalysts. (b) High resolution Bi 4f XPS peaks of various catalysts.

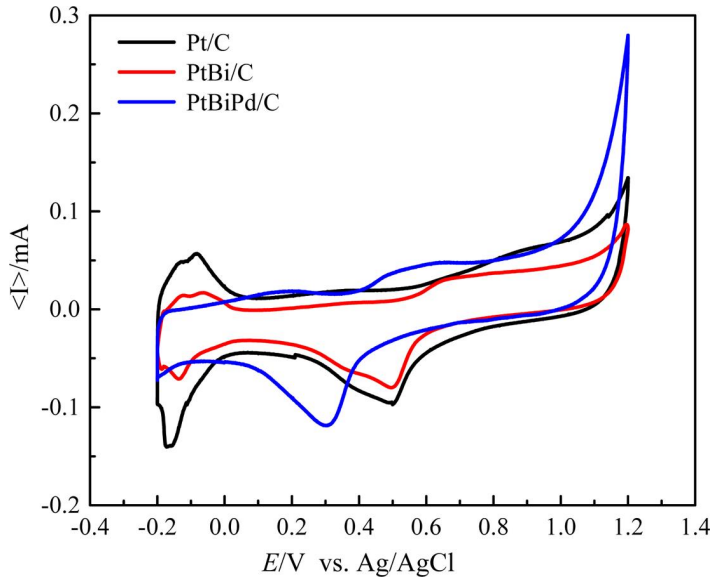

Figure 2.5 CV of Pt/C, PtBi/C and PtBiPd/C (0.5 M H2SO4, scan rate =10 mV/s).

As shown in Figure 2.6, two oxidation peaks in the positive scan were observed, which correspond to the direct and indirect oxidation reaction pathways. The commercial Pt/C catalyst showed poor formic acid oxidation activity due to CO poisoning by the formation of COads on the Pt surface. Instead, the PtBi/C and PtBiPd/C catalysts exhibited enhanced electrocatalytic activity. As summarized in Tables 2.3 and 2.4, the current of direct formic acid oxidation (I_d) increased ~ 8 and 16 folds for the PtBi/C and PtBiPd/C catalysts compared to that of commercial Pt/C because of the electronic, geometric, and third body effects [20,27], which are higher values than those of previous studies [16,17]. In addition, the higher ratio between I_d and the current of indirect formic acid oxidation (I_{ind}) for the PtBi/C and PtBiPd/C catalysts indicates that the dehydrogenation pathway is dominant with less CO formation on these catalysts. To examine the effects of Pd on formic acid oxidation, the scan range was varied, especially for the upper potential limit (UPL), because it can affect the reverse scan peak by the leaching of metal at high potential. As shown in Figure. 7a, in the case of the PtBi/C catalyst, the maximum current of reverse scan increases initially with increasing UPL because of the oxidation of the CO_{ads} at high potential. The reverse scan current was highest when the UPL was 0.8 V and decreased from 0.9 V, which is due to Bi leaching out at high potential [21,23,24]. Instead, in the case of the PtBiPd/C catalyst, the maximum reverse scan current was highest at 1.1 V of the UPL, which means that Bi leaching occurs at a higher potential than that of the PtBi/C catalyst by the co-adsorbed Pd [29], which can be attributed to the formation of the PdBi alloy structure that has a strong resistance against Bi leaching [30].

2.4 Conclusions

PtBi/C and PtBiPd/C catalysts were synthesized by the irreversible adsorption of Pd and Bi using Bi_2O_3, $Pd(NO_3)_2$ as precursors on commercial Pt/C followed by $NaBH_4$ reduction. Instrumental analysis showed that the alloy structure was formed among Pt, Bi, and Pd. The Bi atoms enhanced the direct formic acid oxidation reaction and Pd atoms improved the resistance against Bi bleaching at high potential, which strongly improved the overall formic oxidation reaction.

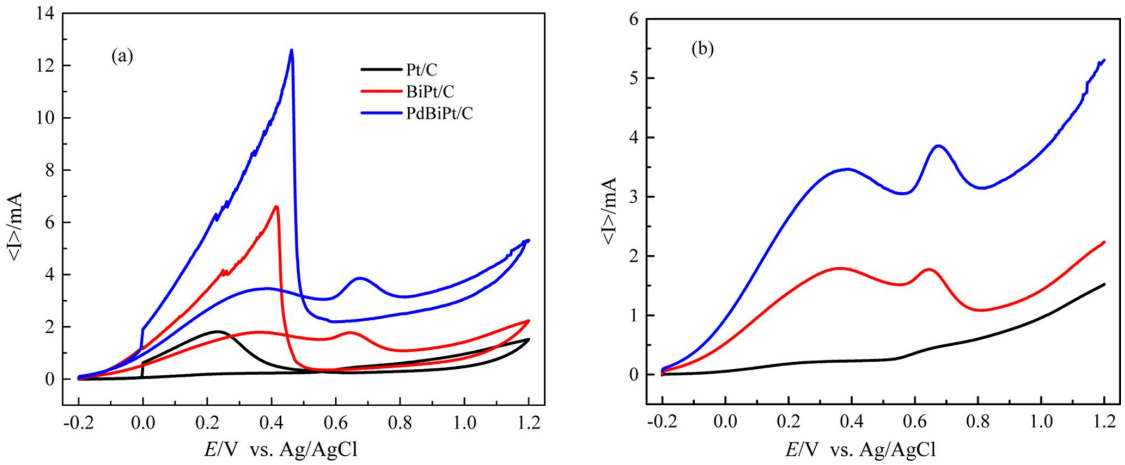

Figure 2.6 (a) CV obtained at Pt/C, PtBi/C and PtBiPd/C catalysts. (b) Forward scan of formic acid oxidation on the different catalysts. The solution contains 0.5 M H_2SO_4 and 2 M HCOOH. The scan rate was 20 mV/s.

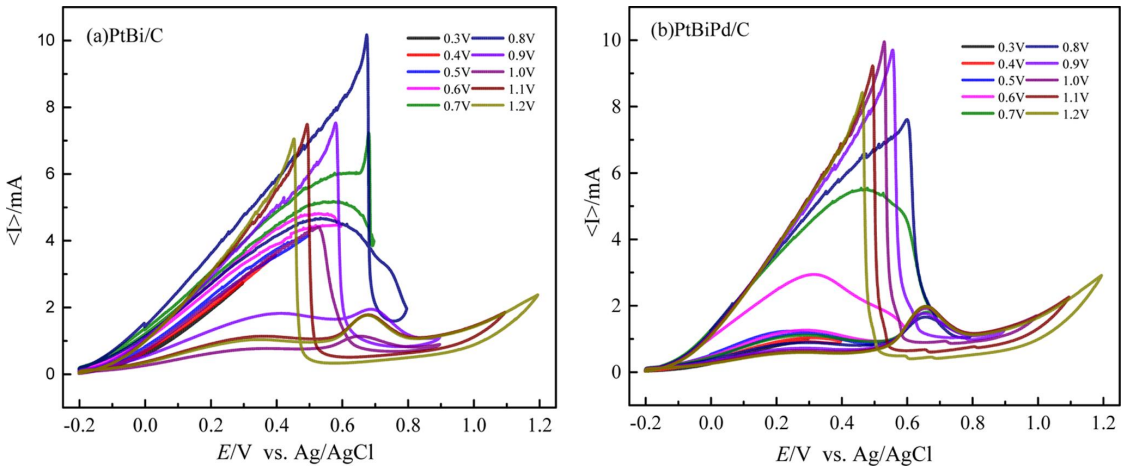

Figure 2.7 CV obtained at (a) BiPt/C and (b) Pt/BiPd/C catalysts. The voltage was swept from -0.20 to 1.2 V with an increasing step of 0.1 V. The solution contained 0.5 M H_2SO_4 and 2 M HCOOH. The scan rate was 20 mV/s.

Table 2.3 Binding energies and relative intensities of the different chemical states of Pt 4f7/2 and Bi 4f 7/2 in the Pt/C, PtBi/C and PtBiPd/C catalysts.

Sample	Species	Binging energy (eV)	Relative intensity (%)
Pt/C	Pt(0)	71.5	51
	Pt(II)	72.9	49
PtBi/C	Pt(0)	71.4	57
	Pt(II)	72.4	43
	Bi(0)	158.8	91
	Bi(III)	160.2	9
PtBiPd/C	Pt(0)	71.5	40
	Pt(II)	73.1	60
	Bi(0)	158.7	90
	Bi(III)	160.0	10

Table 2.4 Formic acid oxidation current of various catalysts.

Sample	First Peak (I_d) (mA)	Second Peak (I_{ind}) (mA)	Reverse scan peak (mA)	I_d/I_{ind}
Pt/C	0.21	0.45	1.80	0.46
10 mM PtBi/C	1.78	1.77	6.59	1.01
0.5 mM PtBiPd/C	3.46	3.85	12.59	0.89

Table 2.5 The comparison of formic acid oxidation peak current for the various catalysts

	PtBiPd/C This work	PtPdAu/C Ref [16]	Pt1Pd3Cu3/C Ref [17]
I(Pt/C),mA	0.21	0.50	0.17
I(PtMN/C), mA	3.46	1.30	1.16
I(PtMN/C) / I(Pt/C)	16	3	7

References

[1] C. Rice, R.I. Ha, R.I. Masel, P. Waszczuk, A. Wieckowski, T. Barnard, Direct formic acid fuel cells, J. Power Sources, 111 (2002) 83–89.

[2] B.C. Ong, S.K. Kamarudin, S. Basri, Direct liquid fuel cells: A review, Int. J. Hydrogen Energy, 42 (2017) 10142-10157.

[3] M. Grasemann, G. Laurenczy, Formic acid as a hydrogen source–recent developments and future trends, Energy Environ. Sci., 5 (2012) 8171-8181.

[4] P. Hong, F. Luo, S. Liao, J. Zeng, Effects of Pt/C, Pd/C and PdPt/C anode catalysts on the performance and stability of air breathing direct formic acid fuel cells, Int. J. Hydrogen Energy, 36 (2011) 8518-8524.

[5] K. Jiang, H.X. Zhang, S. Zou, W.B. Cai, Electrocatalysis of formic acid on palladium and platinum surfaces: from fundamental mechanisms to fuel cell applications, Phys. Chem. Chem. Phys., 16 (2014) 20360-20376.

[6] W. Gao, J.A. Keith, J. Anton, T. Jacob, Theoretical elucidation of the competitive electro-oxidation mechanisms of formic acid on Pt (111), JACS, 132 (2010) 18377-18385.

[7] E. Herrero, J.M. Feliu, Understanding formic acid oxidation mechanism on platinum single crystal electrodes, Curr. Opin. Electrochem., 9 (2018) 145-150.

[8] J.K. Yoo, M. Choi, S. Yang, B. Shong, H.-S. Chung, Y. Sohn, C.K. Rhee, Formic acid electrooxidation activity of Pt and Pt/Au catalysts: Effects of surface physical properties and irreversible adsorption of Bi, Electrochim. Acta, 273 (2018) 307-317.

[9] W. Chen, S. Chen, Iridium-platinum alloy nanoparticles: Composition-dependent electrocatalytic activity for formic acid oxidation, J. Mater. Chem. A, 21 (2011) 9169-9178.

[10] E.N. El Sawy, P.G. Pickup, Formic Acid Oxidation at Ru@Pt Core-Shell Nanoparticles, Electrocatalysis, 7 (2016) 477-485.

[11] M. Choi, C.-Y. Ahn, H. Lee, J.K. Kim, S.-H. Oh, W. Hwang, S. Yang, J. Kim, O.-H. Kim, I. Choi, Y.-E. Sung, Y.-H. Cho, C.K. Rhee, W. Shin, Bi-modified Pt supported on carbon black as electro-oxidation catalyst for 300 W formic acid fuel cell stack, Appl. Catal., B, 253 (2019) 187-195.

[12] J.D. Lović, S.I. Stevanović, D.V. Tripković, A.V. Tripković, R.M. Stevanović, V.M. Jovanović, K.D. Popović, Insight into electrocatalytic stability of low loading Pt-Bi/GC and Pt/GC clusters in formic acid oxidation, J. Solid State Electrochem., 19 (2015) 2223-2233.

[13] X. Yuan, X. Jiang, M. Cao, L. Chen, K. Nie, Y. Zhang, Y. Xu, X. Sun, Y. Li, Q. Zhang, Intermetallic PtBi core/ultrathin Pt shell nanoplates for efficient and stable methanol and ethanol electro-oxidization, Nano Res., 12 (2018) 429-436.

[14] J.V. Perales-Rondon, A. Ferre-Vilaplana, J.M. Feliu, E. Herrero, Oxidation mechanism of formic acid on the bismuth adatom-modified Pt(111) surface, JACS, 136 (2014) 13110-13113.

[15] D.R. Blasini, D. Rochefort, E. Fachini, L.R. Alden, F.J. DiSalvo, C.R. Cabrera, H.D. Abruña, Surface composition of ordered intermetallic compounds PtBi and PtPb, Surf. Sci., 600 (2006) 2670-2680.

[16] C. Li, H. Wang, Y. Li, H. Yu, S. Yin, H. Xue, X. Li, Y. Xu, L. Wang, Tri-metallic PtPdAu mesoporous nanoelectrocatalysts, J. Nanotechnol., 29 (2018) 11762-117625.

[17] M.A. Ud Din, F. Saleem, B. Ni, Y. Yong, X. Wang, Porous Tetrametallic PtCuBiMn Nanosheets with a High Catalytic Activity and Methanol Tolerance Limit for Oxygen Reduction Reactions, Adv. Mater., 1604994 (2017) 1-8.

[18] J.S. Yoo, H.T. Kim, H.-I. Joh, H. Kim, S.H. Moon, Preparation of a CO-tolerant PtRuxSny/C electrocatalyst with an optimal Ru/Sn ratio by selective Sn-deposition on the surfaces of Pt and Ru, Int. J. Hydrogen Energy, 36 (2011) 1930-1938.

[19] R.W. Atkinson, S. St. John, O. Dyck, K.A. Unocic, R.R. Unocic, C.S. Burke, J.W. Cisco, C.A. Rice, T.A. Zawodzinski, A.B. Papandrew, Supportless, Bismuth-Modified Palladium Nanotubes with Improved Activity and Stability for Formic Acid Oxidation, ACS Catal., 5 (2015) 5154-5163.

[20] H. Xu, B. Yan, K. Zhang, J. Wang, S. Li, C. Wang, Y. Du, P. Yang, S. Jiang, S. Song, N-doped graphene-supported binary PdBi networks for formic acid oxidation, Appl. Surf. Sci., 416 (2017) 191-199.

[21] H.-X. Zhang, C. Wang, J.-Y. Wang, J.-J. Zhai, W.-B. Cai, Carbon-supported Pd− Pt nanoalloy with low Pt content and superior catalysis for formic acid electro-oxidation, J. Phys. Chem. C, 114 (2010) 6446-6451.

[22] B. Gralec, A. Lewera, Catalytic activity of unsupported Pd-Pt nanoalloys with low Pt content towards formic acid oxidation, Appl. Catal., B, 192 (2016) 304-310.

[23] H. Liao, J. Zhu, Y. Hou, Synthesis and electrocatalytic properties of PtBi nanoplatelets and PdBi nanowires, Nanoscale, 6 (2014) 1049-1055.

[24] Y. Suo, Synthesis of Highly Active Pt-Pd-Cu/C Catalysts for Formic Acid Oxidation, Int. J. Electrochem. Sci., 12 (2017) 3561-3575.

[25] J.-N. Zheng, J.-J. Lv, S.-S. Li, M.-W. Xue, A.-J. Wang, J.-J. Feng, One-pot synthesis of reduced graphene oxide supported hollow Ag@Pt core–shell nanospheres with enhanced electrocatalytic activity for ethylene glycol oxidation, JACS, 2 (2014) 3445-3451.

[26] A. Zalineeva, A. Serov, M. Padilla, U. Martinez, K. Artyushkova, S. Baranton, C. Coutanceau, P.B. Atanassov, Self-supported Pd(x)Bi catalysts for the electrooxidation of glycerol in alkaline media, JACS, 136 (2014) 3937-3945.

[27] P. Kiatkittikul, J. Yamaguchi, T. Nohira, R. Hagiwara, Catalytic Activities of Pt– Metal Alloys on Oxygen Reduction Reaction in Fluorohydrogenate Ionic Liquid, Electrochemistry, 84 (2016) 766-768.

[28] F. Alardin, P. Ruiz, B. Delmon and M. Devillers, Bismuth-promoted palladium catalysts for the selective oxidation of glyoxal into glyoxalic acid, Appl. Catal., A 2001, 215, 125-136.

[29] M. Besson, F. Lahmer, P. Gallezot, P. Fuertes and G. Fleche, Catalytic oxidation of glucose on bismuth-promoted palladium catalysts, J. Catal. 1995, 152, 116-121

3 Irreversibly Adsorbed Tri-metallic PtPdRu/C Electro-catalyst for the Efficient Formic Acid Oxidation Reaction

3.1 Introduction

Recently, low-temperature fuel cells have attracted extensive attention due to the decreasing of fossil fuels, environmental degradation, and increasing energy demand [1,2]. For example, phosphoric acid fuel cell (PAFC), polymer electrolyte membrane fuel cell (PEMFC), direct methanol fuel cell (DMFC) or direct formic acid fuel cell (DFAFC) are potential alternative power sources for portable power devices [3], among methanol has been researched as anode materials. However, much attention has turned to formic acid (HCOOH) instead of methanol, because HCOOH shows lower crossover flux through Nafion membranes [4, 5], a higher fuel concentration, no toxic and at ambient temperature and thus it is safe in handing as a rational liquid electrolyte at room temperature [6]. The DFAFC uses an air cathode and formic acid anode, direct oxidation of formic acid releases two electrons per molecule. The cathode, anode and overall reactions of a direct formic acid fuel cell are shown as:

Anode: $HCOOH \rightarrow CO_2+2H^++2e^-$ (1)

E_0=-0.25V （vs.SHE）

Cathode: $1/2O_2+2H^++2e^- \rightarrow H_2O$ (2)

E_0=1.23V （vs.SHE）

Overall: $HCOOH + 1/2O_2 \rightarrow CO_2+H_2O$ (3)

OCV=1.48V

The DFAFC has a higher open circuit voltage 1.48V (values vary slightly depending on the source) [2]. In previous works, anode and cathode play roles in the determination of the fuel cell performance. It has been commonly accepted that HCOOH is oxidized to CO_2 by a dual mechanism, an indirect path (CO pathway) and direct path (CO_2 pathway) [7-13]. The indirect pathway is forming adsorbed carbon monoxide (CO) as a poison reaction intermediate, thus the absence of CO is always as an important characteristic in fuel cell reactions [5, 13, 14], Pt/C, Pd/C, and PtPd/C are potential anodic catalysts for electro-oxidation of formic acid (FAO). The workers thought PdPt/C catalyst is more promising for FAO [15]. Because Pd/C and PdPt/C was most probably to react via the direct pathway, therefore it has higher OCV than Pt/C, but poor stability for Pd/C though the highest catalytic activity in the initial reaction [16]. The presence of a Pd layer on the surface of carbon supported PdPt particles due to the

lower surface energy of Pd and the higher cohesive energy of Pt. This layer may present CO adsorption properties [17, 18], the further electro-oxidation of CO has occurred oxygen-containing species clustered onto nearby Ru atoms, in which have weak adsorption for CO, but Ru sites have a strong affinity for OH [19, 20]. Hence the adsorption of ruthenium(Ru) on Pd (111) leads to a significate increase of electrocatalytic activity [21-24].

In this work, RuPdPt/carbon black electrocatalyst was synthesized by using platinum nominally 10% on carbon black (Alfa Aesar) as the catalyst support and palladium and ruthenium precursor that prepared by $NaBH_4$ reduction method [3, 25, 26]. Characterized and tested by XRD analysis, XPS, TEM image and Cyclic Voltammetry (CV) indicated RuPdPt C catalyst enhances activity for FAO significantly. RuPd(111) and Pd(111) slab were built due to exiting the low Ru and high Pd content, and Pd is to form a layer on the surface [18]. Density functional theory (DFT) calculation suggests that OH species of water dissociation can promote CO further oxidation to CO_2.

3.2 Experiment

3.2.1 Catalyst synthesis

The PdPt /C and RuPdPt /C electrocatalyst was prepared by irreversible adsorption method in the literature. Platinum, nominally 10% on carbon black (South Korea Alfa Aesar Chemical) was used as the Pt/C support. The PdPt/C was produced as follow: a solution of bismuth oxide (Sigma-Aldrich, USA) 10 mM was prepared by dissolving 20 mL of 0.1 mol $HClO_4$ (2) 50 mg commercial Pt/C added solution in strong stirring (400 rpm) by hotplate stirrer 10 hours (3) mixed solution was filtered 4~5 times in 0.1 mol $HClO_4$ (4) a 0.019 M solution of $NaBH_4$ (DAE JUNG CHEMICALS & METALS CO, LTD) was slowly added with strong stirring half hour and was filtered 3 times in 0.1mol $HClO_4$ (5) the PdPt /C was filtered and dried，0.1 mM, 0.2mM, 0.5 mM $RuCl_3$ as precursor with 10 mM palladium oxide deposition on Pt/C was accomplished in a way same to Pd deposition on Pt/C.

3.2.2 Physical characterization

X-ray diffraction (XRD) patterns of the as-prepared Pt/C supported catalyst and commercial Pt/C were characterized using the PANalytical X'Pert Pro MPD powder with Cu Kα radiation at 40 kV and 30 mA. The scanning rate was 10.0000 deg./min and the 2θ range was 0–100°. The morphology was recorded by high-resolution transmission electron microscopy （HR-TEM, JEOL JEM-2100F, USA）X-ray photoelectron spectroscopy (XPS) equipped with an Al Kα monochromatic x-ray source (1486.6 eV, 45◦ incident angle) was employed on

the PdPt/C, RuPdPt/C, and the commercial Pt/C samples. Cyclic voltammetry (CV) was reported by SP-50 (Bio-Logic Science Instruments SAS France)

3.2.3 Electrode preparation

Catalyst ink was prepared by mixing of 0.005 g of catalyst powder, 1 ml of ethanol and 0.01 g of Nafion (5 wt %). After 30 min sonication, 10 µL of paste was spread on the GC electrode and dried under hot air drier for 15 mins. 10 µL commercial 10% Pt/C coated for Formic acid, For CV 10 µL of paste was used to compare with all catalyst.

3.2.4 Electrochemical characterization

All catalysts were opted by a Pine Bipotentiostat to conduct at room temperature in a three-electrode-system using an Ag/Agcl (sat. Kcl) reference electrode and a Pt wire conter electrode; all potentials in the manuscript are converted the reversible hydrogen electrode (RHE). The fixed-disk area is 1.13 cm^2 and the OD disk area is 0.196cm^2. All cyclic voltammograms (CVs) were characterized under the same conditions. 0.5 M H_2SO_4 as electrolyte solution and electrode was subjected to potential cycling from -0.2 V to 1.2 V by scan rate of 10 mV s^{-1}. The ORR voltammogram was characterized 0.1 M formic acid in 0.5m H_2SO_4 as electrolyte solution with potential cycling from -0.25 V to 1.2 V by scan rate of 50 mV s^{-1}.

3.2.5 Density functional theory (DFT) calculations

RuPd(111) catalyst have been obtained by the substitutional single atom Ru(111) into the Pd(111) layer. The Pd and RuPd slab were built by using a periodic four-layer slab with a p (4×4) super cell with 16 atoms at each layer with a 12Å-vacuum layer to ensure that the adsorbates (*OH and *CO). All DFT calculations were came true by suing Vienna ab initio simulation package (VASP) [27, 28] by using the generalized gradient approximation (GGA) with Perdew-Burke-Ernzerhof (PBE) exahange-correlation functional [29], which use the projector augmented wave (PAW)[30, 31] method and a plane-wave basis set with a kinetic energy cutoff of 400eV for vacuum.[32, 33] In tergrations in reciprocal space used a 3 ×3 ×1 k-points for Brillouin-zone sampling for unit cell.[34] For the adsorption energy (E_{asd}) is defined as:

$$E_{ads} = E_{ads/slab} - E_{ads} - E_{slab}$$

Here E_{slab} is energy of RuPd(111) and Pd(111) slab, E_{asd} is the energy of free adsorbate, and $E_{ads/slab}$ is the total energy of adsorbate-Pd system in the equilibrium state [35].

3.3 Results and discussion

3.3.1 Physical property of catalyst

Figure 3.1 shown transmission electron microscopy (TEM) analysis found that the metal NPs of the Pt/C (a) and PdPt/C (b) samples are anchored evenly over the carbon hosts and have a narrow distribution in average size of 1.2 ~ 3.6 nm, 1.6~ 4.0 nm, respectively. RuPdPt /C is similar to PdPt/C catalysts sizes due to the less content of Ru, the main particle size of Pt/C and PdPt /C 1.6 ~ 2.0 and 2.4~2.8 nm, the thickness of the Pd layer was around 0.8 nm in the Figure 3.1c by HR-TEM, corresponding to the mean particle size difference value of the Pt/C and PdPt/C. The slight increase in particle size may be described that the parts of Pd atoms were deposited on the Pt surface as layers. The phenomenon can be explained as (i) the surface energy of Pd is lower but Pt has a higher cohesive energy [18, 36], (ii) the more electronic conducted of Pt than XC-72R carbon powder, hence Pd^{2+} can be reduced easily by gaining the electrons on the Pt surface [37], (iii)using the commercial Pt/C catalyst in the experiment so the Pt and C existed stable connection, which indicates a formation of Pd in the beginning.

X-ray diffraction (XRD) patterns were shown the structural Pt/C and PdPt/C catalysts in Figure 3.2 the features peaks of the (002) plane of Vulcan XC-72 carbon are very strong at about 25° due to carbon as support. The Pt/C exhibited very strong peaks (green lines) at. Wide-angle X-ray diffraction (WAXD) shows broad peaks at 39.64° (111), 46.24° (200), 67.63° (220), which are characteristic of Pt to indicate their highly crystalline nature. The PdPt/C catalyst has peaked at 39.78°, 46.01° and 67.45° corresponding to 111, 200 and 220, respectively, which exhibited very weak XRD patterns and the values of PdPt/C catalyst slightly shifted to higher 2θ angle compared with Pd standard (orange lines) and the peaks of carbon was weaker on PdPt/C compared with Pt/C patterns. This can be ascribed to homogeneous dispersion of Pd as surface deposition on Pt and carbon. Furthermore, the lattice parameters of the catalysts calculated based on Bragg's law using diffraction peak are shown in Table 3.1. The lattice parameters of the PdPt/C（3.8604 Å）are lower than that of the standard value of Pt (3.9359 Å)/C. There are no obvious diffraction peaks of Pd in XRD patterns indicating formation PdPt alloy [37]. The diffraction peaks of Ru were hardly seldom owing to the low content of Ru. X-ray Photoelectron Spectroscopy (XPS) survey spectra of Pt/C (a), 10 mm PdPt /C (b) and 0.1mm RuPdPt /C (c) for Pt 4f7/2 was showed in Figure 3.3. All Pt 4f7/2 peaks can be deconvolution into two pairs of doublets. The Pt 4f7/2 peaks of PdPt /C and RuPdPt /C shifted to the lower binding energy (71.28 eV) compared with the Pt 4f7/2 peaks of Pt/C (71.48 eV), the Pt 4f7/2 peaks of PdPt/C and RuPdPt/C are almost same owing to the lower content of Ru (0.1 mm).

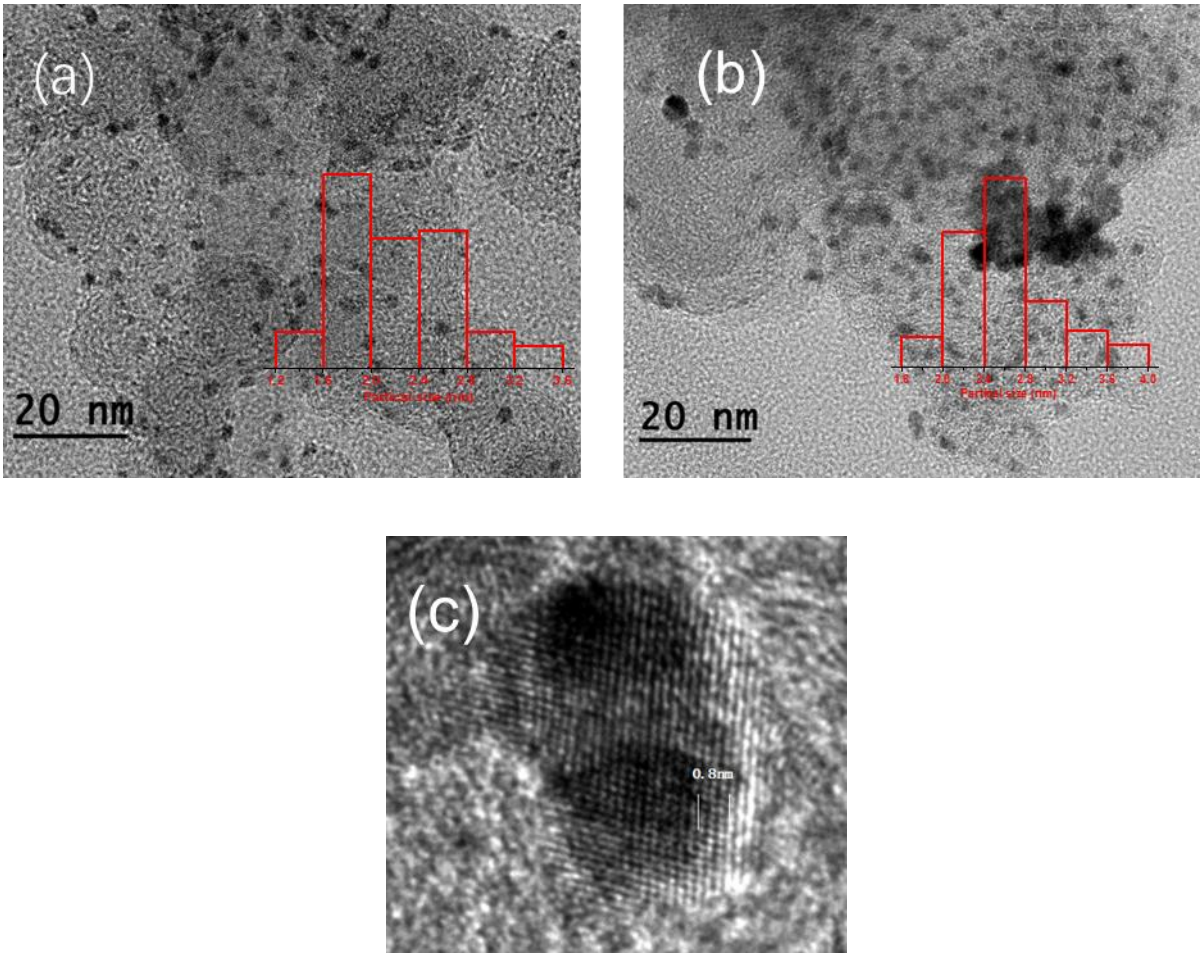

Figure 3.1 TEM and HRTEM micrographs for (a) Pt/C, (b) PdPt/C samples at 20 nm and (c) PdPt/C samples at 5nm

Table 3.1 Crystalline sizes and lattice parameters of the different catalysts based on XRD characterization.

Sample	Crystalline size (nm)	Lattice parameter (Å)
Pt/C	4.2	3.9359
PdPt /C	4.9	3.8604
RuPdPt /C	4.7	3.8707

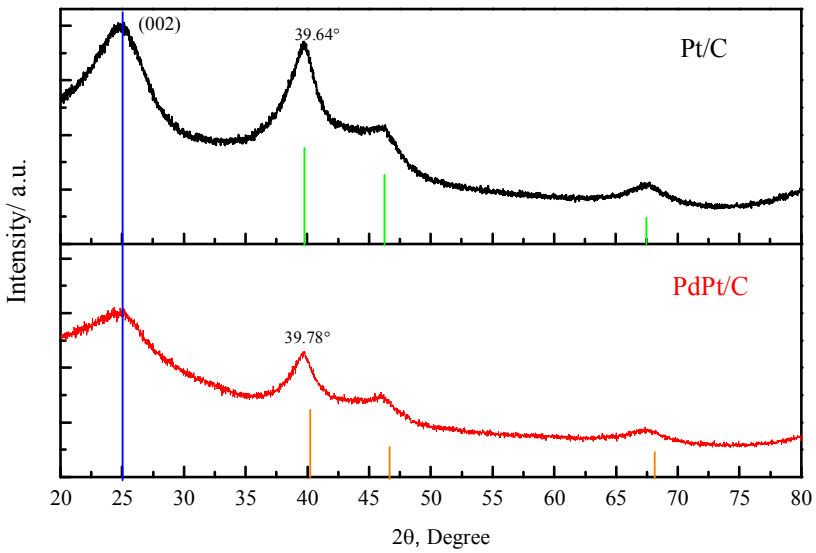

Figure 3.2 Powder X-ray diffraction (XRD) profile of 10wt% Pt/C, 10 Mm PdPt/C catalysts with the Scan speed of 10.0000 deg./min. The standard patterns of Pt and Pd were shown as green and orange vertical lines, respectively.

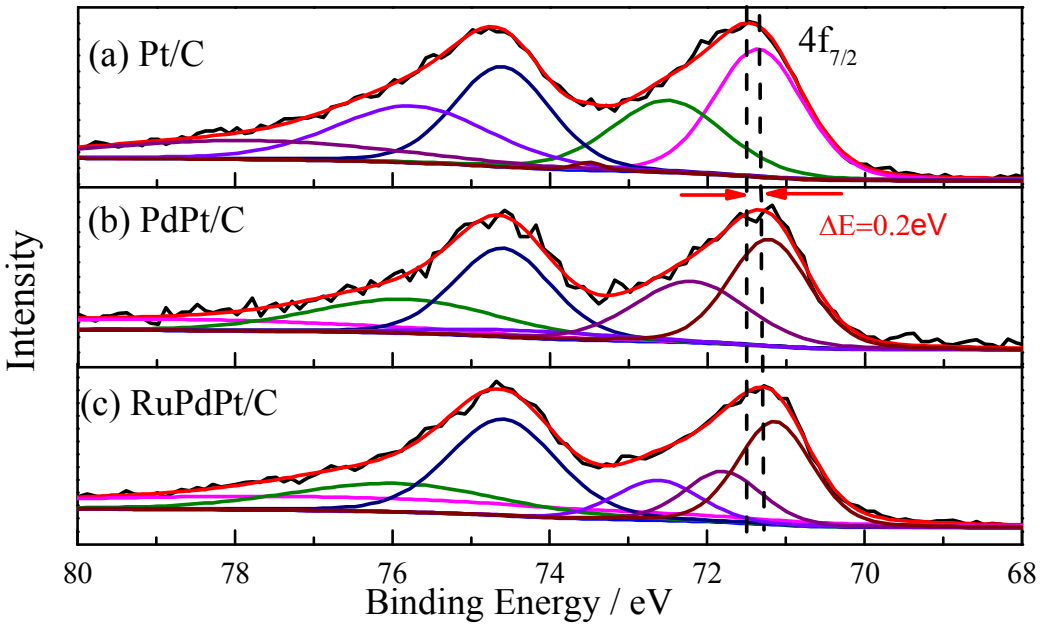

Figure 3.3 X-ray Photoelectron Spectroscopy (XPS) survey spectra of Pt/C (a), 10 mm PdPt /C (b) and 0.1mm RuPdPt /C (c)

3.3.2 Electrochemical property of catalyst

The catalysts were tested for their electrochemical property by using cyclic voltammetry (CV) plots，which is an important measure to demonstrate the surface structure shown Figure 3.4 It can be showed the hydrogen desorption region of catalysts area from -0.2 V to 0V [40], the peak of PdPt/C decrease significantly in H_2 desorption compared with the commercial Pt/C attributing to Pd shell cover the Pt particle, which was further evidence the formation of Pd shell on the Pt surface. Furthermore, the electrochemical surface area (ECSA) of Pt/C (144.35 $m^2g^{-1}Pt$) was much higher than the ECSA (8.14 $m^2g^{-1}Pt$) Pd loading Pt/C, which can be indicated Pd high dispersion led to lower Pt utilization factor [40]. Meanwhile, the peaks of hydrogen desorption region gradually dwindle with the content of Ru exhibited that the Ru load the metal surface even though low content.

The peak of PdPt/C corresponds to the oxidation of catalytic metal with intermediary product metal-OH and metal-O during the positive scan and stripping of oxidized species by negative scan at 0.2V to 1.2V [41]. The peaks of oxidized species reduction shifted to the lower potential owing to the Pd and Ru modified, which exhibited the surface activity increasing further shown the high binding energy with the metal surface. Hence oxidized products divorced from the surface of the catalytic surface in negative potential. RuPdPt /C catalysts have a similar property compare with PdPt/C and Pt/C catalysts. As shown in Figure 3.5a, the formic acid redox reaction voltammograms of Pt/C, PdPt/C, and RuPdPt/C were tested by using CV, which was obtained in 0.5 M H_2SO_4 and 2 M HCOOH with a scan rate of 50 mV s^{-1} at room temperature. The current densities for different catalysts have been shown the curves of the formic acid oxidation reaction. CV typical peaks of formic acid on Pt/C catalyst, with two anodic peaks in the positive scan and one anodic peak in the negative scan can be observed. Formic acid oxidation on Pt follows direct and indirect pathway has been intensively investigated, which includes a dehydrogenation pathway to create CO_2 directly and a dehydration pathway to form intermediates CO [41], a strong peak of oxidation of oxygen species in the negative scan. The first oxidation peak at lower than 0.5 V is formed the dehydrogenation pathway to create CO_2 directly and the oxidation of CO_{ads} at the high potential, the coverage of adsorbed CO species on the active sites of the mental to led catalyst poison. Remove poison species by oxidation of the CO from the metal surface, a large oxidation peak in the negative scan shown the electrocatalytic activity. Figure 3.5b given a detailed explanation for the forward scan linear of different catalysts samples. Direct oxidation peaks of formic acid in around 0.3V have an increasing trend but insignificantly. Ru modified the PdPt/C catalysts have higher current density than PdPt/C catalyst, especially 0.1 mm RuPdPt/C shown the highest peak

current at around 0.5V to 0.8V which is attributed to the indirect pathway of CO_{ads} oxidation to CO_2, which proved the low content Ru modified PdPt/C catalyst can improve the catalytic activity and inhibited CO poison with accelerating the oxidation of CO. Meanwhile, the on-set potential of the RuPdPt/C catalyst (-0.1 V) for FAO is lower than that of PdPt/C catalyst (0.1 V) further evidence that the mingle with Ru can be enhanced electrocatalytic activity.

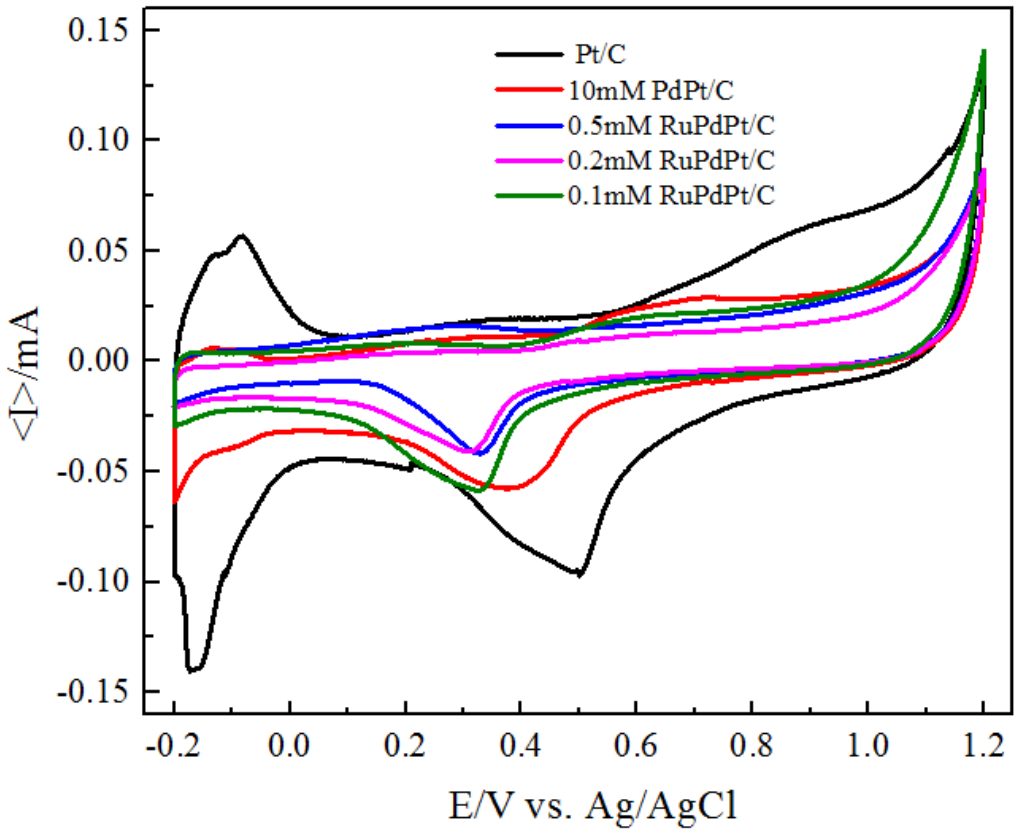

Figure 3.4 Cyclic voltammograms of curves explaining electrocatalytic activity of 10 wt%, Pt/C 10mM Pd with 10 wt% Pt/C and different molarity Ru on PdPt/C at room temperature (in 0.5 m H_2SO_4). Scan rate: 10 mV/s.

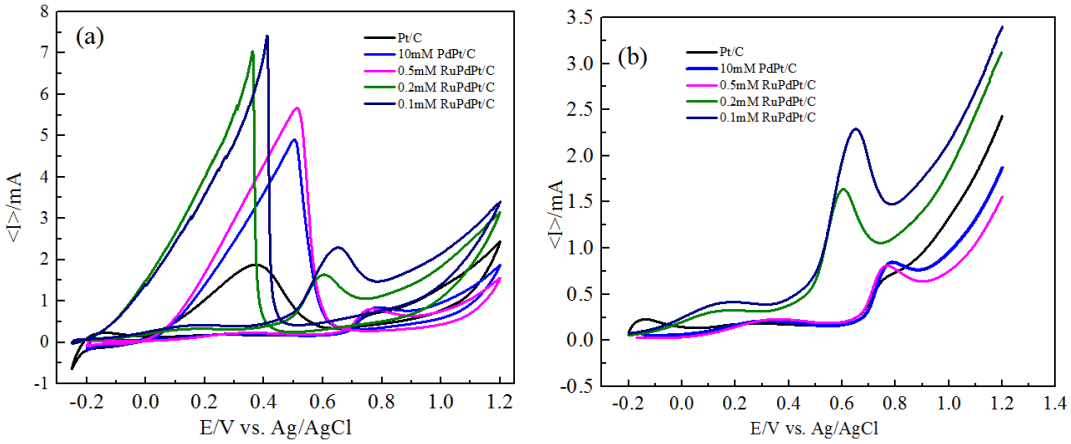

Figure 3.5 (a) CV curves of different catalysts at room temperature with scan rate of 50 mV/s (0.5 M H_2SO_4 with 2 M HCOOH) (b) The forward scan of formic acid oxidation on the different catalysts

3.3.3 *CO Oxidation by *OH of Water

A small amount of *CO is still formed via to other routes though formate as main intermediate of FAO. *CO exist a huge influence for FAO, the concentration in reactants be not allowed over 100 ppm [42]. Catalysis active decreasing due to the *CO has strong adsorption energy for catalysts metal result in catalyst poisoning. Consequently, *CO further translate successfully is key point to keep catalyst good performance. Adsorption CO is from *HCOOH dehydration and *COOH decomposion for FAO, getting *OH from activation water play an important role for *CO oxidation. We built the single atom Ru embedded in the Pd(111) to show the machines of *CO oxidation owing to the a large of Pd on the surface and low content of Ru. The binding energy (BE) of OH is higher on Ru site such as reported by Manos Mavrikakis and co-workers and Pd-CO has a lower BE beside the Ru atom [43, 44]. This is a benefit for CO oxidation and dissociation of water to have both Pd sites for bind CO weakly and Ru sites for bind OH strongly on the catalytic surface. The reaction equation as:

$H_2O + Ru^* \leftrightarrow Ru\text{-}OH + H^+ + e^-$

$Ru\text{-}OH + Pd^* \leftrightarrow Pd\text{-}OH + Ru^*$

$Pd\text{-}CO + Pd\text{-}OH \leftrightarrow CO_2 + H^+ + e^- + Pd^*$

The formation of CO* is the most favored in the low potential attributed to the dehydration reaction (CO^*+H_2O) is exothermal thermodynamically, removed CO* on surface until water is dissociation to OH* at high potential, and Pd mixed Ru more easily to activate water result in the peaks of RuPdPt/C catalysts shifted low potential compared with the PdPt/C catalyst. In addition, the Ru can promote the generation of the first dehydrogenation step of HCOOH, producing COOH* or HCOO* gain more insight that enhances electrocatalytic activity with modified Ru [43]. As shown in Figure 3.6(a), H_2O dissociation on RuPd surface compared with pure Pd surface, where is more favorable for H_2O dissociation on Ru@Pd attributing to Ru-O strong BE, the barrier was changed from 1.10 eV to 0.78 eV, the relative energy also was decreased from 0.32 eV to 0.01 eV, it means that the number of *OH will be generated at a lower potential in an electrochemical environment from dynamic and thermodynamically.

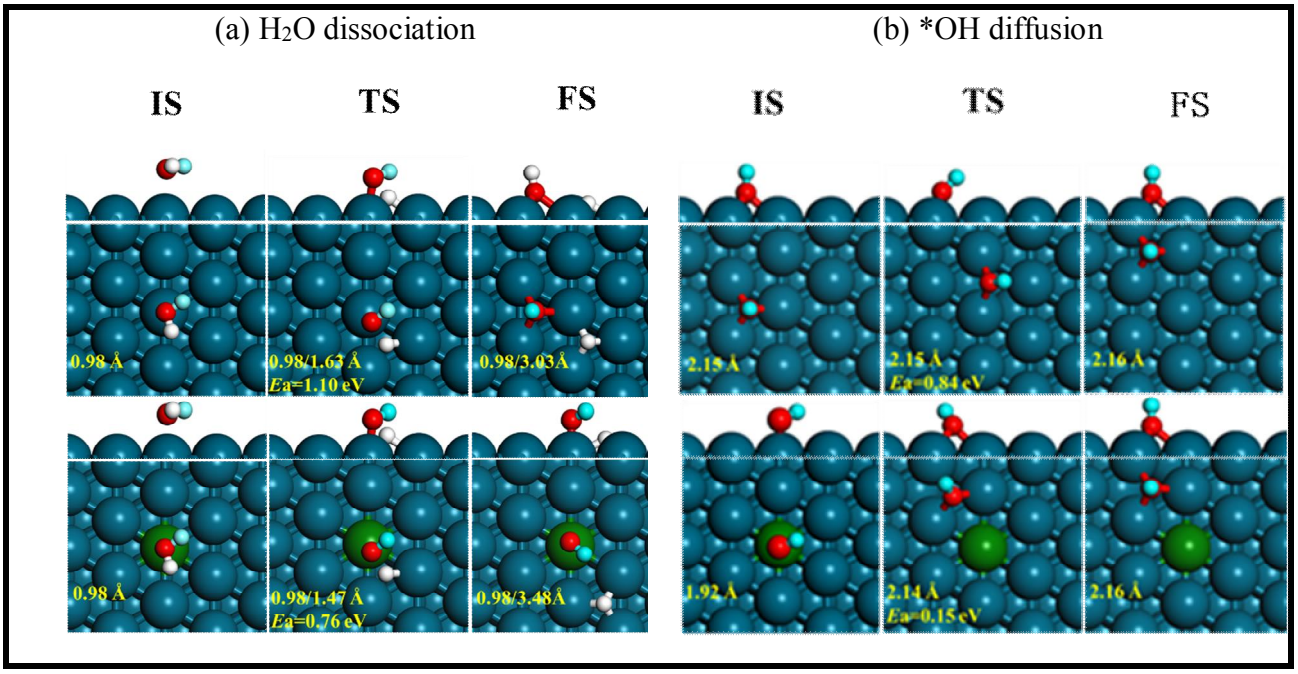

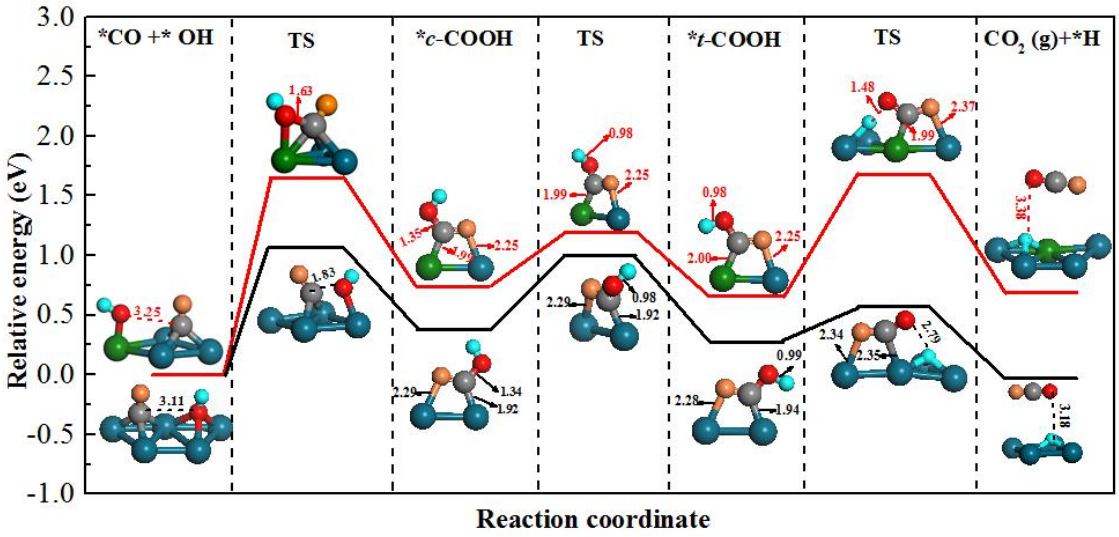

(c)

Figure 3.6 (a) Initial (IS), transition (TS), and final states (TS) of H_2O decomposion (O-H distances, H-O-H bond angle values and barrier energy are shown) (b) IS, TS, and TS of *OH diffusion (Ru-O and the average of Pd-O distances are shown) (c) CO oxidation on Ru@Pd (111) (black scatter) and Pd (111) (red line) surface. The H_1, H_2, O_1, O_2, C, Pd, Ru atoms were represented cyan, white, red, orange, grey, blue and green balls, respectively.

Figure 3.6(c) represents the process of *CO oxidation by *OH, the route is *CO+ *OH→ *cCOOH→*tCOOH→CO_2+ *H, noticeably, in which we discuss the *OH is from water not HCOOH. Nevertheless, the oxidation reaction has higher activation barriers on around Ru sites than pure Pd due to stronger adsorption energy, this is not consistent with the anticipation. Herein we have a conjecture is about *OH formation on single atom Ru sites after diffusion to other Pd sites to oxidize *CO, as Figure 3.6b, the micromolecule diffusion on metal surface is allowed, and the amounts of Pd sites far exceeds that of Ru sites [45-47], *OH from water activation is diffusion from Ru atom to Pd sites, the barrier is lower than reaction on Ru site. It is easier formation CO_2 on beside Pd sites, the results accord with the experiments for RuPd various alloy for FAO research [48].

3.4 Conclusions

In this study, using an ultralow RuPdPt/C surface to form a high-efficiency catalyst by irreversible adsorption method for DFAFC. The parts of Pd as a shell successfully covered Pt particles on carbon support, PdPt is the most potential catalysts compared with Pd/C and Pt/C due to its stable and electrocatalytic activity, RuPdPt/C enhance CO_2 direct pathway, meanwhile increasing CO tolerance via to reaction with OH of water dissociation on the Ru, OH shown the higher binding energy on Ru surface and CO the lower binding energy on Pd closed Ru by formic acid oxidation of CV image and DFT calculation. Therefore, RuPdPt/C catalyst exists superior performance for DFAFC.

References

[1] E. Antolini, J.R.C. Salgado, E.R. Gonzalez, The stability of Pt–M (M=first row transition metal) alloy catalysts and its effect on the activity in low temperature fuel cells, J. Power Sources 160 (2006) 957-968.

[2] X. Yu, P.G. Pickup, Recent advances in direct formic acid fuel cells (DFAFC), J. Power Sources, 182 (2008) 124-132.

[3] R.S. Amin, R.M. Abdel Hameed, K.M. El-Khatib, M. Elsayed Youssef, Electrocatalytic activity of nanostructured Ni and Pd–Ni on Vulcan XC-72R carbon black for methanol oxidation in alkaline medium, Int. J. Hydrog. Energy, 39 (2014) 2026-2041.

[4] W. Chen, S. Chen, Iridium-platinum alloy nanoparticles: Composition-dependent electrocatalytic activity for formic acid oxidation, J. Mater. Chem. A, 21 (2011) 9169-9178.

[5] X. Ji, K.T. Lee, R. Holden, L. Zhang, J. Zhang, G.A. Botton, M. Couillard, L.F. Nazar, Nanocrystalline intermetallics on mesoporous carbon for direct formic acid fuel cell anodes, Nat. Chem., 2 (2010) 286-293.

[6] U.B. Demirci, Direct liquid-feed fuel cells: Thermodynamic and environmental concerns, J. Power Sources 169 (2007) 239-246.

[7] C. Rice, Catalysts for direct formic acid fuel cells, J. Power Sources 115 (2003) 229-235.

[8] A.V. Tripković, K.D. Popović, R.M. Stevanović, R. Socha, A. Kowal, Activity of a PtBi alloy in the electrochemical oxidation of formic acid, Electrochem commun, 8 (2006) 1492-1498.

[9] Y. Suo, Synthesis of Highly Active Pt-Pd-Cu/C Catalysts for Formic Acid Oxidation, Int. J. Electrochem. Sci., 12 (2017) 3561-3575.

[10] C. Rice, S. Ha, R. Masel, A. Wieckowski, Catalysts for direct formic acid fuel cells, J. Power Sources 115 (2003) 229-235.

[11] C. Rice, S. Ha, R. Masel, P. Waszczuk, A. Wieckowski, T. Barnard, Direct formic acid fuel cells, J. Power Sources 111 (2002) 83-89.

[12] N.V. Rees, R.G. Compton, Sustainable energy: a review of formic acid electrochemical fuel cells, J. Solid State Electrochem., 15 (2011) 2095-2100.

[13] M.D. Maciá, E. Herrero, J.M. Feliu, Formic acid oxidation on Bi Pt(1 1 1) electrode in perchloric acid media. A kinetic study, J. Electroanal. Chem., 554-555 (2003) 25-34.

[14] Adolfo Ferre-Vilaplana, ‡ Juan Vıctor Perales-Rondon,§ Juan M. Feliu,§ and Enrique Herrero*,§, Understanding the Effect of the Adatoms in the Formic Acid Oxidation Mechanism on Pt(111) Electrodes, ACS Catal., (2014) 645-654.

[15] B. Fıçıcılar, A. Bayrakçeken, İ. Eroğlu, Effect of Pd loading in Pd-Pt bimetallic catalysts doped into hollow core mesoporous shell carbon on performance of proton exchange membrane fuel cells, J. Power Sources 193 (2009) 17-23.

[16] P. Hong, F. Luo, S. Liao, J. Zeng, Effects of Pt/C, Pd/C and PdPt/C anode catalysts on the performance and stability of air breathing direct formic acid fuel cells, Int. J. Hydrogen Energy, 36 (2011) 8518-8524.

[17] O.W.N. L. C. A. van den Oetelaar, S. Oerlemans, A. W. Denier van der Gon, and, H.H. Brongersma, Surface Segregation in Supported Pd-Pt Nanoclusters and Alloys, J. Phys. Chem. B (1998) 3445-3455.

[18] Antolini., Ermete., Palladium in fuel cell catalysis, Energy Environ. Sci., 2 (2009) 915-931.

[19] N.M. Marković, H.A. Gasteiger, P.N. Ross Jr, X. Jiang, I. Villegas, M.J. Weaver, Electrooxidation mechanisms of methanol and formic acid on Pt-Ru alloy surfaces, Electrochim. Acta, 40 (1995) 91-98.

[20] T.E.S. Marc T. M. Koper, and Rutger A. van Santen, <Periodic density functional study of CO and OH adsorption on PtRu alloy surfaces implications for CO tolerant fuel cell catalysts, J. Phys. Chem. B 686-692.

[21] A.O. Elnabawy, J.A. Herron, J. Scaranto, M. Mavrikakis, Structure Sensitivity of Formic Acid Electrooxidation on Transition Metal Surfaces: A First-Principles Study, J. Electrochem. Soc., 165 (2018) J3109-J3121.

[22] A. Deffernez, S. Hermans, M. Devillers, Bimetallic Bi–Pt, Ru–Pt and Ru–Pd and trimetallic catalysts for the selective oxidation of glyoxal into glyoxalic acid in aqueous phase, Appl. Catal. A, 282 (2005) 303-313.

[23] A.M. Ruppert, M. Jędrzejczyk, O. Sneka-Płatek, N. Keller, A.S. Dumon, C. Michel, P. Sautet, J. Grams, Ru catalysts for levulinic acid hydrogenation with formic acid as a hydrogen source, Green Chem., 18 (2016) 2014-2028.

[24] D. Wu, K. Kusada, H. Kitagawa, Recent progress in the structure control of Pd-Ru bimetallic nanomaterials, Sci Technol Adv Mater, 17 (2016) 583-596.

[25] J.K. Yoo, M. Choi, S. Yang, B. Shong, H.-S. Chung, Y. Sohn, C.K. Rhee, Formic acid electrooxidation activity of Pt and Pt/Au catalysts: Effects of surface physical properties and irreversible adsorption of Bi, Electrochim. Acta, 273 (2018) 307-317.

[26] M. Wei, C. Hsu, F. Liu, One-pot synthesis of mixed-phase Pd-Ru/C as efficient catalysts for electro-oxidation of formic acid, Int. J. Electrochem. Sci. 11 (2016) 2185-2196.

[27] J.F.b. G. Kresse av* Efficiency of ab-initio total energy calculations for metals and semiconductors using a plane-wave basis set, Comput. Mater. Sci. (1996) 15-50.

[28] G.K. *, Ab initio molecular dynamics for liquid metals, J Non Cryst Solids (1995).

[29] J.P. Perdew, Y. Wang, Accurate and simple analytic representation of the electron-gas correlation energy, Phys. Rev. B, 45 (1992) 13244-13249.

[30] J.P. Perdew, J.A. Chevary, S.H. Vosko, K.A. Jackson, M.R. Pederson, D.J. Singh, C. Fiolhais, Atoms, molecules, solids, and surfaces: Applications of the generalized gradient approximation for exchange and correlation, Phys. Rev. B, 46 (1992) 6671-6687.

[31] P.E. Blöchl, Projector augmented-wave method, Phys. Rev. B, 50 (1994) 17953-17979.

[32] W.A. H. Wang, XY. Liu, C. Heath Turner b, Oxygen reduction reaction on Pt(1 1 1), Pt(2 2 1), and Ni/Au1Pt3(2 2 1) surfaces: Probing scaling relationships of reaction energetics and interfacial composition, Chem. Eng. Sci., (2018) 239–250.

[33] R. Zhang, H. Liu, B. Wang, L. Ling, Insights into the Preference of CO2 Formation from HCOOH Decomposition on Pd Surface: A Theoretical Study, J. Phys. Chem. C, 116 (2012) 22266-22280.

[34] H.J. Monkhorst, J.D. Pack, Special points for Brillouin-zone integrations, Phys. Rev. B, 13 (1976) 5188-5192.

[35] J. Scaranto, M. Mavrikakis, HCOOH decomposition on Pt(111): A DFT study, Surf Sci, 648 (2016) 201-211.

[36] H.L. Skriver, N.M. Rosengaard, Surface energy and work function of elemental metals, Phys. Rev. B, 46 (1992) 7157-7168.

[37] D. Dang, H. Zou, Z.a. Xiong, S. Hou, T. Shu, H. Nan, X. Zeng, J. Zeng, S. Liao, High-Performance, Ultralow Platinum Membrane Electrode Assembly Fabricated by In Situ Deposition of a Pt Shell Layer on Carbon-Supported Pd Nanoparticles in the Catalyst Layer Using a Facile Pulse Electrodeposition Approach, ACS Catalysis, 5 (2015) 4318-4324.

[38] Feng Tao, 2 Michael E. Grass,1,2 Yawen Zhang,1,2,5 Derek R. Butcher,1,2 James R. Renzas,1,2 Zhi Liu,1,3 Jen Y. Chung,3 Bongjin S. Mun,3 Miquel Salmeron,1,4* Gabor A.

Somorjai1,2*, Reaction-Driven Restructuring of Rh-Pd and Pt-Pd Core-Shell Nanoparticles, Science (2008).

[39] https://en.wikipedia.org/wiki/X-ray_photoelectron_spectroscopy.

[40] Y.W. Lee, A.R. Ko, S.B. Han, H.S. Kim, K.W. Park, Synthesis of octahedral Pt-Pd alloy nanoparticles for improved catalytic activity and stability in methanol electrooxidation, Physical chemistry chemical physics: Phys. Chem. Chem. Phys., 13 (2011) 5569-5572.

[41] H. Liao, Z. Qiu, Q. Wan, Z. Wang, Y. Liu, N. Yang, Universal electrode interface for electrocatalytic oxidation of liquid fuels, ACS Appl. Mater. Interfaces, 6 (2014) 18055-18062.

[42] J.S. Yoo, H.T. Kim, H.-I. Joh, H. Kim, S.H. Moon, Preparation of a CO-tolerant PtRuxSny/C electrocatalyst with an optimal Ru/Sn ratio by selective Sn-deposition on the surfaces of Pt and Ru, Int. J. Hydrogen Energy, 36 (2011) 1930-1938.

[43] J.A. Herron, J. Scaranto, P. Ferrin, S. Li, M. Mavrikakis, Trends in Formic Acid Decomposition on Model Transition Metal Surfaces: A Density Functional Theory study, ACS Catal., 4 (2014) 4434-4445.

[44] T.E. Shubina., M.T.M. Koper., Quantum-chemical calculations of CO and OH interacting with bimetallic surfaces, Electrochim. Acta, (2002) 3621-3628.

[45] D.E. Sanders, A.E. DePristo, A non-unique relationship between potential energy surface barrier and dynamical diffusion barrier: fcc (111) metal surface, Surf. Sci. Lett., 264 (1992) L169-L176.

[46] D.S. Hsu, M.A. Hoffbauer, M. Lin, Dynamics of OH desorption from single crystal Pt (111) and polycrystalline Pt foil surfaces, Surf. Sci., 184 (1987) 25-56.

[47] J. Tully, M. Cardillo, Dynamics of molecular motion at single-crystal surfaces, Science, 223 (1984) 445-450.

[48] D. Wu, Z. Zheng, S. Gao, M. Cao, R. Cao, Mixed-phase PdRu bimetallic structures with high activity and stability for formic acid electrooxidation, Phys. Chem. Chem. Phys., 14 (2012) 8051-8057.

4 Bimetallic Pd-Based Surface Alloys Promote Electrochemical Oxidation of Formic Acid: Mechanism, Kinetics and Descriptor

4.1 Introduction

Formic acid (FA), known as a promising hydrogen storage carrier [1], can be also used directly as the feedstock for direct formic acid fuel cell (DFAFC), which has exhibited a number of advantages such as a high theoretical open circuit potential (1.48 V), a higher fuel concentration, a lower fuel crossover and low toxicity of FA at room temperature with respect to other types of fuel cells (e.g., PEMFC, DMFC) [2]. With FA produced from renewable resources [3], DFAFC can be regarded as the clean and green energy source. Over the years, electrochemical oxidation of formic acid (FAO) has been extensively researched that palladium and platinum as anode catalysts are the two prominent metals for catalyzing FAO, and comparatively, Pd is more beneficial than Pt owing to its high CO tolerance [4-6]. Additionally, the carbon materials are commonly used as support for improving the electro-conductibility and enhancing the electrochemical active surface area [7, 8]. It has been proposed both experimentally [6, 9-13] and theoretically [14-17] that FAO proceeds via either direct mechanism: HCOOH →*HCOO or *COOH (formate or carboxyl) → $CO_2 + 2H^+ + 2e^-$ or indirect mechanism: HCOOH →*COOH→*CO →$CO_2 + 2H^+ + 2e^-$, sensitively depending on the pH at the anode/electrolyte interface. As expected, the direct mechanism is highly preferred over the indirect mechanism as *CO poison can be minimized [18]. It was reported that the maximum current density of FAO was observed from low-index surfaces of crystal Pd and Pt, following the order of Pd(110) < Pd(111) < Pd(100) against Pt(111) < Pt(100) < Pt(110) [15, 19].

Bimetallic alloy of various forms (e.g., surface, near-surface, core-shell) have attracted much attention as advanced catalyst due to primarily the three unique effects, i.e., geometric, electronic and strain, introduced by the secondary metal [20-24]. Not surprisingly, Pd-based alloys and composites (PdM) such as M = Mo [25], Fe [26], Ru [27, 28], Co [29], Ni [30], Cu [31], Zn [32], Au [33], as well as CoP [34], Ni_2P [35, 36] have been employed as anode electrocatalysts for FAO demonstrating the improved activity/stability and the inhibition of CO poison. As a novel form of alloy, single-atom alloy (SAA) catalysts [37-39] were also fabricated and employed for catalyzing various types of reactions in heterogeneous catalysis. For example, single-atom Pt sites on AuPt alloy surface greatly promote FAO via the direct mechanism meanwhile inhibiting the *CO formation in indirect mechanism mainly through the ensemble effect, resulting in superior catalytic activity and selectivity [39]. Theoretically, bi-

metallic SAA models allow one to study the unique effects of alloyed single atom on catalytic properties by exploiting their structural uniformity and simplicity [38-41].

Herein, using density functional theory (DFT) calculations combined with microkinetic modeling, we systematically investigated FAO over bimetallic Pd-based single-atom surface alloys denoted as M@Pd(111) where M = Mo, Fe, Ru, Co, Ni, Cu, Zn, Ag, Au (total of 9 elements), considering the low-miller index (111) facets predominantly present on a fcc-metal nanoparticle catalyst surface. Our focus is on the role of alloyed single atoms of M in tuning the potential-determining step (PDS) of direct/indirect pathways (Figure 4.1) and thereafter deriving an effective catalytic descriptors for FAO activity.

4.2 Models and computational methods

4.2.1 Models

M@Pd(111) was modeled by a four-layer close-packed p(4×4) slab of Pd(111) with one Pd atom of the top layer replaced by one M atom, corresponding to 1/16ML of isolated M atoms. A vacuum region in the z-direction was set to 15 Å and the surface is periodic in the x- and y-direction. The size of chosen supercell is sufficiently large to avoid the interactions between the imaging cells. During the optimization, the adsorbates and the top two-layer metal atoms were allowed to relax while the bottom two layers were fixed at their bulk positions (Pd: 3.891 Å).

4.2.2 Computational methods

All DFT calculations were performed with the Vienna ab-initio simulation package (VASP) [42, 43] using the Perdew−Burke−Ernzerhof (PBE) exchange-correlation functional [44] of the generalized gradient approximation (GGA) and the projector augmented wave (PAW) pseudopotential [45, 46] for describing the core−valence interactions. The plane-wave cutoff energy was set to 400 eV. The Brillouin zone was sampled by a Γ-centered Monkhorst−Pack scheme [47] with 3 × 3 × 1 and 5 × 5 × 1 k-points grids for geometry optimization and electronic structure calculations, respectively. The conjugate gradient algorithm was used in ionic optimization. The convergence threshold was set to 10^{-4} eV for electronic relaxation and 0.02 eV/Å for forces. Fermi-smearing of k_{BT} = 0.1 eV was employed to speed up the convergence. All reported energies are extrapolated to k_{BT} = 0 eV. The transition states (TSs) were searched using the climbing image nudged elastic band (CI-NEB) method [48] combined with improved dimer method (IDM) [49, 50], in which all force components were relaxed below 0.02 eV/Å. Bader charge analysis was used to calculate the partial charge transfer [51]. Gibbs free energy of reaction for FAO elementary steps involving ($H^+ + e^-$) pair transfer was calculated using computational hydrogen electrode (CHE) model [15, 52], which has been successfully

employed for a variety of electrochemical systems including FAO [15, 53]. The limiting potential (UL) is obtained from the maximum free energy change (ΔGmax) among all elementary steps along the lowest-energy pathway by using the relation of U_L = -ΔGmax/e, where e is the unit charge. Theoretical overpotential is defined as $U_0 - U_L$, where U_0 is the equilibrium potential of FAO (i.e., -0.25 V).

4.2.3 Microkinetic Modeling

The microkinetics modeling was carried out using MKMCXX code developed by Filot et al [54]. The explicit solvation model containing four H_2O molecules adjacent to (111) surface [16, 17] was employed for locating TS of key elementary steps of FAO (Table 4.1) at electrochemical interface whose activation barriers (Ea) were used as input for microkinetic analysis. For the electrochemical steps, the rate constants k_i at T=298.15 K can be calculated as [55]:

$$k_i = A\exp\left(-\frac{\Delta G_i^{\#}(U_i^0)\text{-}e\beta_i(U+U_i^0)}{k_B T}\right) \tag{4-1}$$

Where $\Delta G_i^{\#}\left(U_i^0\right)$ is the activation free energy at the reversible potential U_i^0 of step i, A= k_{BT}/h = 6.21 × 10^{12} s^{-1}, which is the maximum value for the pre-exponential factor (A) of electrochemical steps, $\beta = 0.5$ is a symmetry factor was used for all elementary steps. kB is the Boltzmann constant, and h is the Planck constant. β is a symmetry factor, which is typically between 0.3 and 0.7. Here, $\beta = 0.5$ was used for all elementary reactions.

The reversible potential for step i is given by:

$$U_i^0 = -\frac{\Delta G_i^0}{e} \tag{4-2}$$

The equilibrium constant K_i at T=298.15 K can be calculated as:

$$K_i = \exp\left(-\frac{\Delta G_i}{k_B T}\right) \tag{4-3}$$

$$\Delta G_i = \Delta G_i^0 - eU \tag{4-4}$$

Where ΔG_i^0 is the reaction free energy at 0 V of step i, and U is the electrode potential versus RHE [56]. The rate constant for the backward electrochemical reaction is given by:

$$k_{-i} = K_i * k_i / \left[\mathrm{H}^+\right] \tag{4-5}$$

$$K_i = \exp\left(-\frac{\Delta G_i^0}{k_B T}\right) \tag{4-6}$$

Accordingly, the rate of key elementary step can be written as

$$r_2 = k_2\left[\mathrm{HCOOH}\right]\theta_* - k_{-2}\theta_{b\mathrm{H}_u\mathrm{COO}}\left[\mathrm{H}^+\right] \tag{4-7}$$

$$r_3 = k_3\theta_{b\mathrm{H}_u\mathrm{COO}} \tag{4-8}$$

$$r_4 = k_4\theta_* - k_{-4}\theta_{\mathrm{OH}}\left[\mathrm{H}^+\right] \tag{4-9}$$

Finally, the current density j for FAO directly on Ru@Pd(111) and Pd(111) is calculated as $j = j_{bH_uCOO} = 2Fk_3\theta_{bH_uCOO}$ [14]. θ_{mH_dCOO} is the coverage of *mH$_d$COO, F is Faraday's constant (96458C mol^{-1}). The 0.18%mol of H^+ (pH = 1) and 0.90% mol of HCOOH in H_2O solution were used to mimic those in experiment (0.1 M $HClO_4$ + 0.5 M HCOOH solution) [31].

Table 4.1 Summary of key elementary steps in reaction network[a].

	Reaction type	Process
	Direct pathway via formate	
R1	Absorption	$HCOOH + * \leftrightarrow *mH_uCOOH$
R2	Dehydrogenation (O-H)	$*mH_uCOOH \leftrightarrow *bH_uCOO + (H^+ + e^-)$
R3	Decoordination–Dehydrogenation(C-H)	$*bH_uCOO \leftrightarrow *mH_dCOO \rightarrow * + CO_2 + (H^+ + e^-)$
R4	Dissociation	$H_2O + * \leftrightarrow *OH + (H^+ + e^-)$
	Direct pathway via carboxyl	
R1	Absorption	$HCOOH + * \leftrightarrow *mH_dCOOH$
R2	Dehydrogenation(C-H)	$*mH_dCOOH \leftrightarrow *bCOOH_u + (H^+ + e^-)$
R3	Isomerization	$*bCOOH_u \leftrightarrow *bCOOH_d$
R4	Dehydrogenation(O-H)	$*bCOOH_d \leftrightarrow * + CO_2 + (H^+ + e^-)$
	Indirect pathway	
R3	Dehydroxylation	$*bCOOH_u + * \leftrightarrow *CO + *OH$
R4	Dehydration	$*bCOOH_u + (H^+ + e^-) \leftrightarrow *CO + H_2O$
R5	CO oxidation	$*CO + *OH \leftrightarrow 2* + CO_2 + (H^+ + e^-)$

[a]All adsorbed states (*) are selected from the most stable/reasonable configurations as displayed in Figure 4.5 and Figure 4.6. Both monodentate (*m*) and bidentate (*b*) adsorption modes of *HCOOH, *HCOO and *COOH were clearly marked with orientation of the H atom involving C-H and O-H bond forming/breaking. Specifically, Hu is for 'upward' and H_d is for 'downward' of H atom against the surface were specified.

4.2.4 Computational Details

The electrochemical formic acid oxidation (FAO) involves the coupled proton-electron pair ($H^+ + e^-$) transfer, where computational hydrogen electrode (CHE) model was used for the calculation of Gibbs free energy of reactions [1], defined as $\Delta G_n(U) = \Delta G_n (U=0) + neU$, where n is the number of ($H^+ + e^-$) pairs transferred in FAO and U is the electrode potential versus the reversible hydrogen electrode (RHE). At U=0 V, $\Delta G_n = \Delta E_n - T\Delta S + \Delta ZPE + \Delta E_{sol} + \Delta G_{pH}$, where ΔE_n is DFT-calculated reaction energy in vacuum, $T\Delta S$ is the entropy contributions to the reaction at T=298.15 K, ΔZPE is zero-point energy (ZPE) correction based on the calculated vibrational frequencies, ΔE_{sol} represents the correction of H_2O solvation effect at the water-solid interface, and ΔG_{pH} represents the correction of the free energy due to the variations in H+ concentration, defined as $GpH = kT \ln[H^+] = kT \ln 10 \, pH$, and the value of pH was set to 0 for strong acidic medium in this work and therefore, the calculated limiting potentials (U_L) were referenced to the RHE. Implicit model was used for treating H2O solvation effect, where ΔE_{sol} was accounted for depending on OH-containing species and their binding situations [2]: *R-OH bound to M directly/indirectly through hydroxyl is stabilized by approximately 0.5eV/0.25eV, respectively, and those containing no hydroxyl were stabilized approximately by 0.1eV. The free energy of gaseous molecules was calculated under the standard pressure of 1 bar. The limiting potential (U_L) is obtained from the maximum free energy change (ΔG_{max}) among all elementary steps along the lowest-energy pathway by using the relation of $U_L = -\Delta G_{max}/e$.

The entropies of the gaseous molecules were taken from the NIST Chemistry WebBook [3] and the zero-point energy (ZPE) was calculated according to:

$$E_{ZPE} = \sum_{i=1}^{3N} \frac{h\nu_i}{2} \qquad (4\text{-}10)$$

The entropy change for adsorbed intermediates was calculated within the hamoic approximation:

$$\Delta S_{ads}(0 \to T, P^0) = S_{vib} = \sum_{i=1}^{3N} \left[\frac{N_A h\nu_i}{T(e^{h\nu_i/k_BT} - 1)} - R\ln(1 - e^{-h\nu_i/k_BT}) \right] \qquad (4\text{-}11)$$

Where ν_i is DFT-calculated normal-mode frequency for species of 3N degree of freedom (N=number of atoms) adsorbed on Ru@Pt(211) SACs, N_A is the Avogadro's constant(6.022×10^{23} mol^{-1}), h is the Planck's constant (6.626×10^{-34}J s), and k_B is the Boltzmann constant (1.38×10^{-23} JK^{-1}), R is the ideal gas constant (8.314 J K^{-1} mol^{-1}), and T is the system temperature, and T=298.15K in this work.

The dissolution potentials (U_{dis}, in V) of M in M@Pd(111) at pH=0 were calculated as $U_{dis} = U_M^0 + [E_{M,bulk} - (E_{M@Pd(111)} - E_{Pd(111)})]/ne$, where U_M^0 is the standard dissolution potentials of M in the bulk form, $E_{M,bulk}$, $E_{M@Pd(111)}$ and $E_{Pd(111)}$ are the total energy of one M atom in the bulk, M-allyed Pd(111) and Pd(111) with M being dissolved out, respectively [4], and n is the coefficient for aqueous dissolution reaction: $M + nH^+ \leftrightarrow M^{n+} + n/2H_2$, where more positive values indicate more stable of M, and e is unit charge. The calculated binding energy of single M atom is also listed in Table 4.2.

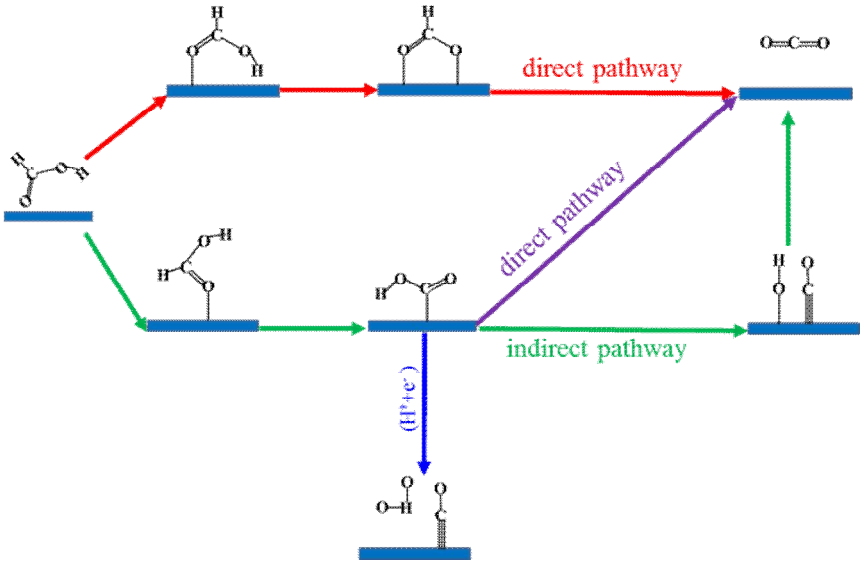

Figure 4.1 Proposed FAO reaction network on M@Pd(111).

4.3 Results and discussion

4.3.1 Stability and Electronic Structure of M@Pd(111)

To evaluate the stability of M@Pd(111) in strong acidic media, we calculated the dissolution potentials (U_{dis})[57] of M in M@Pd(111) at pH=0, as shown in Figure 4.2a and Table 4.2. It can be seen that all M@Pd(111) except M = Fe and Co have positive U_{dis} values, indicatives of surviving the medium of pH=0. With Pd(111) as a reference, all M@Pd(111) studied become less stable with the lowered and/or less positive U_{dis} values except Au and Ag, i.e., Co (-0.28 V) < Fe (-0.20 V) < Ni(0.03V)< Ru(0.24 V) < Mo (0.28 V) < Zn (0.48 V) < Cu(0.93 V)< Pd (1.42 V) < Ag (1.81 V) < Au (1.98 V), but are still more stable than their bulk counterparts of M based on $U_{dis} > U_{M0}$. The DFT-calculated binding energy (BE) also suggests that M@Pd(111) are highly stable with respect to Pd(111).

Regarding M-Pd bonding situation, there exists the substantial electron charge transfer from M atom to host Pd atoms (equivalently, the oxidation state of M^{+}), i.e., $Mo^{1.00+} > Fe^{0.49+} > Zn^{0.48+} > Co^{0.33+} > Ru^{0.28+} > Cu^{0.23+} = Ni^{0.23+} > Ag^{0.11+}$ except $Au^{0.17-}$, an indicative of the formation of polarized heteroatom Pd-M bonds, which enable the tuning of the electronic structure of local active sites adjacent to M atom. The partial positive charge of doped atom could have beneficial effect on the modified surface for promoting FAO [58]. We further employed CO and OH (which are relevant to FAO) as probe species to evaluate the effect of alloyed M on electronic structure of M@Pd(111). As can be seen from Figure 4.2b, the calculated binding energy of adsorbed *CO and *OH increases proportionally with the upshifting of d-band center of surface atoms where the adsorbates are bound, showing alloyed M single atom can not only act as active site but also affect the reactivity of nearest-neighboring Pd atoms via the ligand effect (charge transfer). More importantly, binding strength of *CO and *OH can be used as an indicator for carbophilicity and oxyphilicity of alloyed M [59], from which an effective descriptor may be derived for FAO catalyst design.

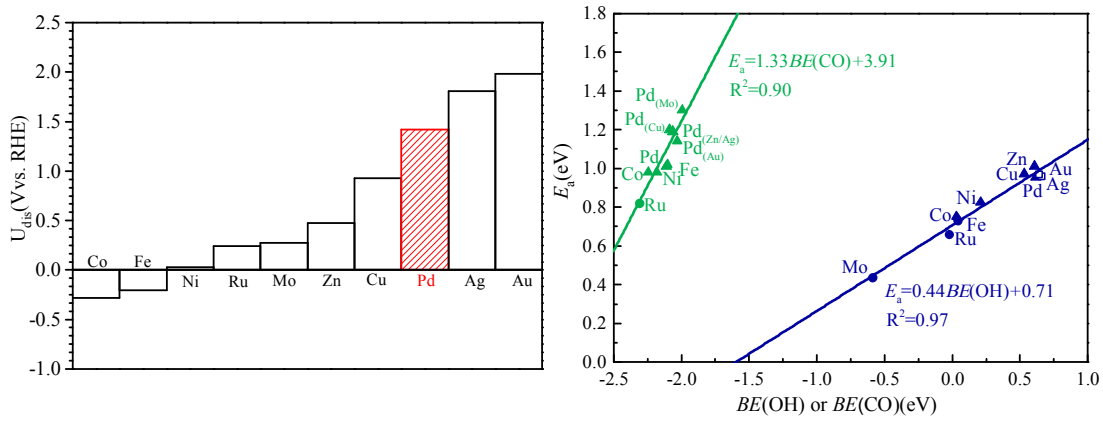

(a) (b)

Figure 4.2 (a) DFT-calculated dissolution potentials (U_{dis}) of M in M@Pd(111). (b) Linear correlation between *OH/*CO binding energy (BE) and *d*-band center (ε_d) of active sites, where *OH and *CO are favorably adsorbed. $Pd_{(M)}$ represents M's the nearest-neighboring Pd site where adsorbed *CO prefers (Figure 4.11, 4.12). •: M-top site for *OH and *CO. □: Pd-M bridge site for *OH. ▲: 3-fold hollow site of Pd-M-Pd for *OH and *CO.

Table 4.2 Standard dissolution potential (U_{M0}) of bulk metals, DFT-calculated binding energy (BE)*, dissolution potential (U_{dis}) of M in M@Pd(111), where $M + nH^+ \rightarrow M^{n+} + n/2H_2$ at pH=0.

Metal	n	U_{M0}(V vs. RHE)	U_{dis}(V vs. RHE)	BE(eV)
Mo	3	-0.20	0.28	-7.71
Fe	2	-0.45	-0.20	-4.76
Ru	2	0.46	0.24	-8.71
Co	2	-0.28	-0.28	-7.07
Ni	2	-0.26	0.03	-5.44
Cu	2	0.34	0.93	-4.85
Zn	2	-0.76	0.48	-3.42
Ag	1	0.80	1.81	-3.92
Au	3	1.50	1.98	-4.64
Pd	2	0.95	1.42	-4.69

* $BE = E_{M@Pd(111)} - E_{Pd(111)} - EM$, where $E_{M@Pd(111)}$, $E_{Pd(111)}$ and E_M are total energy of M-allyed Pd(111), Pd(111) with M being dissolved out, and isolated single atom, respectively.

4.3.2 Mechanistic aspect of FAO on Ru@Pd(111).

The experimentally synthesized PdRu nanoparticle alloys have demonstrated enhanced activity and stability compared to commercial monometallic Pd/C catalyst towards FAO[27, 28]. Accordingly, we chose Ru@Pd(111) single-atom surface alloy as model catalyst to explore both direct and indirect mechanism of FAO (Figure 4.1 and Table 4.1). As shown in Figure 4.3, there exists the subtle discrepancy of adsorbed configuration of *HCOOH in that *mH$_u$COOH (BE=-0.71eV) has carbonyl H atom (cyan ball) pointing *upward(u)* and *mH$_d$COOH (BE=-0.47eV) has carbonyl H atom (cyan ball) pointing *downward(d)* against the catalyst surface, which have important implication of how dehydrogenation of *HCOOH is initiated. The adsorbed *mH$_u$COOH favors the formation of formate *HCOO while the adsorbed *mH$_d$COOH favors the formation of carboxyl *COOH, leading to either direct pathway (HCOOH → *HCOO or *COOH → $CO_2 + 2H^+ + 2e^-$) or indirect pathway (HCOOH → *COOH→*CO →$CO_2 + 2H^+ + 2e^-$) in FAO. Additionally, *bHCOOH (BE=-0.32eV) with *bidentate (b)* adsorption mode was identified for Ru@Pd(111) and other M@Pd(111) with moderate binding strength (Figure 4.4), but not on pure Pd(111), Cu@Pd(111), Zn@Pd(111), Ag@Pd(111) and Au@Pd(111) with nearly no binding strength, same as on low-miller index Au facets[60]. Nonetheless, *bHCOOH was not chosen as the starting point for the subsequent reactions due to its weaker binding.

It is generally accepted that the cleavage of O-H or C-H bond of HCOOH is the first step for FAO on metal surfaces [61-64]. As can be seen from Figure 4.5 and Figure 4.6, *mH$_u$COOH configuration (BE=-0.88eV) is highly preferred for facilitating O-H bond scission to form *HCOO without encountering geometric frustration, while *mH$_d$COOH (BE=-0.63eV) is highly preferred for facilitating C-H bond cleavage to form *COOH. For direct mechanism (Figure 4.5), the PDS is identified as the decoordination of adsorbed state from bidentate to monodentate *HCOO (*bH$_u$COO→ *mH$_d$COO) with a free energy barrier of 0.73eV (TS2) on Ru@Pd(111) against 0.95eV (TS2) on Pd(111), followed by the facile carbonyl-H abstraction toward the final product of $CO_2 + (H^+ + e^-)$. Here, the bidentate-bonded *HCOO species has been experimentally validated [12-14]. The alternative route in direct mechanism is via *mH$_d$COOH → *bCOOH$_u$ followed by carboxyl O-H bond cleavage to form CO_2, however, encounters a much higher barrier (Ea=1.12eV, TS6) on Ru@Pd(111), which makes carboxyl route less competitive with formate route in direct mechanism. The previous experimental [10, 11] studies also reported that FAO on Pd-based catalyst proceed mainly via direct mechanism. Note also that *bH$_u$COO → *mH$_d$COO was identified as the rate-liming step in previous DFT studies on HCOOH decomposition on Pd(111) [63-66] and FAO on Pt(111)[16]. Moreover, our calculated activation barrier on Pd(111) agrees well with those (0.90eV and 0.93eV) previously reported[63, 64].

On the other hand, FAO is also likely to proceed via indirect mechanism on Ru@Pd(111) because the binding strength of *mH$_d$COOH is competitive with *mH$_u$COOH for active sites as mentioned earlier. However, FAO encounters much higher activation barriers in indirect mechanism (*CO) via either dehydroxylation (0.83eV, TS7) or dehydration (1.15eV, TS9) as compared to direct mechanism via formate (0.73eV, Figure 4.6). On Pd(111), FAO has an activation barrier of 1.01eV(TS7) in indirect mechanism via dehydroxylation, consistent with that (1.02eV) reported in previous study[67]. Here, the effect of alloyed Ru on *CO binding is two-fold: (i) enhancing the binding strength of *CO adsorbed at top site of Ru with BE=-2.31eV; (ii) reducing the binding strength of *CO adsorbed at the nearest-neighboring fcc site of Pd with BE=-2.03 eV (Table 4.3) with respect to that (BE=-2.10eV) on Pd(111). Given that, Ru sites are likely to be poisoned by strongly-adsorbed *CO and accordingly, the nearest-neighboring top site of Pd can act as the active site for FAO. However, our calculated results using explicit solvation model of H_2O demonstrate that H_2O-assisted HCOOH adsorption at electrochemical interface of H_2O/Ru@Pd(111) and H_2O/Pd(111) results in facile release of carboxyl H forming adsorbed *bH$_u$COO (Section 4.3.4), which suppress HCOOH →*COOH→*CO route, consistent with the experimental observations that Pd-based electrodes are superior to Pt-based ones due to their resistance to CO poison[9-11].

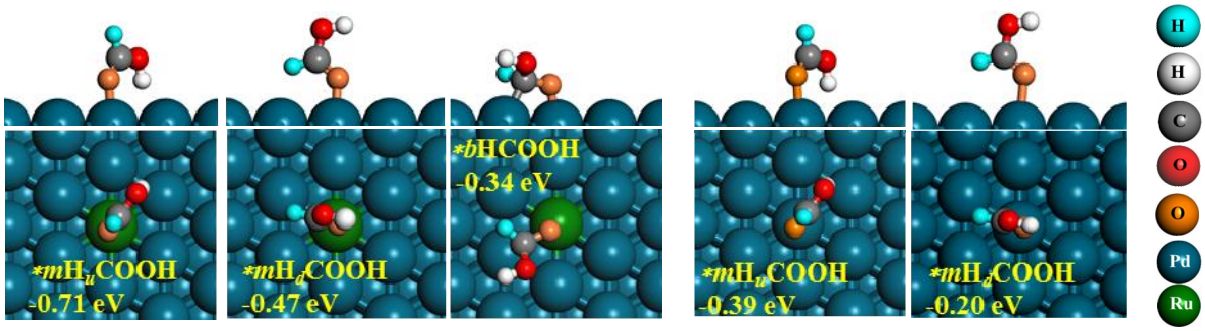

(a) (b)

Figure 4.3 Optimized structures of *HCOOH adsorbed on (a) Ru@Pd(111) and (b) Pd(111). Binding energy (BE, in eV) of *HCOOH were marked.

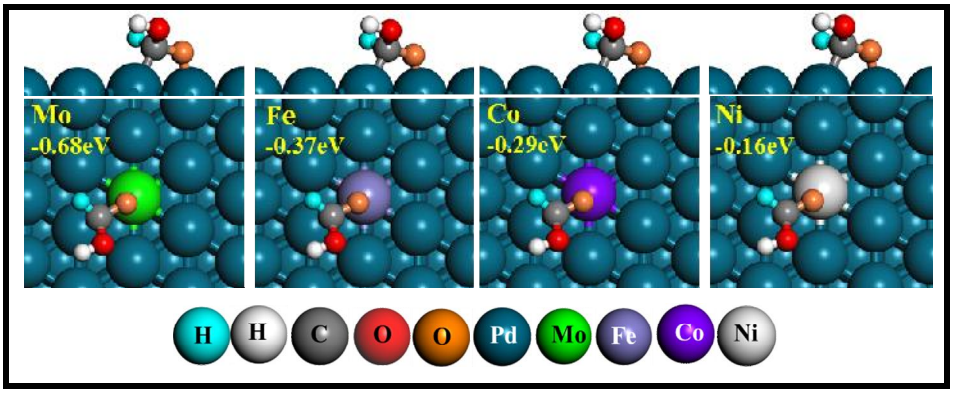

Figure 4.4 Optimized structures of *bHCOOH adsorbed on M@Pd(111). Binding energy (BE, in eV) of *bHCOOH were marked.

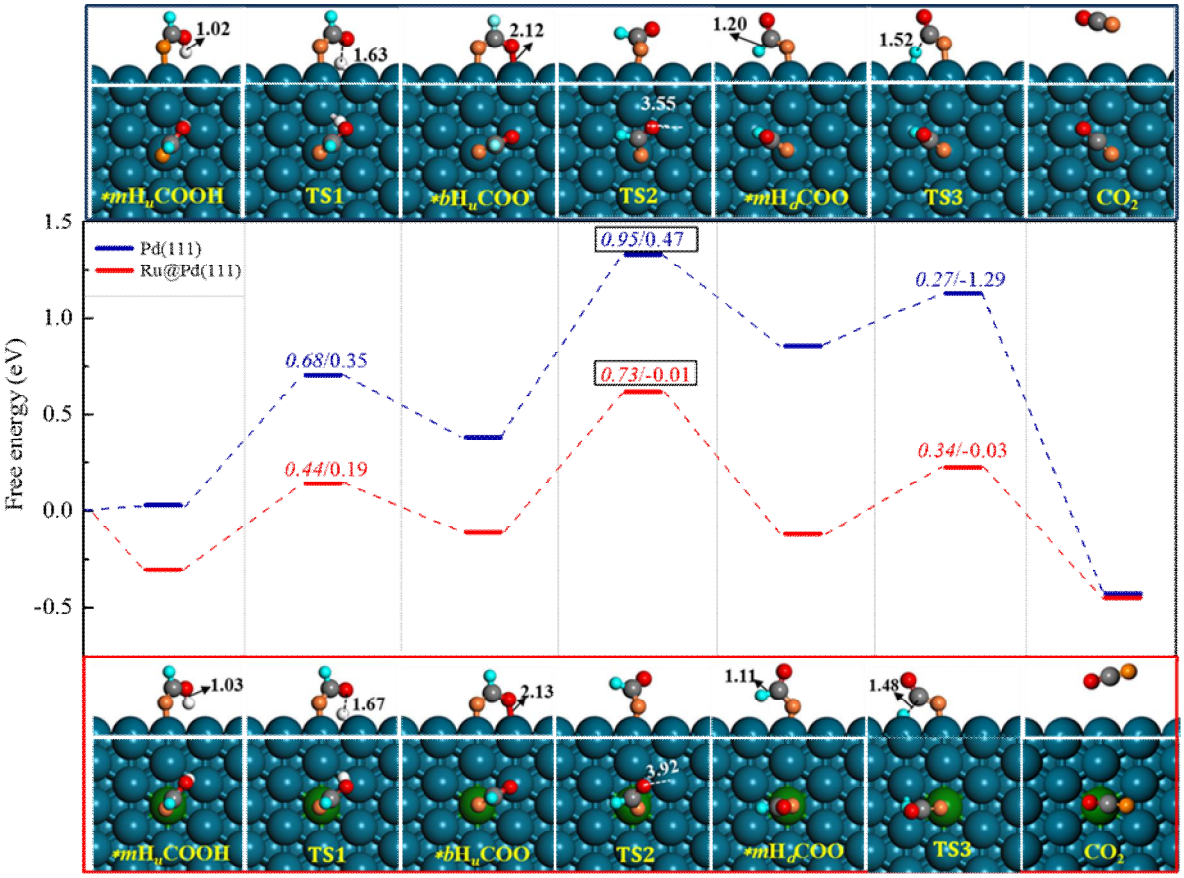

Figure 4.5 Free energy profiles for FAO toward CO_2 via direct mechanism (*HCOO) on Ru@Pd(111) and Pd(111), along with the DFT-optimized structures. Bond lengths (in Å), activation energy (italic font, in eV) and reaction energy (regular font, in eV) are displayed. Black rectangular: PDS.

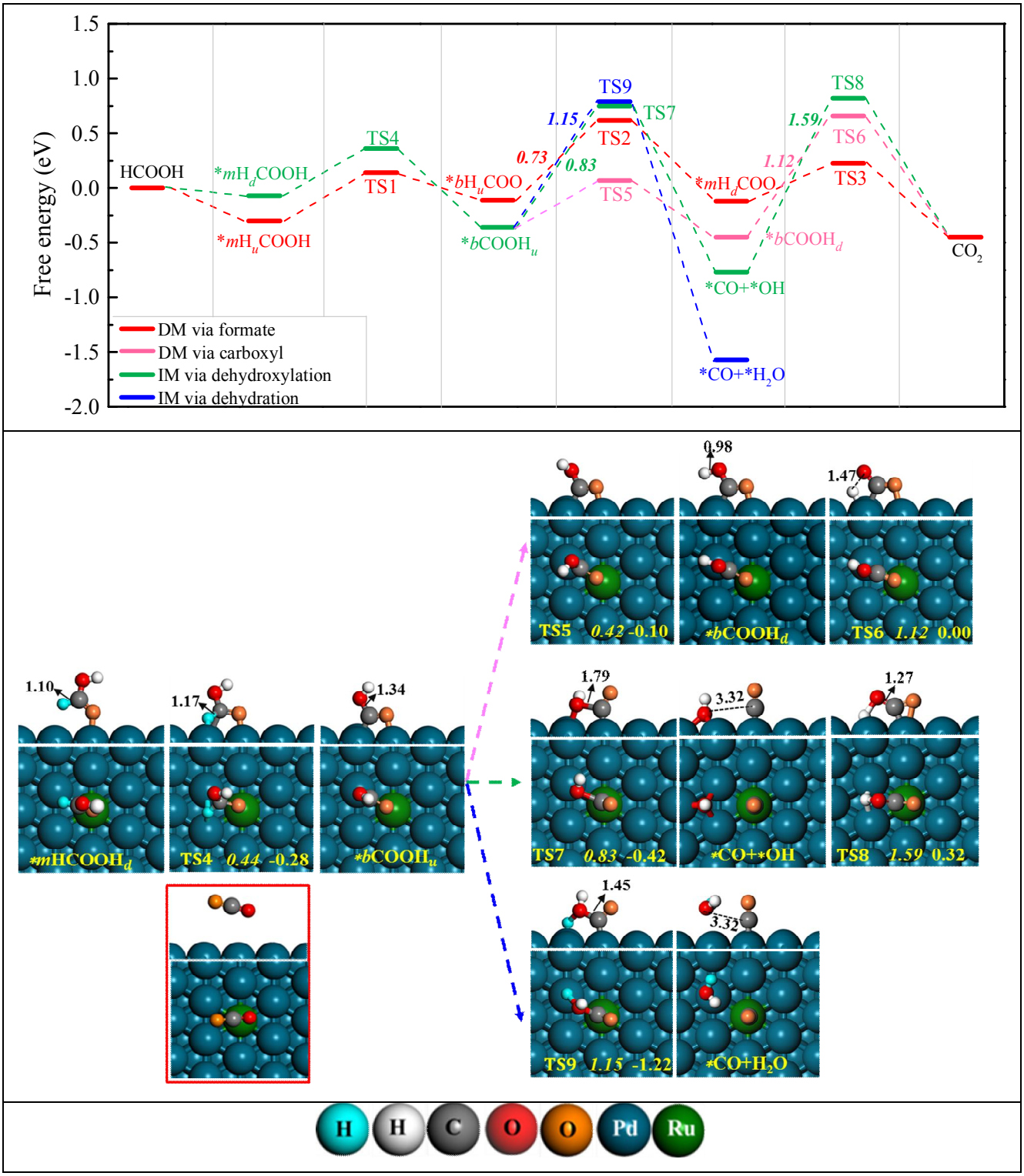

Figure 4.6 Free energy profiles for FAO toward CO_2 via direct mechanism (DM, *HCOO/*COOH), indirect mechanism (IM, *CO) on Ru@Pd(111) and Pd(111), along with the DFT-optimized structures. Bond lengths (in Å), activation energy (italic font, in eV) and reaction energy (regular font, in eV) are displayed.

Table 4.3 Binding energy (BE, in eV) of *mHuCOOH, *mHdCOOH, *bHCOOH, *CO2, *CO and *H2O with most stable configuration on Ru@Pd(111) and Pd(111) calculated using their gas-phase as reference.

Catalyst	*mH$_u$COOH	*mH$_d$COOH	*bHCOOH	*CO_2	*CO[a]	*H_2O
Pd(111)	-0.39	-0.20	—	-0.04	-2.10	-0.26
Ru@Pd(111)	-0.71	-0.47	-0.32	-0.03	-2.31/-2.03[b]	-0.55

[a]The most stable configuration of CO adsorption is 3-fold hollow site on Pd(111) and Ru-top site on Ru@Pd(111).

[b]Adsorbed at 3-fold hollow site of the nearest-neighboring Pd.

Table 4.4 Binding energies (BE)[a] of the adsorbed species with the most stable configuration on Ru@Pd(111) and Pd(111) calculated using CO_2, H_2 and H_2O as references.

Metals	*mH$_u$COOH	*mH$_d$COOH	* bHCOOH	*bH$_u$COO	*mH$_d$COO	*bCOOH$_d$	*bCOOH$_u$	*CO[b]	*CO_2
Pd(111)	-0.57	-0.36	—	-0.13	0.56	-0.33	-0.21	-1.39	-0.03
Ru@Pd(111)	-0.88	-0.63	-0.50	-0.61	-0.06	-0.62	-0.54	-1.60/-1.32c	-0.04

[a]The Binding energies (BE) is defined as $E[CH_xO_y] = E[CO_2] + [(4+x-2y)/2]*E[H_2] - (2-y)*E[H_2O]$, calculated using gas-phase CO_2, H_2 and H_2O energy as the reference.

[b]The most stable configuration of CO adsorption is 3-fold hollow site on Pd(111) and Ru-top site on Ru@Pd(111).

[c]Adsorbed at 3-fold hollow site of the nearest-neighboring Pd.

Table 4.5 Zero-point energy (ZPE, in eV) and entropy corrections (TS, in eV) at T = 298.15 K for gaseous molecules.

Molecules	ZPE	TS
H_2	0.30	0.40
H_2O	0.64	0.58
HCOOH	0.91	0.77
CO_2	0.31	0.66

Table 4.6 Zero-point energy (ZPE, in eV) and entropy corrections (TS, in eV) at T = 298.15 K for adsorbates.

Adsorbate	Pd(111)		Ru@Pd(111)	
	ZPE	TS	ZPE	TS
*mH$_u$COOH	0.88	0.09	0.88	0.09
*mH$_d$COOH	0.90	0.13	0.91	0.18
*bCOOH$_d$	0.22	0.13	0.60	0.17
*bCOOH$_u$	0.59	0.07	0.59	0.18
*bH$_u$COO	0.60	0.07	0.60	0.07
*mH$_d$COO	0.50	0.10	0.09	0.02
*CO	0.18	0.16	0.20	0.09
*CO+*OH	0.67	0.24	0.52	0.13

4.3.3 Descriptor for FAO and catalyst screening

From above, Ru@Pd(111) has demonstrated the enhanced activity for FAO as compared to Pd(111). With $*bH_uCOO \rightarrow *mH_dCOO$ being identified as PDS, we explored the underlying origin of beneficial effect of alloyed Ru on lowering the activation barrier. Figure 4.7 displays isosurface of charge-density difference ($\Delta\rho$) for adsorbed $*bH_uCOO$, showing the bond strength of $*bH_uCOO$ with bidentate-adsorption mode is unequal in that Ru-O bond is stronger than Pd-O bond visualized by the larger lobe of charge accumulation of Ru-O bond and of charge depletion around Ru. Such unsymmetrical binding strength has the natural advantage of promoting the decoordination from $*bH_uCOO$ to $*mH_dCOO$, where the oxyphilic Ru atom facilitates bidentate-to-monodentate transformation. The same behaviors are found for Mo@Pd(111) and Fe@Pd(111) (Figure 4.7). Remarkably, the calculated activation barriers of TS2 ($*bH_uCOO \rightarrow *mH_dCOO$) reduce proportionally with the enhanced oxyphilicity of alloyed M, i.e., Mo>Fe≈Co≈Ru>Zn≈Cu≈Ni≈Ag>Au≈Pd [68], using *OH binding strength as an indicator[40, 69] (Figure 4.8a). That is, the alloyed M with moderate-to-strong oxyphilicity would facilitate the decoordination of bidentate HCOO on M@Pd(111). Likewise, the calculated activation barriers of TS7 ($*bCOOH_u + * \rightarrow *CO+*OH$) reduce proportionally with the carbophilicity of alloyed M using *CO binding strength as an indicator [59] (Figure 4.8a), where *CO is bound with M and *OH is bound with Pd. Note here that both *CO and *OH are the key intermediates involved in the reaction mechanism of FAO. Assuming the PDS for FAO on M@Pd(111) is unchanged, one can see that the direct mechanism via formate intermediate is favored in the order of M(Ea)=Mo(0.44eV)>Fe(0.66eV)>Ru(0.73eV)>Co(0.75eV)>Ni(0.82eV)>Pd(0.95eV)>Au(0.96eV)>Cu(0.97eV)=Ag(0.97eV)>Zn(1.01eV), while the indirect mechanism via CO intermediate is disfavored in the order of M(Ea)=Mo(1.40eV)>Cu(1.22eV)>Zn(1.20eV) >Ag(1.19eV) >Au(1.14eV)>Pd(1.01eV) >Fe(1.00eV) >Co(0.98eV)=Ni(0.98eV)>Ru(0.83eV) (Figure 4.8b). Specifically, we would predict M@Pd(111) where M = Mo, Fe, Ru, Co, Ni as the promising Pd-based bimetallic catalysts for promoting FAO via the direct mechanism, among which Mo@Pd(111) could be the best among M studied due to the additional function of inhibiting *CO formation. Indeed, Pd-based alloys (e.g., M = Mo, Fe, Ru, Co, Ni) [25-30] have been experimentally verified to be efficient FAO catalysts with high activity and stability. Here, it is worthy noting that the measured FAO performance catalyzed by PdMo alloy is controversial in experiment, from which both enhanced [25] and decreased [70] FAO performance were observed relative to Pd. We speculate that the oxidation state and the dispersion of Mo within synthesized PdMo could be the key factors that affect the performance of the catalyst, e.g., increasing the proportion of Mo (accordingly varying the oxidation state and the dispersion of Mo) further lowered the current

density of PdMo [70]. By contrast, our predictions are based on single-atom M@Pd(111) surface alloy, where the oxidation state and the dispersion of M are well-defined, e.g., 1/16ML of $Mo^{1.00+}$ for Mo@Pd(111) and 1/16ML of $Ru^{0.28+}$ for Ru@Pd(111), but during the electrooxidation for FAO they can be increased and altered, even leading to the formation of metal oxides for M=Mo and Ru [71, 72]. Accordingly, our theoretical predictions serve only as a baseline Furthermore, the scaling relations can be identified between *HCOO/*COOH and *CO/*OH binding energies on single-atom M@Pd(111) surface alloys (Figure 4.13), provided that the appropriate x for *CO and y for *OH are employed, i.e., (x=0, y=1) for $*b\mathrm{H_uCOO}$, (x=0, y=1) for $*m\mathrm{H}_d\mathrm{COO}$, and (x=1, y=1) for $*b\mathrm{H_uCOO}$, same as those on transition metal surfaces [73] except the equal weight of *CO/*OH for $*b\mathrm{COOH}_u$ due to its binding configuration (Figure 11). Such a difference renders M of M@Pd(111) (except M = Ru) being capable of inhibiting *COOH→*CO (Figure 4.12) as compared to monometallic metal surfaces.

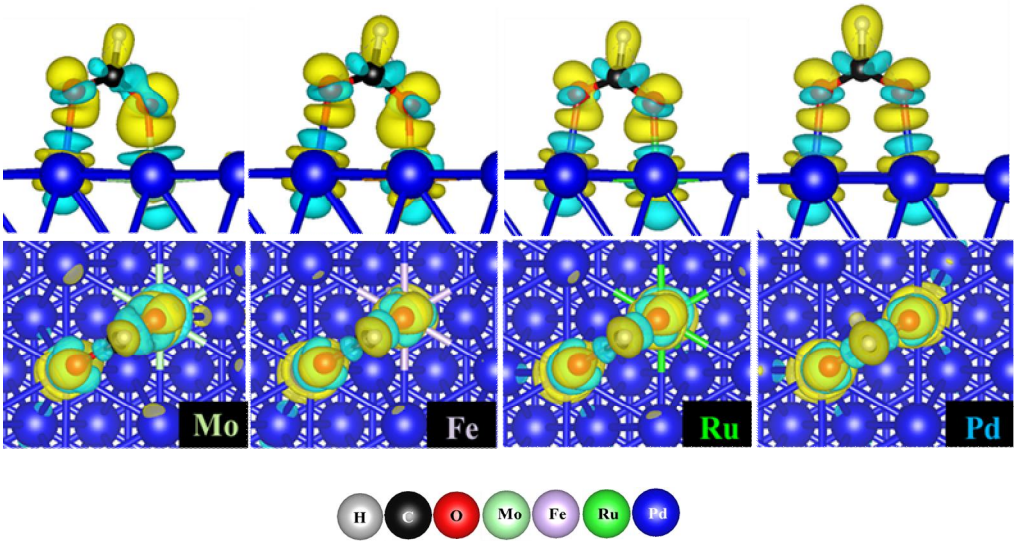

Figure 4.7 Isosurface of charge-density difference (Δρ) for adsorbed *bH$_u$COO on Mo@Pd(111), Fe@Pd(111), Ru@Pd(111) and Pd(111), respectively. Both top and side views are displayed. Yellow: charge accumulation; Cyan: charge depletion. Isosurface level=0.004 e/Bohr^3. $\Delta\rho = \rho_{(\text{slab+ads})} - \rho_{(\text{slab})} - \rho_{(\text{ads})}$.

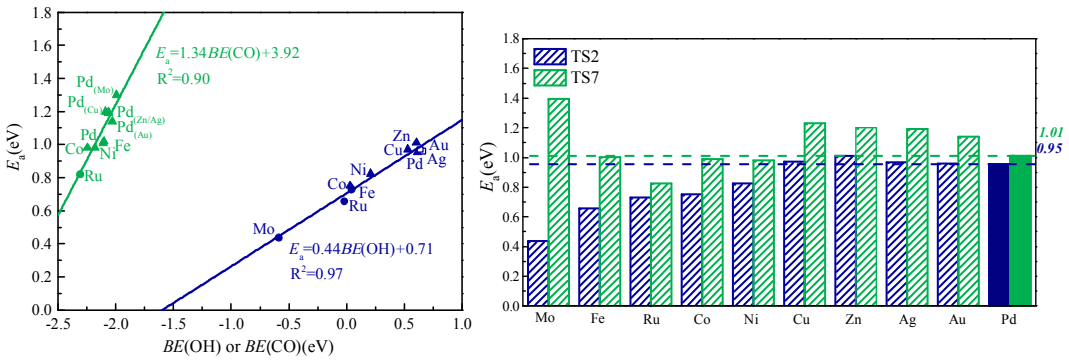

(a) (b)

Figure 4.8 (a) Correlation of activation energy (E$_a$) as a function of *OH/CO binding energy (BE). Blue line: *bH$_u$COO ↔ *mH$_d$COO for TS2 as in Figure S5; Green line: *bCOOH$_u$ + * ↔ *CO+*OH for TS7. (b) Comparison of activation energy (E$_a$) on M@Pd(111) and Pd(111).

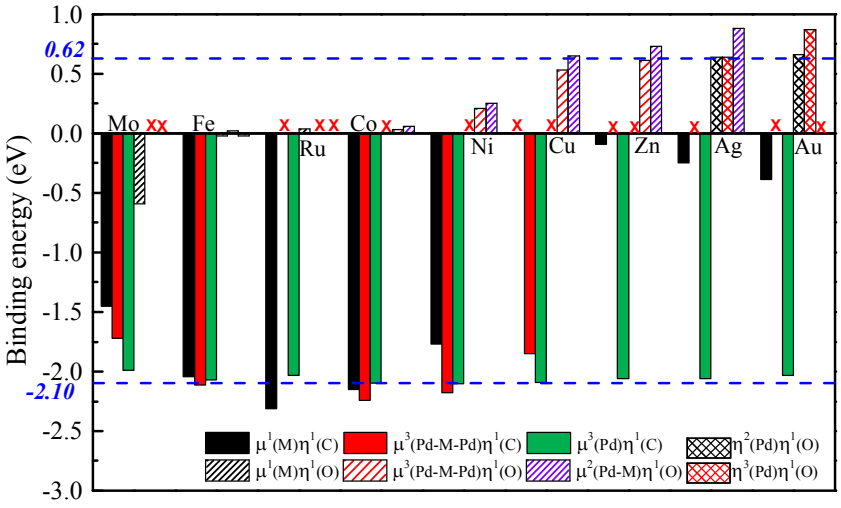

Figure 4.9 The binding energy of *CO and *OH adsorbed on M@Pd (111). Solid color: *CO; Striped color: *OH; Horizontal dashed lines: *CO and *OH adsorbed on Pd(111).

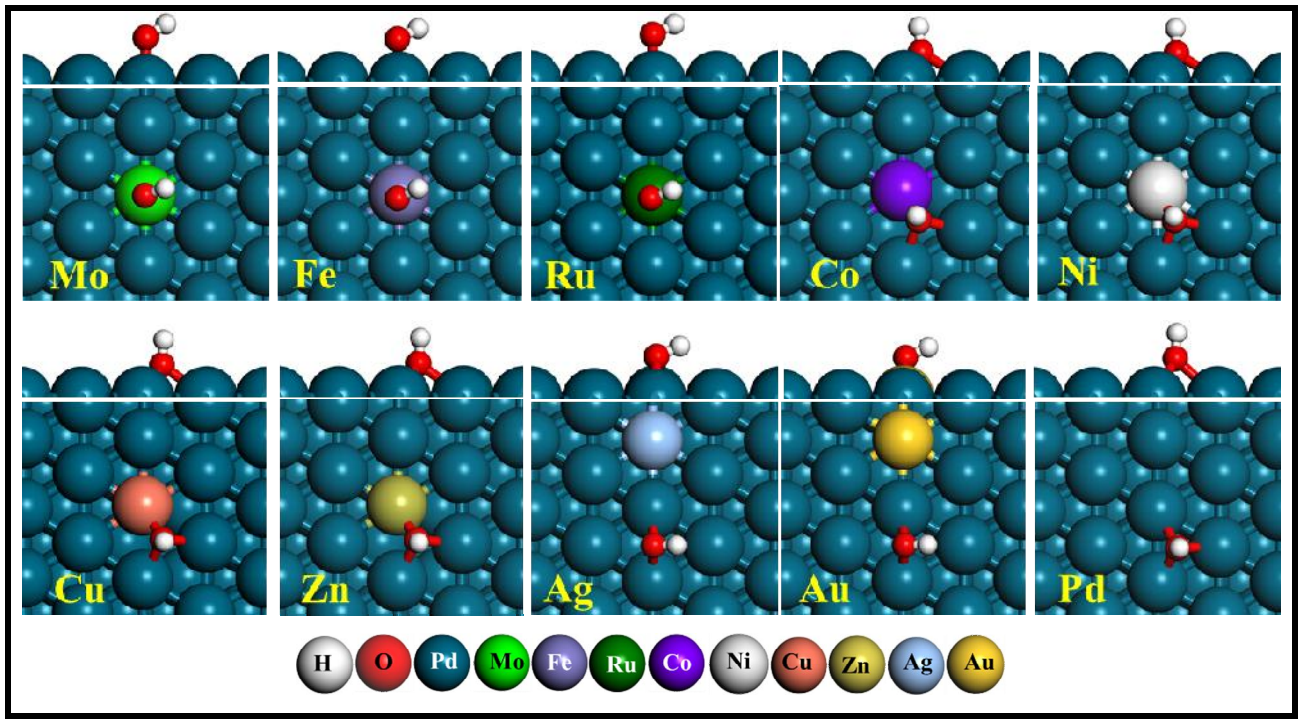

Figure 4.10 Optimized initial state *OH configurations on M@Pd(111).

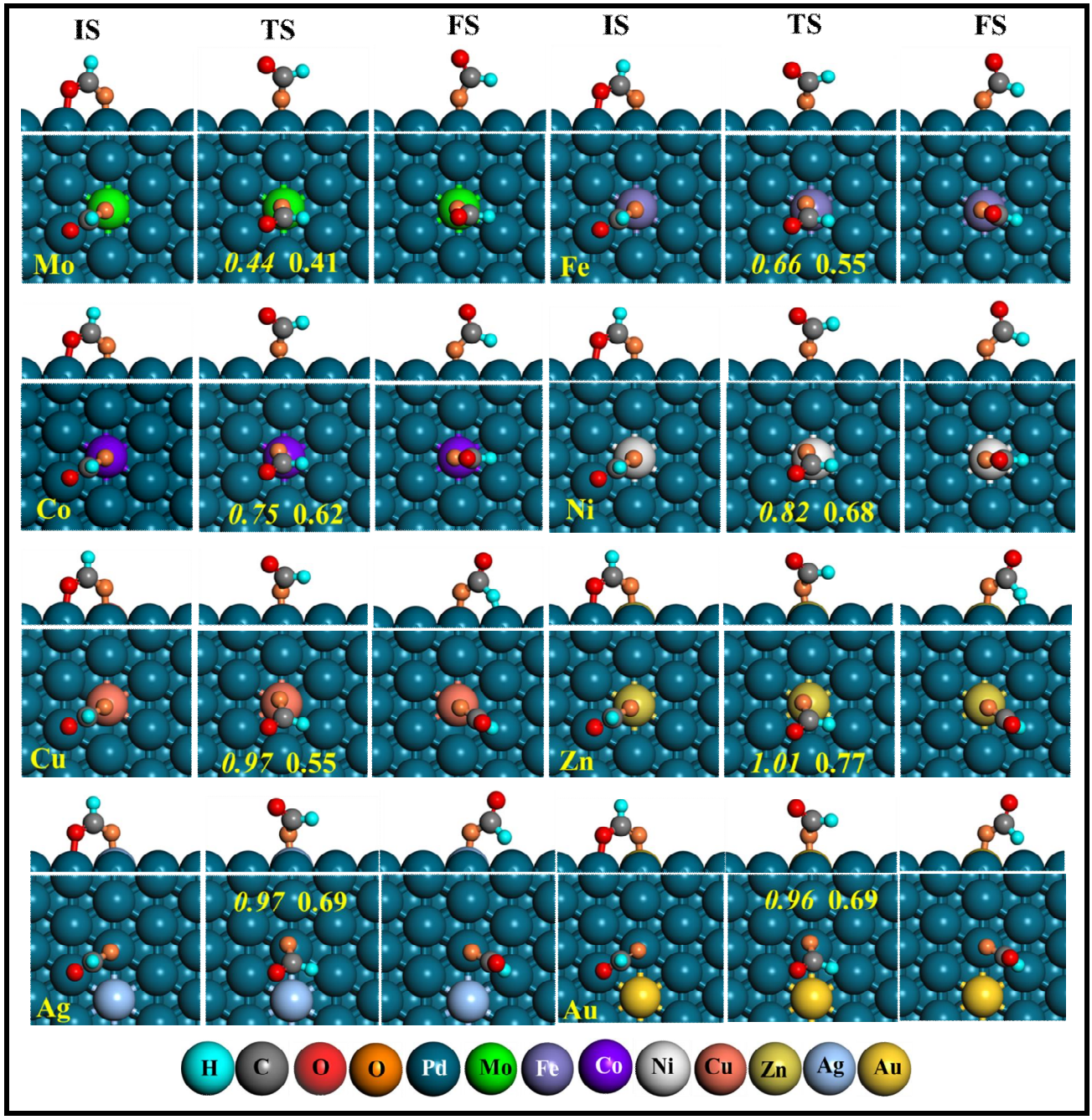

Figure 4.11 Optimized initial state (IS), transition state (TS) and final state (FS) configurations of R_3 (*bH$_u$COO ↔ *mH$_d$COO) along direct pathway, activation energy (italic font, in eV) and reaction energy (regular font, in eV) are displayed.

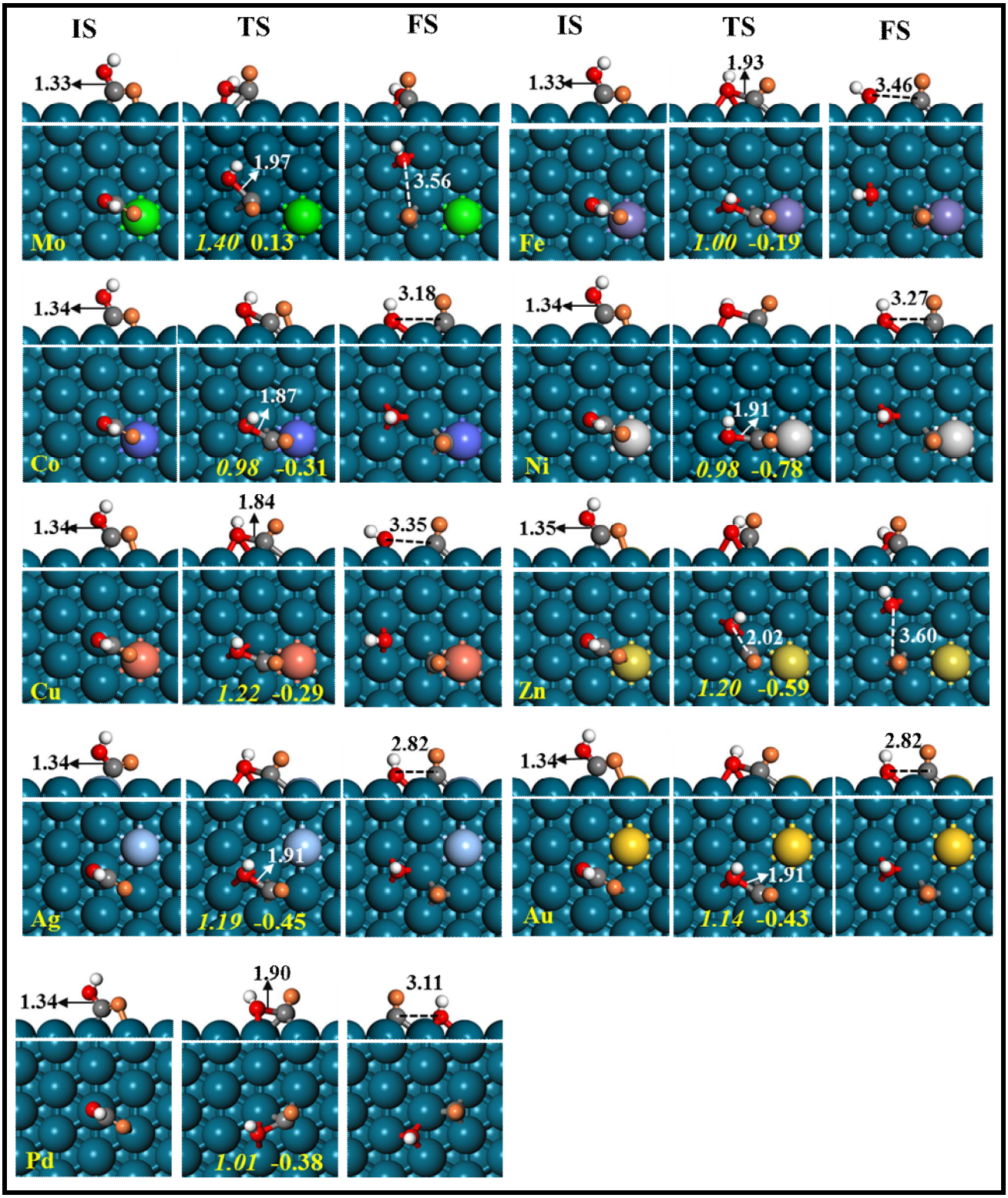

Figure 4.12 Optimized initial state (IS), transition state (TS) and final state (FS) configurations of R_3 (*bCOOH$_u$ + * ↔ *CO+*OH) along direct pathway, activation energy (italic font, in eV) and reaction energy (regular font, in eV) are displayed.

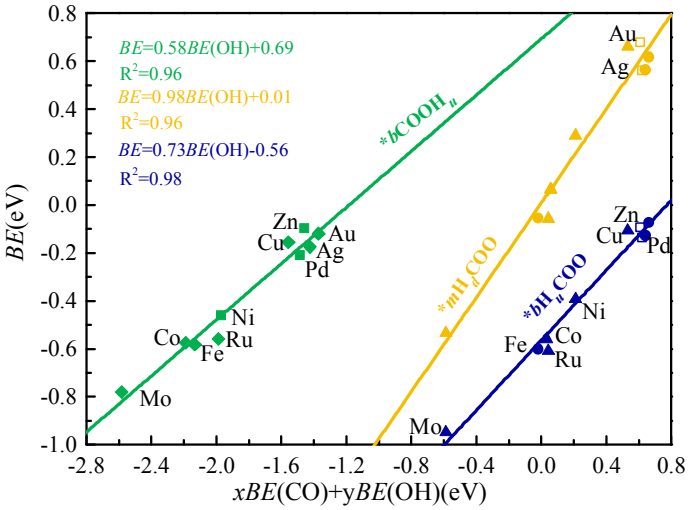

Figure 4.13 Scaling relations of binding energies of reaction intermediates *bCOOH$_u$, *mH$_d$COO and *bH$_u$COO adsorbed on their most stable sites plotted as functions of binding energies of CO and OH. As in Figure 4.2b.

Table 4.7 The binding energy (in eV) of *bH$_u$COO, *mH$_d$COO, *bCOOH$_u$, *OH and *CO adsorbed on M@Pd(111) calculated using CO_2, H_2 and H_2O as references.

Metal	*bH$_u$COO	*mH$_d$COO	*bCOOH$_u$	*CO[a]	*OH
Mo	-0.95	-0.53	-0.78	-2.00	-0.59
Fe	-0.60	-0.05	-0.58	-2.11	-0.02
Ru	-0.61	-0.06	-0.56	-2.31	0.04
Co	-0.56	0.07	-0.57	-2.25	0.03
Ni	-0.39	0.29	-0.46	-2.18	0.21
Cu	-0.11	0.66	-0.15	-2.09	0.53
Zn	-0.09	0.68	-0.10	-2.06	0.61
Ag	-0.13	0.56	-0.17	-2.06	0.64
Au	-0.07	0.62	-0.12	-2.03	0.66
Pd	-0.13	0.56	-0.21	-2.10	0.62

[a]*CO with most stable configuration on M@Pd(111) calculated using their gas-phase as reference.

4.3.4 Microkinetic Modeling

At is known, it still remains challenging for theoretically evaluating potential-dependent activation barriers and reaction rates of FAO elementary steps due to complex reaction mechanism involving coupled ($H^+ + e^-$) pair transfer at electrode–electrolyte interface [12-14]. Here, we adopted the methodology by Nørskov and co-workers [74] to calculate transition states and kinetic barriers of FAO on Ru@Pd(111) with Pd(111) as a benchmark reference. The solvent-assisting proton transfer via the Heyrovsky mechanism at metal/H_2O interface was captured using water-solvated proton transfer approach [59], which was presented by explicitly embedding four H_2O molecules close to adsorbed *HCOOH, *HCOO, and other adsorbates [16, 17], as illustrated in Figure 4.14. As such, the stabilization effect of H_2O solvation on key intermediates particularly the transition-state structure was taken into account by assuming that local interactions of solvated proton within a few angstrom of the electrode surface is most important. Figure 4.14 shows that assisted by surrounding solvated H_2O, the adsorbed *HCOOH can release carboxyl H forming adsorbed *bH$_u$COO and aqueous H_3O^+ on both Ru@Pd(111) and Pd(111) without an activation barrier, unlike those in gas-solid interface (Figure 4.5). Note here that *bHuCOO is most likely to be the sole product of R1 and R2 in aqueous environment and *COOH is less likely to be formed from HCOOH → *COOH → *CO route.

On the basis of DFT-calculated activation barriers, we conducted microkinetic modeling (MK) of FAO catalyzed by Ru@Pd(111) and Pd(111) to evaluate the current efficiency of active site over a wide range of potentials commonly found in experiment. The calculated kinetic parameters are listed in Table 4.8. Here, only the direct mechanism is considered for MK as HCOOH → *COOH → *CO route is completely suppressed. The similar approach was also employed for FAO on Pt(111) regardless of Pt being known for its strong binding of *CO [14].

Figure 4.16 shows that the predicted current density (j, solid blue line) from FAO on Pd(111) has a symmetric bell shape with a maximum value of 3.78 mA cm^{-2} at 0.14 V and a lower onset potential (0.00 V), agreeing well with the experiment on Pd/C but shifting upward to 0.13 V with a higher peak value of 2.10 mA cm^{-2} (dashed blue line)[31]. Noticeably, the current peak appears at the very potential (0.14 V) where a decrease of *bH$_u$COO coverage and an increase of free sites cross each other (black dashed line), i.e., the numbers of adsorbed *bH$_u$COO and free sites are equal (50% each) with no *OH adsorbed. This is reasonable in that *bH$_u$COO ↔ *mH$_d$COO ↔ CO_2 + * + ($H^+ + e^-$) being the PDS is promoted greatly with increasing electrode potential despite *bH$_u$COO ↔ *mH$_d$COO being a non-electrochemical process. With more positive potential applied (>0.17 V) enabling overcoming the barrier for R4 (E_a=1.16eV) in Figure 4.15: H_2O +* ↔ *OH + (H^++e^-), the coverage of *OH produced

from H_2O dissociation increases exponentially accompanying with a decrease of free sites, displaying the coupled symmetric bell shapes (black and deep-yellow lines).

In comparison, FAO on Ru@Pd(111) displays a very similar trend as Pd(111) as shown in Figure 4.16b, however, demonstrates a lower onset potential (-0.35 V) and higher maximum current (15.90 mA cm^{-2}) at 0.24V, in line with that experimentally observed from FAO on PdRu alloy NPs (0.23 V) [27, 28]. Remarkably, adsorbed *OH become competitive with *bH_uCOO for active sites due to its lowered barrier for H_2O dissociation (0.78eV) as in Figure 4.15. The first small peak is concomitant with the exponential decrease of *bH_uCOO coverage and increase of *OH coverage, whereas the second large peak is accompanied by the exponential decrease of *OH coverage and increase of free sites, suggesting H_2O dissociation plays a crucial role of determining the current efficiency of FAO originating from moderate-to-strong *OH binding with Ru active site (Figure 4.18a). This could provide an alternative explanation of similar two peaks experimentally observed from FAO on PdRu alloy NPs[27]. Furthermore, Figure 4.18c shows that the simulated peak current density for FAO on Pd(111) (at pH =1) is increased and shifted upward to higher electrode potential with increasing concentrations of HCOOH, consistent with the experimental observations from FAO on Pd/C electrocatalyst. Additionally, the simulated current density (Figure 4.16d) is increased with increasing pH up to 2 then reaches a plateau (at 0.15V and 0.5M HCOOH), agreeing also well the experiment [75].

Overall, the similar trends with the experiments validate our computational approach, where the simulated current and onset/peak potential for FAO on either Pd(111) or Ru@Pd(111) could be reasonably compared with the experimental measurements [26, 28-33, 75], where the interplays of many controlling factors (e.g., overpotentials arising from such as activation, reaction, diffusion, resistance, and pH, scanning rate, etc.) contribute the measured values.

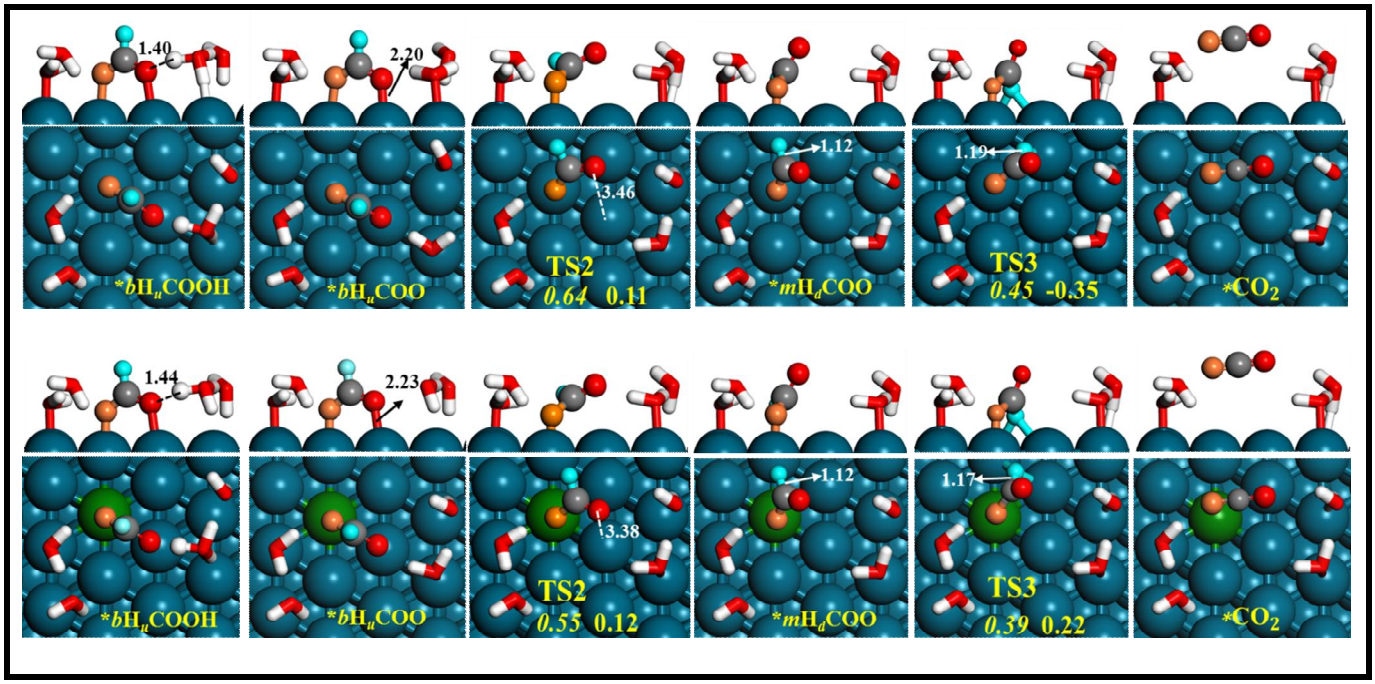

Figure 4.14 Optimized configurations of FAO toward CO_2 via direct mechanism (*HCOO) on Ru@Pd(111) and Pd(111) using HCOOH-$(H_2O)_4$ as the reactant. TS: transition state; Italic numbers: activation energy (in eV); Regular numbers: reaction energy (in eV).

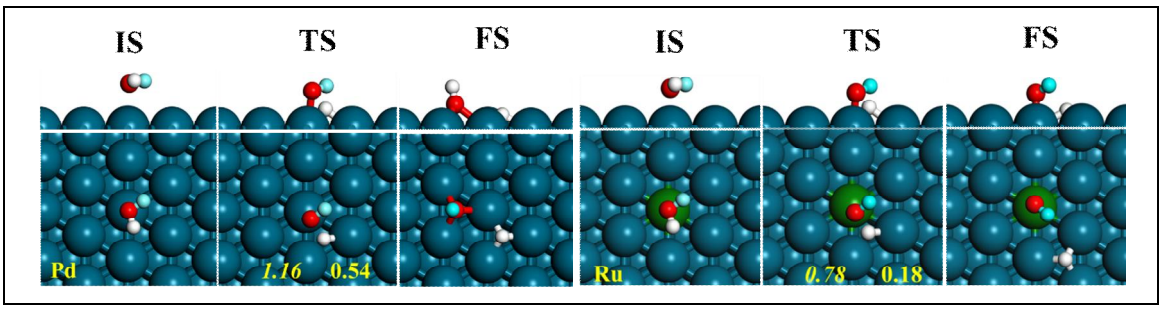

Figure 4.15 Optimized initial state (IS), transition state (TS) and final state (FS) configurations of R_4: $H_2O \leftrightarrow$ *OH + (H^++e^-) on Ru@Pd(111) and Pd(111), activation energy (italic font, in eV) and reaction energy (regular font, in eV) are displayed.

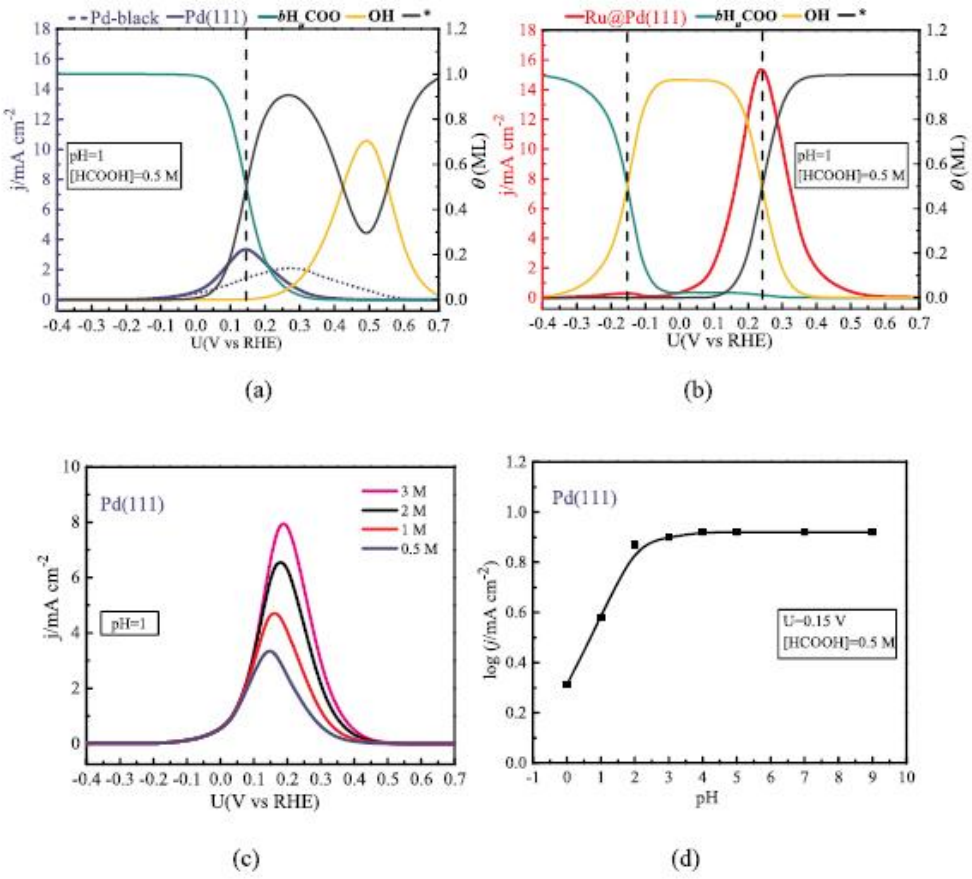

Figure 4.16 Simulated current density (j) and coverage of intermediates ( ) as a function of electrode potential on (a) Pd(111) and (b) Ru@Pd(111); Simulated current density (j) as a function of electrode potential for different concentrations of HCOOH on (c) Pd(111); Simulated current density (j) as a function of pH on (d) Pd(111). The experimental data points were retrieved from FAO on Pd black anode (blue dotted line) [31]. * denote free sites.

Table 4.8 The reaction free energy (ΔG_i, in eV) and activation energy (E_a, in eV) forward rate constants (k^+), backward rate constant (k^-) of each elementary step for FAO at 0 V *vs.* RHE, (pH = 1, 1.0 bar CO_2, and 298.15 K). The adsorption energy of CO_2 was used as E_a of desorption. The average energy of HCOOH and *HCOOH was used as TS energy [5].

	Pd(111)				Ru@Pd(111)			
	ΔG_i	E_a	k^+ (s^{-1})	k^- (s^{-1})	ΔG_i	E_a	k^+ (s^{-1})	k^- (s^{-1})
R_2	0.21	0.22	1.06×10^{7}	1.81×10^{5}	-0.31	0.16	8.02×10^{12}	5.23×10^{20}
R_3	0.23	0.64	5.16×10^{-1}	3.26×10^{-3}	0.34	0.55	2.19×10^{0}	2.25×10^{-4}
R_4	0.54	1.16	1.67×10^{-12}	7.25×10^{-20}	0.18	0.78	5.95×10^{-3}	2.68×10^{-4}

4.4 Conclusions

In this work, we theoretically investigated mechanism, kinetics and descriptor for FAO on M@Pd(111) surface alloys (M = Mo, Fe, Ru, Co, Ni, Cu, Zn, Ag, Au), employed as the bimetallic Pd-based model catalyst. It is revealed that alloyed M single atom can not only act as active site for FAO but also affect the reactivity of nearest-neighboring Pd atoms via the ligand effect (charge transfer). The decoordination of *HCOO from bidentate to monodentate adsorption mode (i.e., $*b\mathrm{H}_u\mathrm{COO} \rightarrow *m\mathrm{H}_d\mathrm{COO}$) followed by the facile carbonyl-H abstraction forming $CO_2 + (H^+ + e^-)$ is identified as the PDS with a free energy barrier of 0.73eV on Ru@Pd(111) against 0.95eV on Pd(111). The oxyphilic Ru atom facilitates such a bidentate-to-monodentate transformation arising from the uneven Ru-O and Pd-O bindings of $*b\mathrm{H}_u\mathrm{COO}$ and the stronger Ru-O binding of $*m\mathrm{H}_d\mathrm{COO}$. The simulated polarization curves agree reasonably well with the experiment, showing Ru@Pd(111) outperforms Pd(111) for promoting FAO via primarily the direct mechanism: HCOOH →*HCOO (formate) → $CO_2 + 2H^+ + 2e^-$. It is predicted that among M studied, Mo@Pd(111) owing to the weakest carbophilicity and stronger oxyphilicity of alloyed Mo could be the most promising bimetallic Pd-based catalyst for FAO. As such, the binding strength of *CO and *OH can be used as an effective descriptor for fast screening of high-performance FAO catalysts.

REFRENCES

[1] K. Sordakis, C. Tang, L.K. Vogt, H. Junge, P.J. Dyson, M. Beller, G. Laurenczy, Homogeneous catalysis for sustainable hydrogen storage in formic acid and alcohols, Chem. Rev., 118 (2018) 372-433.

[2] C. Rice, S. Ha, R. Masel, P. Waszczuk, A. Wieckowski, T. Barnard, Direct formic acid fuel cells, J. Power Sources, 111 (2002) 83-89.

[3] R. Xing, W. Qi, G.W. Huber, Production of furfural and carboxylic acids from waste aqueous hemicellulose solutions from the pulp and paper and cellulosic ethanol industries, Energy Environ. Sci., 4 (2011) 2193-2205.

[4] R.S. Jayashree, J.S. Spendelow, J. Yeom, C. Rastogi, M.A. Shannon, P.J.A. Kenis, Characterization and application of electrodeposited Pt, Pt/Pd, and Pd catalyst structures for direct formic acid micro fuel cells, Electrochim. Acta, 50 (2005) 4674-4682.

[5] E. Antolini, Palladium in fuel cell catalysis, Energy Environ. Sci., 2 (2009) 915-931.

[6] K. Jiang, H.X. Zhang, S. Zou, W.B. Cai, Electrocatalysis of formic acid on palladium and platinum surfaces: from fundamental mechanisms to fuel cell applications, Phys. Chem. Chem. Phys., 16 (2014) 20360-20376.

[7] J. Chang, X. Sun, L. Feng, W. Xing, X. Qin, G. Shao, Effect of nitrogen-doped acetylene carbon black supported Pd nanocatalyst on formic acid electrooxidation, J. Power Sources, 239 (2013) 94-102.

[8] J. Chang, S. Li, L. Feng, X. Qin, G. Shao, Effect of carbon material on Pd catalyst for formic acid electrooxidation reaction, J. Power Sources, 266 (2014) 481-487.

[9] J.Y. Wang, H.X. Zhang, K. Jiang, W.B. Cai, From HCOOH to CO at Pd electrodes: a surface-enhanced infrared spectroscopy study, J. Am. Chem. Soc., 133 (2011) 14876-14879.

[10] H. Miyake, T. Okada, G. Samjeske, M. Osawa, Formic acid electrooxidation on Pd in acidic solutions studied by surface-enhanced infrared absorption spectroscopy, Phys. Chem. Chem. Phys., 10 (2008) 3662-3669.

[11] S. Hu, F. Che, B. Khorasani, M. Jeon, C.W. Yoon, J.-S. McEwen, L. Scudiero, S. Ha, Improving the electrochemical oxidation of formic acid by tuning the electronic properties of Pd-based bimetallic nanoparticles, Appl. Catal., B, 254 (2019) 685-692.

[12] J. Joo, T. Uchida, A. Cuesta, M.T.M. Koper, M. Osawa, The effect of pH on the electrocatalytic oxidation of formic acid/formate on platinum: A mechanistic study by surface-

enhanced infrared spectroscopy coupled with cyclic voltammetry, Electrochim. Acta, 129 (2014) 127-136.

[13] A. Cuesta, G. Cabello, M. Osawa, C. Gutiérrez, Mechanism of the electrocatalytic oxidation of formic acid on metals, ACS Catal., 2 (2012) 728-738.

[14] J. Joo, T. Uchida, A. Cuesta, M.T. Koper, M. Osawa, Importance of acid-base equilibrium in electrocatalytic oxidation of formic acid on platinum, J. Am. Chem. Soc., 135 (2013) 9991-9994.

[15] A.O. Elnabawy, J.A. Herron, J. Scaranto, M. Mavrikakis, Structure sensitivity of formic acid electrooxidation on transition metal surfaces: a first-principles study, J. Electrochem. Soc., 165 (2018) J3109-J3121.

[16] W. Gao, J.A. Keith, J. Anton, T. Jacob, Theoretical elucidation of the competitive electrooxidation mechanisms of formic acid on Pt (111), J. Am. Chem. Soc., 132 (2010) 18377-18385.

[17] H.F. Wang, Z.P. Liu, Formic acid oxidation at Pt/H_2O interface from periodic DFT calculations integrated with a continuum solvation model, J. Phys. Chem. C, 113 (2009) 17502-17508.

[18] X. Yu, P.G. Pickup, Recent advances in direct formic acid fuel cells (DFAFC), J. Power Sources, 182 (2008) 124-132.

[19] N. Hoshi, K. Kida, M. Nakamura, M. Nakada, K. Osada, Structural effects of electrochemical oxidation of formic acid on single crystal electrodes of palladium, J. Phys. Chem. B, 110 (2006) 12480-12484.

[20] K.D. Gilroy, A. Ruditskiy, H.C. Peng, D. Qin, Y. Xia, Bimetallic nanocrystals: syntheses, properties, and applications, Chem. Rev., 116 (2016) 10414-10472.

[21] W. An, P. Liu, Rationalization of Au concentration and distribution in AuNi@ Pt core–shell nanoparticles for oxygen reduction reaction, ACS Catal., 5 (2015) 6328-6336.

[22] W. An, P. Liu, Size and Shape Effects of Pd@Pt Core–Shell Nanoparticles: Unique Role of Surface Contraction and Local Structural Flexibility, J. Phys. Chem. C, 117 (2013) 16144-16149.

[23] H. Wang, W. An, X. Liu, C.H. Turner, Oxygen reduction reaction on Pt (111), Pt (221), and Ni/Au 1 Pt 3 (221) surfaces: probing scaling relationships of reaction energetics and interfacial composition, Chem. Eng. Sci., 184 (2018) 239–250.

[24] W. An, Y. Men, J. Wang, P. Liu, Interfacial and alloying effects on activation of ethanol from first-principles, J. Phys. Chem. C, 121 (2017) 5603-5611.

[25] R. Larsen, J. Zakzeski, R.I. Masel, Unexpected Activity of Palladium on Vanadia Catalysts for Formic Acid Electro-oxidation, Electrochem. Solid-State Lett., 8 (2005) A291.

[26] M.A. Matin, J.-H. Jang, Y.-U. Kwon, PdM nanoparticles (M = Ni, Co, Fe, Mn) with high activity and stability in formic acid oxidation synthesized by sonochemical reactions, J. Power Sources, 262 (2014) 356-363.

[27] D. Wu, M. Cao, M. Shen, R. Cao, Sub-5 nm Pd-Ru nanoparticle alloys as efficient catalysts for formic acid electrooxidation, ChemCatChem, 6 (2014) 1731-1736.

[28] X. Kang, K. Miao, Z. Guo, J. Zou, Z. Shi, Z. Lin, J. Huang, S. Chen, PdRu alloy nanoparticles of solid solution in atomic scale: Size effects on electronic structure and catalytic activity towards electrooxidation of formic acid and methanol, J. Catal., 364 (2018) 183-191.

[29] M. Yin, Q. Li, J.O. Jensen, Y. Huang, L.N. Cleemann, N.J. Bjerrum, W. Xing, Tungsten carbide promoted Pd and Pd–Co electrocatalysts for formic acid electrooxidation, J. Power Sources, 219 (2012) 106-111.

[30] R. Li, Z. Wei, T. Huang, A. Yu, Ultrasonic-assisted synthesis of Pd–Ni alloy catalysts supported on multi-walled carbon nanotubes for formic acid electrooxidation, Electrochim. Acta, 56 (2011) 6860-6865.

[31] C. Li, Q. Yuan, B. Ni, T. He, S. Zhang, Y. Long, L. Gu, X. Wang, Dendritic defect-rich palladium-copper-cobalt nanoalloys as robust multifunctional non-platinum electrocatalysts for fuel cells, Nat. Commun., 9 (2018) 3702.

[32] G.S. Hammond, A Correlation of Reaction Rates, J. Am. Chem. Soc., 77 (1955) 334-338.

[33] M.D. Obradović, S.L. Gojković, HCOOH oxidation on thin Pd layers on Au: self-poisoning by the subsequent reaction of the reaction product, Electrochim. Acta, 88 (2013) 384-389.

[34] L. Feng, J. Chang, K. Jiang, H. Xue, C. Liu, W.-B. Cai, W. Xing, J. Zhang, Nanostructured palladium catalyst poisoning depressed by cobalt phosphide in the electro-oxidation of formic acid for fuel cells, Nano Energy, 30 (2016) 355-361.

[35] J. Chang, L. Feng, C. Liu, W. Xing, X. Hu, An effective Pd–Ni2P/C anode catalyst for direct formic acid fuel cells, Angew. Chem. Int. Ed., 53 (2014) 122-126.

[36] S. Wang, J. Chang, H. Xue, W. Xing, L. Feng, Catalytic stability study of a Pd‐Ni2P/C catalyst for formic acid electrooxidation, ChemElectroChem, 4 (2017) 1243-1249.

[37] F.R. Lucci, J. Liu, M.D. Marcinkowski, M. Yang, L.F. Allard, M. Flytzani-Stephanopoulos, E.C. Sykes, Selective hydrogenation of 1,3-butadiene on platinum-copper alloys at the single-atom limit, Nat. Commun., 6 (2015) 9550.

[38] G.X. Pei, X.Y. Liu, A. Wang, A.F. Lee, M.A. Isaacs, L. Li, X. Pan, X. Yang, X. Wang, Z. Tai, K. Wilson, T. Zhang, Ag alloyed Pd single-atom catalysts for efficient selective hydrogenation of acetylene to ethylene in excess ethylene, ACS Catal., 5 (2015) 3717-3725.

[39] P.N. Duchesne, Z.Y. Li, C.P. Deming, V. Fung, X. Zhao, J. Yuan, T. Regier, A. Aldalbahi, Z. Almarhoon, S. Chen, D.E. Jiang, N. Zheng, P. Zhang, Golden single-atomic-site platinum electrocatalysts, Nat. Mater., 17 (2018) 1033-1039.

[40] X. Jia, W. An, Z. Wang, J. Zhou, Effect of doped metals on hydrodeoxygenation of phenol over Pt-based bimetallic alloys: Caryl–OH versus caliphatic H–OH bond scission, J. Phys. Chem. C, 123 (2019) 16873-16882.

[41] M.J. Cheng, E.L. Clark, H.H. Pham, A.T. Bell, M. Head-Gordon, Quantum mechanical screening of single-atom bimetallic alloys for the selective reduction of CO2 to C1 hydrocarbons, ACS Catal., 6 (2016) 7769-7777.

[42] G. Kresse, J. Furthmüller, Efficient iterative schemes for ab initio total-energy calculations using a plane-wave basis set, Phys. Rev. B, 54 (1996) 11169-11186.

[43] G. Kresse, J. Hafner, Ab initio molecular dynamics for liquid metals, Phys. Rev. B, 47 (1993) 222-229.

[44] J.P. Perdew, K. Burke, M. Ernzerhof, Generalized gradient approximation made simple, Phys. Rev. Lett., 77 (1996) 3865-3868.

[45] G. Kresse, D. Joubert, From ultrasoft pseudopotentials to the projector augmented-wave method, Phys. Rev. B, 59 (1999) 1758-1775.

[46] P.E. Blöchl, Projector augmented-wave method, Phys. Rev. B, 50 (1994) 17953-17979.

[47] H.J. Monkhorst, J.D. Pack, Special points for Brillouin-zone integrations, Phys. Rev. B, 13 (1976) 1746-1747.

[48] G. Henkelman, B.P. Uberuaga, H. Jónsson, A climbing image nudged elastic band method for finding saddle points and minimum energy paths, J. Chem. Phys., 113 (2000) 9901-9904.

[49] A. Heyden, A.T. Bell, F.J. Keil, Efficient methods for finding transition states in chemical reactions: Comparison of improved dimer method and partitioned rational function optimization method, J. Chem. Phys., 123 (2005) 224101.

[50] G. Henkelman, H. Jónsson, A dimer method for finding saddle points on high dimensional potential surfaces using only first derivatives, J. Chem. Phys., 111 (1999) 7010-7022.

[51] G. Henkelman, A. Arnaldsson, H. Jónsson, A fast and robust algorithm for Bader decomposition of electronic density, Comput. Mater. Sci, 36 (2006) 354-360.

[52] J.K. Nørskov, J. Rossmeisl, A. Logadottir, L. Lindqvist, J.R. Kitchin, T. Bligaard, H. Jonsson, Origin of the overpotential for oxygen reduction at a fuel-cell cathode, J. Phys. Chem. B, 108 (2004) 17886-17892.

[53] H. Wang, W. An, Promoting the oxygen reduction reaction with gold at step/edge sites of Ni@AuPt core–shell nanoparticles, Catal. Sci. Technol., 7 (2017) 596-606.

[54] I.A.W.Z. Filot, B.; Hensen, E. J. M. http://www.mkmcxx.nl.

[55] S.A. Vilekar, I. Fishtik, R. Datta, Kinetics of the hydrogen electrode reaction, J. Electrochem. Soc., 157 (2010) B1040-B1050.

[56] H.A. Hansen, V. Viswanathan, J.K. Nørskov, Unifying kinetic and thermodynamic analysis of 2 e– and 4 e– reduction of oxygen on metal surfaces, J. Phys. Chem. C, 118 (2014) 6706-6718.

[57] J. Greeley, J.K. Nørskov, Electrochemical dissolution of surface alloys in acids: thermodynamic trends from first-principles calculations, Electrochim. Acta, 52 (2007) 5829-5836.

[58] A. Ferre-Vilaplana, J.V.c. Perales-Rondón, J.M. Feliu, E. Herrero, Understanding the effect of the adatoms in the formic acid oxidation mechanism on Pt (111) electrodes, ACS Catal., 5 (2014) 645-654.

[59] Y. Feng, W. An, Z. Wang, Y. Wang, Y. Men, Y. Du, Electrochemical CO2 reduction reaction on M@ Cu (211) bimetallic single-atom surface alloys: mechanism, kinetics and catalyst screening, ACS Sustainable Chem. Eng., (2019) DOI: 10.1021/acssuschemeng.1029b05183.

[60] S. Singh, S. Li, R. Carrasquillo-Flores, A.C. Alba-Rubio, J.A. Dumesic, M. Mavrikakis, Formic acid decomposition on Au catalysts: DFT, microkinetic modeling, and reaction kinetics experiments, AlChE J., 60 (2014) 1303-1319.

[61] L. Ou, J. Chen, Y. Chen, J. Jin, Mechanistic study of Pt-catalyzed electrooxidation of HCOOH in acid medium: kinetic considerations on the effect of solvation, J. Phys. Chem. C, 122 (2018) 24871-24884.

[62] J.A. Herron, J. Scaranto, P. Ferrin, S. Li, M. Mavrikakis, Trends in formic acid decomposition on model transition metal surfaces: a density functional theory study, ACS Catal., 4 (2014) 4434-4445.

[63] Y. Wang, Y. Qi, D. Zhang, C. Liu, New insight into the decomposition mechanism of formic acid on Pd(111): competing formation of CO2 and CO, J. Phys. Chem. C, 118 (2014) 2067-2076.

[64] J. Scaranto, M. Mavrikakis, Density functional theory studies of HCOOH decomposition on Pd(111), Surf. Sci., 650 (2016) 111-120.

[65] R. Zhang, H. Liu, B. Wang, L. Ling, Insights into the Preference of CO2 Formation from HCOOH Decomposition on Pd Surface: A Theoretical Study, J. Phys. Chem. C, 116 (2012) 22266-22280.

[66] C. Hu, S. Ting, K. Chan, W. Huang, Reaction pathways derived from DFT for understanding catalytic decomposition of formic acid into hydrogen on noble metals, Int. J. Hydrogen Energy, 37 (2012) 15956-15965.

[67] M. Zhang, Y. Wu, M. Dou, Y. Yu, A DFT study of methanol synthesis from CO2 hydrogenation on the Pd(111) surface, Catal. Lett., 148 (2018) 2935-2944.

[68] K.P. Kepp, A quantitative scale of oxophilicity and thiophilicity, Inorg. Chem., 55 (2016) 9461-9470.

[69] J. Zhou, W. An, Z. Wang, X. Jia, Hydrodeoxygenation of phenol over Ni-based bimetallic single-atom surface alloys: mechanism, kinetics and descriptor, Catal. Sci. Technol., 9 (2019) 4314-4326.

[70] X. Yu, P.G. Pickup, Screening of PdM and PtM catalysts in a multi-anode direct formic acid fuel cell, J. Appl. Electrochem., 41 (2011) 589-597.

[71] C. Song, M. Khanfar, P.G. Pickup, Mo oxide modified catalysts for direct methanol, formaldehyde and formic acid fuel cells, J. Appl. Electrochem., 36 (2005) 339-345.

[72] D. Wu, Z. Zheng, S. Gao, M. Cao, R. Cao, Mixed-phase PdRu bimetallic structures with high activity and stability for formic acid electrooxidation, Phys. Chem. Chem. Phys., 14 (2012) 8051-8057.

[73] J.S. Yoo, F. Abild-Pedersen, J.K. Nørskov, F. Studt, Theoretical analysis of transition-metal catalysts for formic acid decomposition, ACS Catal., 4 (2014) 1226-1233.

[74] H.A. Hansen, J.B. Varley, A.A. Peterson, J.K. Nørskov, Understanding trends in the electrocatalytic activity of metals and enzymes for CO2 reduction to CO, J. Phys. Chem. Lett., 4 (2013) 388-392.

[75] Y. Wang, B. Wu, Y. Gao, Y. Tang, T. Lu, W. Xing, C. Liu, Kinetic study of formic acid oxidation on carbon supported Pd electrocatalyst, J. Power Sources, 192 (2009) 372-375.

5 Pd@Mo Bimetallic Alloys Catalyst: The Role of the Mo Ensemble for Electrochemical Oxidation of Formic Acid

5.1 Introduction

Direct formic acid fuel cell (DFAFC) has a potential fuel cell due to a high theoretical open circuit potential (1.48 V), a higher fuel concentration, a lower fuel crossover and low toxicity of FA at room temperature with concerning other types of fuel cells (e.g., PEMFC, DMFC) in the low-temperature [1, 2]. Bimetallic Pd-based alloys catalysts have been extensively studied for electrooxidation of formic acid (FAO) owing to its high CO tolerance and activity [3, 4].

We have reported the FAO over bimetallic Pd-based single-atom surface alloys denoted as M@Pd(111) where M = Mo, Fe, Ru, Co, Ni, Cu, Zn, Ag, Au (total of 9 elements) on Pd(111) surface by the density functional theory (DFT) calculations. The potential-determining step (PDS) of the direct pathway is $*bH_uCOO \rightarrow *mH_dCOO$ as effective catalytic descriptors for FAO activity. The most promising bimetallic Pd-based catalyst for FAO is Mo@Pd(111) due to the weakest carbophilicity and stronger oxyphilicity [5]. However, it is worth noting that the measured FAO performance catalysed by PdMo alloy is controversial in the experiment, from which both enhanced [6] and decreased [7] FAO performance were observed relative to Pd. Which enhances the performance of FAO with a decreasing amount of Mo. Therefore, Mo ensemble Pd plays an important role for FAO. For example, Pd/Cu has a good catalytic activity toward HCOOH dissociation into CO_2 and reduce the formation of CO, Pd ensemble on the Pd_6Cu_3 and Pd_9Cu_0 surfaces with the Pd/Cu ratio of 6/3 and 9/0 exhibit higher selectivity and activity toward CO_2 formation via the COOH intermediate, especially, Pd_6Cu_3 is superior to the single Pd; whereas the isolated Pd atom on the Pd_1Cu_8 and Pd_3Cu_6 surfaces with the Pd/Cu ratio of 1/8 and 3/6 dominantly produce CO via the COOH intermediate [8]. Duchesne and co-workers found that single-atom Pt sites on the AuPt alloy surface greatly promote FAO via the direct mechanism meanwhile inhibiting the *CO formation in indirect mechanism mainly through the ensemble effect, resulting in superior catalytic activity and selectivity [9]. PtAu as an excellent catalyst of FAO, PtAu(111) alloy surface FAO mechanism in aqueous solution phase has been verified by DFT calculation, in which 3 adjacent Pt atom has a good performance for the formation of CO_2 directly and CO-poison via to dimer pathway and single atom is benefit for formate pathway for FAO[10]. The explicit solvation model is closer to the real FAO condition, there are some researches to report that the explicit solvation model has significant effects [10-13], such as $HCOOH_{ad}$(CH-down) is the dominant pathway with the low transition state 0.45eV on Pt(111) surface [12].

Herein, using density functional theory (DFT) calculations, we systematically investigated FAO over bimetallic MoPd(111), among them, Mo ensemble on the Pd surface that coverage degree 1/16 (Mo_1Pd), 2/16 (Mo_2Pd), 3/16 (Mo_3Pd)and 4/16 (Mo_4Pd) ML with the explicit water model. Our focus is on the role of alloyed Mo ensemble effects. It is valuable for reveal microscopic details of FAO on MoPd(111), which is beneficial for the engineering and optimization of single-site catalysts.

5.2 Models and computational methods

5.2.1 Models

MoPd(111) was modelled by a four-layer close-packed p(4×4) slab of Pd(111) with Pd atoms of the top layer replaced by Mo atoms, corresponding to 1/16, 2/16, 3/16 and 4/16 ML of isolated Mo atoms. The explicit solvation model containing four H_2O molecules adjacent to (111) surface [11, 14] was employed for the whole elementary steps of FAO. A vacuum region in the z-direction was set to 15 Å and the surface is periodic in the x- and y-direction. The size of chosen supercell is sufficiently large to avoid the interactions between the imaging cells. During the optimization, the adsorbates and the top two-layer metal atoms were allowed to relax while the bottom two layers were fixed at their bulk positions (Pd: 3.891 Å).

5.2.2 Computational methods

All DFT calculations were performed with the Vienna ab-initio simulation package (VASP) [15, 16] using the RPBE exchange-correlation functional [17] of the generalized gradient approximation (GGA) and the projector augmented wave (PAW) pseudopotential [18, 19] for describing the core−valence interactions. The plane-wave cutoff energy was set to 400 eV. The Brillouin zone was sampled by a Γ-centered Monkhorst−Pack scheme [20] with 2 × 2 × 1 and 5 × 5 × 1 k-points grids for geometry optimization and electronic structure calculations, respectively. The conjugate gradient algorithm was used in ionic optimization. The convergence threshold was set to 10^{-4} eV for electronic relaxation and 0.02 eV/Å for forces. Fermi-smearing of k_{BT} = 0.1 eV was employed to speed up the convergence. All reported energies are extrapolated to k_{BT} = 0 eV. The transition states (TSs) were searched using the climbing image nudged elastic band (CI-NEB) method [21], combined with improved dimer method (IDM) [22, 23], in which all force components were relaxed below 0.02 eV/Å. Bader charge analysis was used to calculate the partial charge transfer [24]. Gibbs free energy of reaction for FAO elementary steps involving ($H^+ + e^-$) pair transfer was calculated using computational hydrogen electrode (CHE) model [25, 26], which has been successfully employed for a variety of electrochemical systems including FAO [25, 27]. The limiting potential (U_L) is obtained from the maximum free energy change (ΔG_{max}) among all elementary steps along the lowest-energy

pathway by using the relation of $U_L = -\Delta G_{max}/e$, where e is the unit charge. Theoretical overpotential is defined as $\square = U_0 - U_L$, where U0 is the equilibrium potential of FAO (i.e., -0.25 V). The dissolution potentials (U_{dis}, in V) of M in M@Pd(111) at pH=0 were calculated as $U_{dis} = U_{M0} + [E_{M,bulk} - (E_{M@Pd(111)} - E_{Pd(111)})]/ne$, where U_{M0} is the standard dissolution potentials of M in the bulk form, $E_{M,bulk}$, $E_{M@Pd(111)}$ and $E_{Pd(111)}$ are the total energy of one M atom in the bulk, M-allyed Pd(111) and Pd(111) with M being dissolved out, respectively [28], and n is the coefficient for aqueous dissolution reaction: $M + nH^+ + M^{n+} + n/2H_2$, where more positive values indicate more stable of M, and e is unit charge. The formation energies of different Mo ensembles on the Pd(1 1 1) surface are calculated to characterize the thermal stability of these ensembles, as defined in ref [29]:

$$\Delta E_{Pd} = -(E_{MoPd} - E_{pd\text{-}slab})/N_{Mo} - (E_{Pd\text{-}bulk} - E_{Pd\text{-}atom})$$

Where E_{MoPd}, $E_{pd\text{-}slab}$, $E_{Pd\text{-}bulk}$ and $E_{Pd\text{-}atom}$ represent the total energies of the MoPd slab, an isolated Pd slab, bulk cohesive energies of Pd, and an isolated Pd atom, respectively. N_{Mo} represents the number of Mo atoms alloyed into the Pd surface.

$$BE = E_{Mo@Pd(111)} - E_{Pd(111)} - E_{Mo}$$

where $E_{Mo@Pd(111)}$, $E_{Pd(111)}$ and E_{Mo} are total energy of Mo-allyed Pd(111), Pd(111) with Mo being dissolved out, and isolated single atom, respectively.

5.3 Results and discussion

5.3.1 Stability of M@Pd(111)

We consider that the centre of activity is Mo atom, in which Mo ensembles ML1/16, 2/16, 3/16 and 4/16, All structures were showed in Figure 5.1. Among them, Mo_2Pd have three structures includes adjacent/A, diagonal interval/ID and liner interval/LD. Mo_3Pd was discussed five generates include hollow/H, v shap/V, line/L and triangle/T. To evaluate the stability of Mo ensembles alloy embedded in Pd(111) surface layer in strong acidic media, we calculated the dissolution potentials (U_{dis}) and [28] of M in M@Pd(111) at pH=0 and formation energies (ΔE_{Pd}) in gas phase using ΔE_{Pd} of Mo_1Pd as reference, as shown in Table 5.1. FAO reaction sites take place around Mo atoms due to the high adsorption energy of OH as well as the key intermediate formate (HCOO) by previous study [5]. The stability of Pd ensembles increased with the numbers of Pd atoms decreasing on Pd(1 1 1) this trend is similar with the Pd state-to-state ensembles on Au(111) [29]. There are similar formation energies for the same numbers of Mo of different structures. Therefore, it is more benefit to form the single atom MoPd. An addition, the dissolution potentials (U_{dis}) [28] of MoPd were calculated at pH=0 in a strong acidic media. It can be seen that all MoPd(111) have positive U_{dis} values expect Mo_3Pd (H) and Mo_4Pd, indicatives of surviving the medium of pH=0. With $Mo_1Pd(111)$

as a reference, all MoPd(111) studied become less stable with the lowered and/or less positive Udis values, i.e., Mo_4Pd (-0.01 V) = Mo_3Pd/H (-0.01 V) < Mo_3Pd/V(0.02 V) < Mo_3Pd/T (0.02V)< Mo_3Pd/L (0.07 V) < Mo_2Pd/DI (0.11 V) < Mo_2Pd/LI (0.15 V) < Mo_2Pd/A (0.16 V)< Mo_1Pd (0.21 V), but are still more stable than their bulk counterparts of Mo based on $U_{dis} > U_{Mo.}$ The DFT-calculated binding energy (BE) also suggests that MoPd(111) are highly stable with respect to Pd(111). The coverage degree was up to 4/16 ML, we just consider parallelogram structure, a detailed explanation is given below.

We have found that the potential-determining step (PDS) of FAO is $*bH_uCOO \leftrightarrow *mH_dCOO$ in pervious study [5], hence, we calculated the intermidates of PDS as shown in Figure 5.2, there are binding energy (BE) of $*mH_dCOO$ rather $*bH_uCOO$ were compared with histogram, in which the larger difference of $*mH_dCOO$ and $*bH_uCOO$ exist on the adjacent Mo atoms of Mo_2Pd and Mo_3Pd due to the strong oxyphilicity. It must have a high barrier owing to the larger difference value of BE of initiating configuration and final configuration. Nevertheless, the interval Mo atoms was embedded in the Pd(111) that exist the lower difference value of BE for the PDS species include Mo_1Pd, Mo_2Pd/DI, Mo_2Pd/LI and Mo_3Pd/T was discussed in next study and marked by red boxes in Figure 5.2. Meanwhile, the coverage degree was considered so the Mo_4Pd alloy surface has been researched as the highest coverage degree under interval atoms condition.

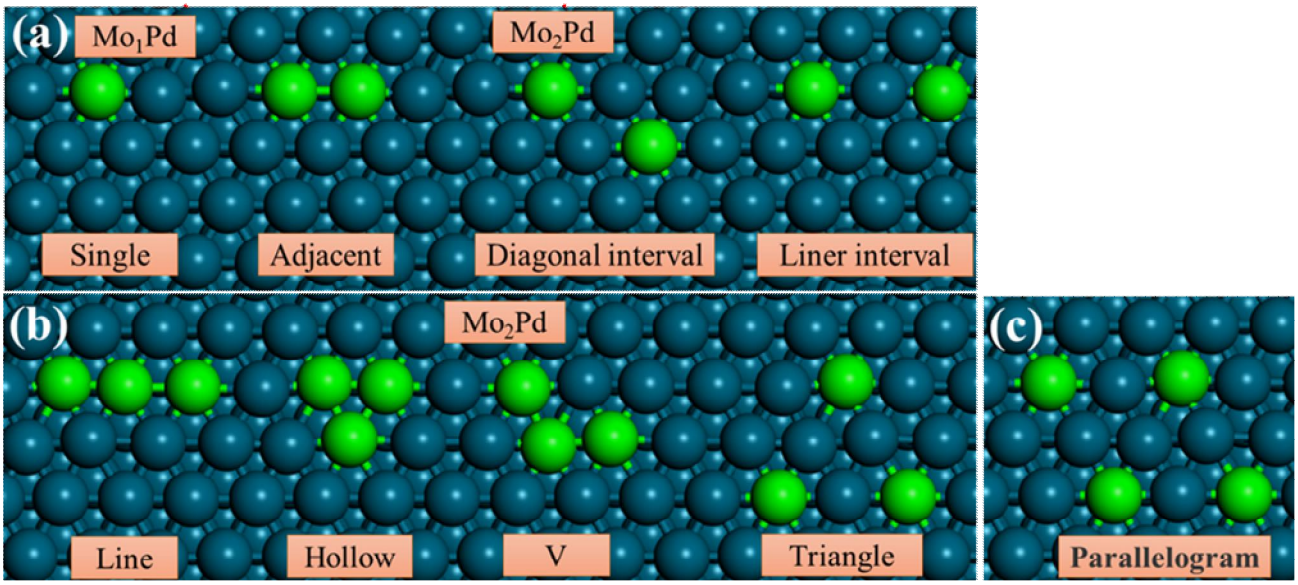

Figure 5.1 The structures for the Mo ensembles on Pd(111)

Table 5.1 Table DFT-calculated formation energies (ΔE_{Pd}) using the Mo_1Pd as refrence, binding energy (BE)*, dissolution potential (U_{dis}) of M in Mo@Pd(111), where $M + nH^+ \leftrightarrow M^{n+} + n/2H_2$ at pH=0.

Structure	ΔE_{Pd}(eV)	U_{dis}(V *vs.* RHE)	BE(eV)
Mo_1Pd	0.00	0.21	-11.24
Mo_2Pd/DI	-0.12	0.16	-11.11
Mo_2Pd/LI	-0.16	0.15	-11.06
Mo_2Pd/A	-0.18	0.11	-10.95
Mo_3Pd/L	-0.37	0.07	-10.82
Mo_3Pd/TI	-0.39	0.02	-10.68
Mo_3Pd/V	-0.40	0.02	-10.68
Mo_3Pd/H	-0.41	-0.01	-10.60
Mo_4Pd	-0.61	-0.01	-10.59

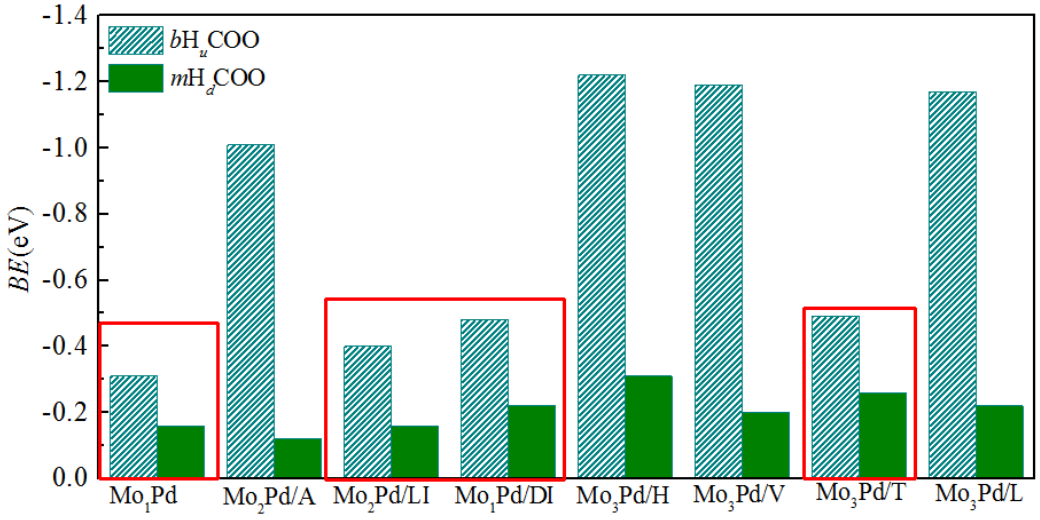

Figure 5.2 The binding energy (BE) of *bH$_u$COO in turquoise and *mH$_d$COO in green for the 1, 2 and 3 Mo atoms ensembles on Pd(111). Both *monodentate (m)* and *bidentate (b)* adsorption modes of *HCOO were clearly marked with orientation of the H atom involving C-H and O-H bond forming/breaking. Specifically, Hu is for 'upward' and Hd is for 'downward' of H atom against the surface were specified. $E[CH_xO_y] = E[CO_2] + [(4+x-2y)/2]*E[H_2] - (2-y)*E[H_2O]$, calculated using gas-phase CO_2, H_2 and H_2O energy as the reference

5.3.2 Electronic Structure of M@Pd(111)

Regarding Mo-Pd bonding situation, there exists the substantial electron charge transfer from Mo atom to host Pd atoms (equivalently, the oxidation state of M^{+}), i.e., $Mo^{1.00+}$ (Mo_1Pd) > $Mo^{0.98+}$ (Mo_2Pd/LI) = $Mo^{0.98+}$ (Mo_1Pd/DI) > $Mo^{0.94+}$ (Mo_3Pd/T) > $Mo^{0.87+}$ (Mo_4Pd), in which we use the electro charge transfer of average single atom. An indicative of the formation of polarized heteroatom Pd-Mo bonds, which enable the tuning of the electronic structure of local active sites adjacent to Mo atom. The most electron charge transfer of single atom is consistent with the observation from the most stable of Mo_1Pd. The partial positive charge of doped atom could have beneficial effect on the modified surface for promoting FAO [30]. As can be seen from Figure 5.3, the calculated binding energy of adsorbed *OH increases proportionally with the closer Femi level of d-band centre of surface atoms where the adsorbates are bound, showing alloyed Mo atom can not only act as active site but also affect the reactivity of nearest-neighbouring Pd atoms via the ligand effect (charge transfer). The OH best stale sites change due influence of additives explicit water model, and BE slight enhance owing to the water can stable the adsorptions [31]. Enhancing the explicit water model is closer the real electrochemical condition. More importantly, binding strength of *OH can be used as an indicator for oxyphilicity of alloyed Mo [32], from which an effective descriptor may be derived for FAO catalyst design.

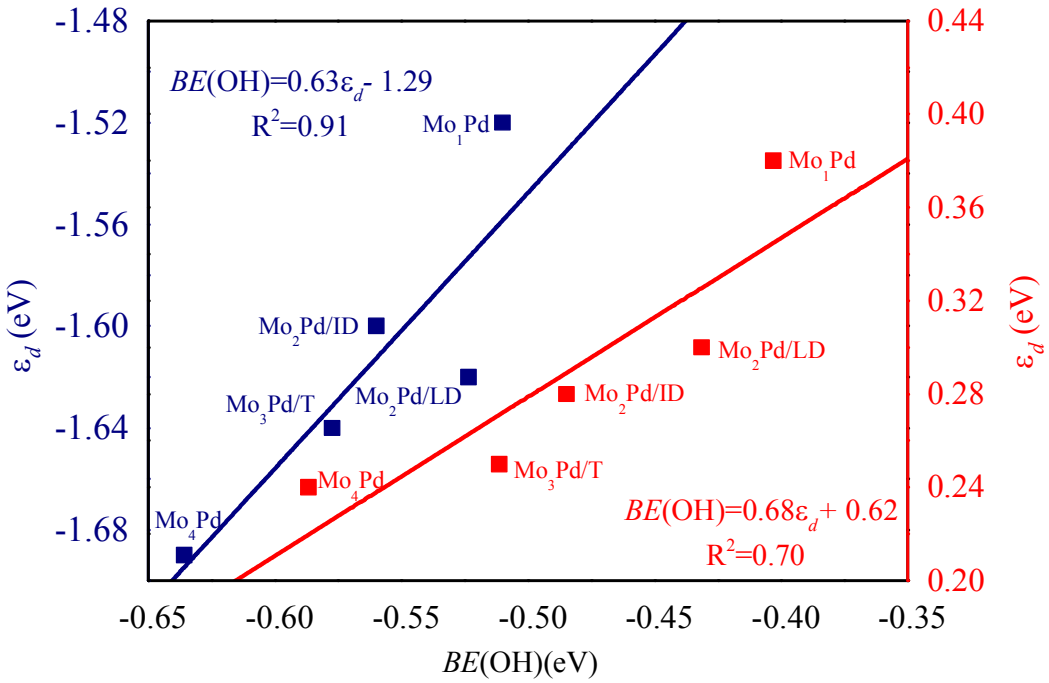

Figure 5.3 Linear correlation between *OH binding energy (BE) and *d*-band centre (ε_d) of active sites, where are favourably adsorbed. OH adsorbed on top site of Mo in gas phase and 3-fold hollow site of Pd-Mo-Pd in aqueous phase by red and blue, respectively.

5.3.3 Mechanistic aspect of FAO on Ru@Pd(111).

At is known, it still remains challenging for theoretically evaluating potential-dependent activation barriers and reaction rates of FAO elementary steps due to complex reaction mechanism involving coupled ($H^+ + e^-$) pair transfer at electrode–electrolyte interface [33-35]. Here, we adopted the methodology by Nørskov and co-workers [36] to calculate transition states on MoPd(111). The solvent-assisting proton transfer via the Heyrovsky mechanism at metal/H2O interface was captured using water-solvated proton transfer approach[32], which was presented by explicitly embedding four H2O molecules close to adsorbed *HCOOH, *HCOO, and other adsorbates[11, 14]However, our calculated results using explicit solvation model of H_2O demonstrate that H_2O-assisted HCOOH adsorption at electrochemical interface of H2O/MoPd(111) results in facile release of carboxyl H forming adsorbed *bH$_u$COO, which suppress HCOOH →*COOH→*CO route [37-39]. BE of poison-CO have been considered in Table 5.2, where Mo_1Pd and Mo_2Pd/L have relatively higher while lower than previous study [5].

BE of all adsorptions is shown in the Table 5.3, in which Mo_2Pd/DI has a high BE result in the O-H broken but there is no existence another key species *mH_dCOO leading to the difficult of C-H session. So Only Mo_2Pd/LI is considered at letter. As shown in Figure 5.2, there exists the subtle discrepancy of adsorbed configuration of *HCOOH in that *H_uCOOH_u (BE=-0.84 eV) has carbonyl H atom (cyan ball) and hydroxyl H atom (white ball) pointing upward(u) on Mo_1Pd, however, there *H_pCOOH_p, *H_dCOOH_d has carbonyl H atom (cyan ball) and hydroxyl H atom (white ball) pointing parallel(p) and downward(d) against the catalyst surface except *H_uCOOH_u on other catalytic surface same as on low-miller index Au facets[40], which have important implication of how dehydrogenation of *HCOOH is initiated. The adsorbed *H_uCOOH_u is benefit for the formation of formate *HCOO (HCOOH → *HCOO → $CO_2 + 2H^+ + 2e^-$) while the adsorbed *H_dCOOH_d favors the formation of CO_2 directly (HCOOH→ $CO_2 + 2H^+ + 2e^-$) like pure Pt(111) sueface [12]. *H_dCOOH_d exist these situations of dehydrogenation in FAO. Additionally, adsorbed configuration of *H_pCOOH_p (BE=0.03 eV) is the most stable on Mo_2Pd/LI, *H_pCOOH_p (BE=-0.27eV) and *H_uCOOH_u (BE=-0.26eV) are relatively stable on the Mo3Pd/T while adsorbed *H_dCOOH_d (BE=-0.33eV) is the most stable on Mo_4Pd.

It has been reported that the cleavage of O-H bond of HCOOH is the first step for FAO on some metal surfaces [41-44]. As can be seen from Figure 5.4a, *H_uCOOH_u configuration is highly preferred for facilitating O-H bond scission to form *HCOO without encountering geometric frustration on Mo1Pd, for direct mechanism, the PDS is identified as the decoordination of adsorbed state from bidentate to monodentate *HCOO (*bH$_u$COO →

*mH_dCOO) with a free energy barrier of 0.30 eV (TS1-2), however, the PDS of FAO is *mH_dCOO → $CO_2 + 2H^+ + 2e^-$ on the Mo_2Pd/LI (TS2-3, 1.09 eV) and Mo_3Pd/T (TS2-3, 1.23 eV). Direct dehydrogenation can take place O-H bond broken as the proton-electron pair transfer by water and C-H bond cleavage by the adoption on catalyst surface (TS4, 0.79 eV) lower on Mo_2Pd/LI (TS2-4, 0.97 eV) and Mo_3Pd/T (TS2-4, 1.00 eV). Mo1Pd has the lowest barrier for FAO on the explicit water model.

Remarkably, the calculated activation barriers of *bH_uCOO→ *mH_dCOO reduce proportionally with the enhanced oxyphilicity of alloyed Mo [45], using *OH BE as an indicator[40, 69] (Figure 5.6), thay have a volcano relationship. That is, the alloyed Mo with moderate-to-strong oxyphilicity would facilitate the decoordination of bidentate HCOO on M@Pd(111), nonetheless, the oxphilicity is too strong will enhance the BE of *mH_dCOO inhibition of further dehydrogenation. Therefore, BE is too strong or too weak lead to decreasing catalyst activity, the Mo1Pd exist the highest catalyst performance due to moderate BE of OH.

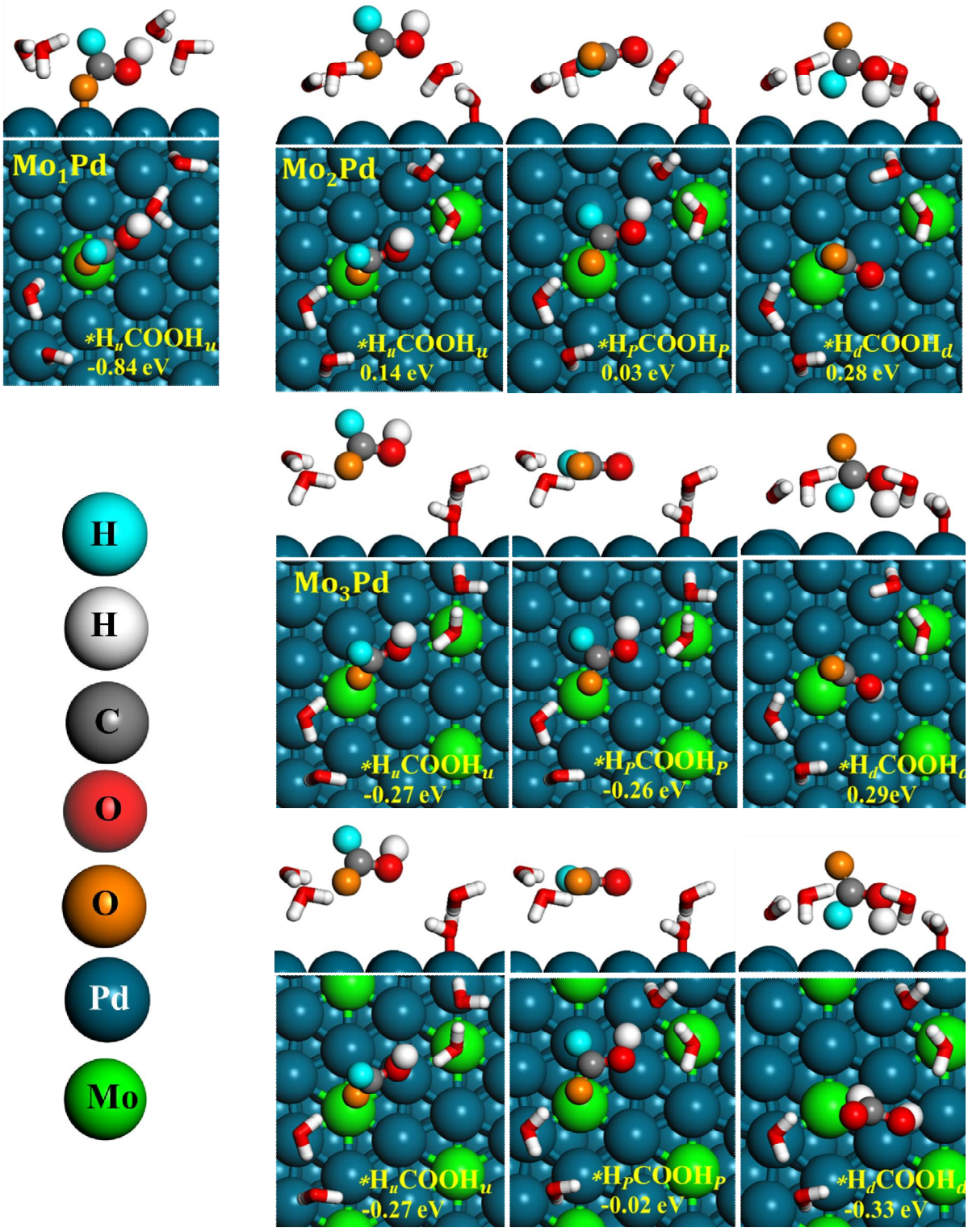

Figure 5.4 Optimized structures of *HCOOH adsorbed on Mo_1Pd, Mo_2Pd/DI, Mo_2Pd/LI, Mo_3Pd/T and Mo_4Pd. Binding energy (BE, in eV) of *HCOOH were marked.

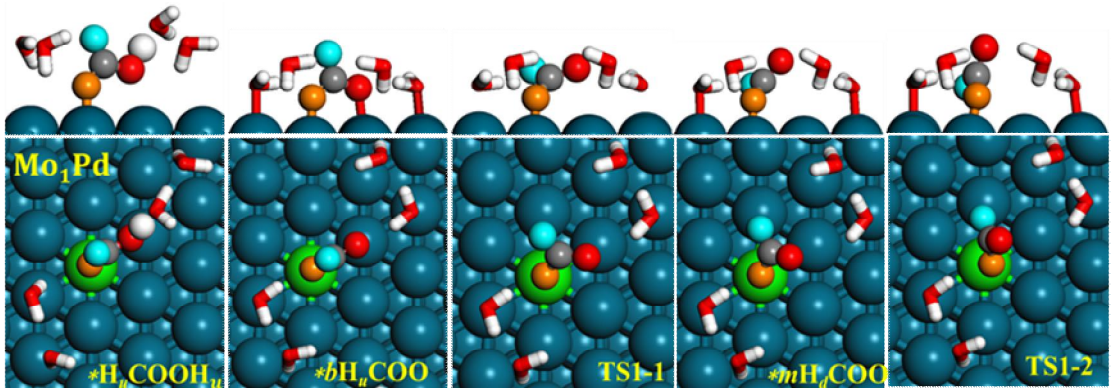
Mo1Pd
*HuCOOHu
*bHuCOO
TS1-1
*mHuCOO
TS1-2

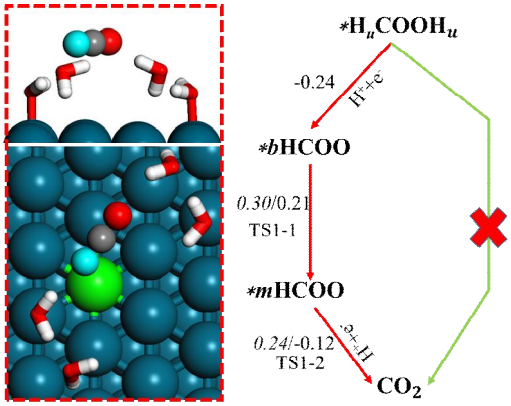
*HuCOOHu
-0.24
H++e
*bHCOO
0.30/0.21
TS1-1
*mHCOO
0.24/-0.12
TS1-2
2+H
CO2

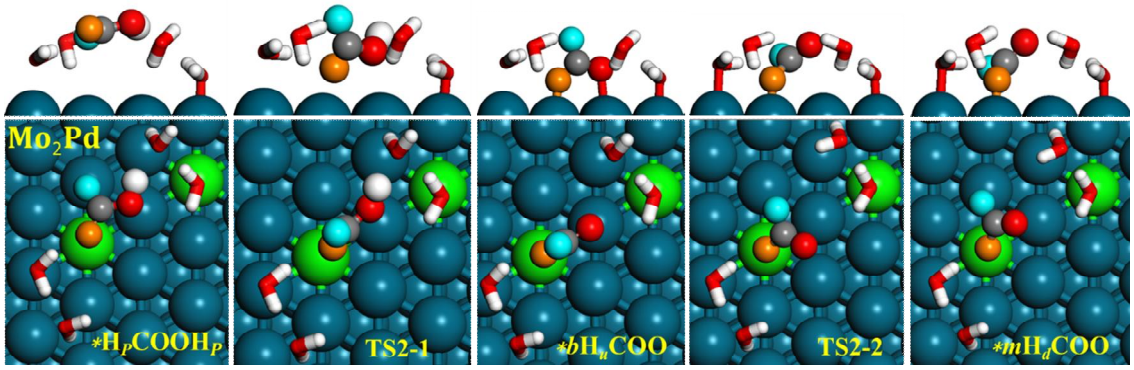
Mo2Pd
*HpCOOHp
TS2-1
*bHuCOO
TS2-2
*mHdCOO

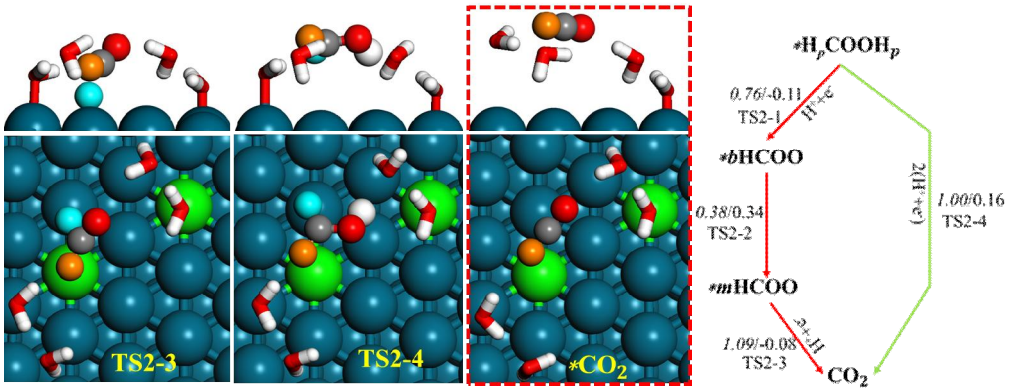
TS2-3
TS2-4
*CO2
*HpCOOHp
0.76/-0.11
TS2-1
H++e
*bHCOO
0.38/0.34
TS2-2
*mHCOO
1.09/-0.08
TS2-3
2+H
2(H++e)
1.00/0.16
TS2-4
CO2

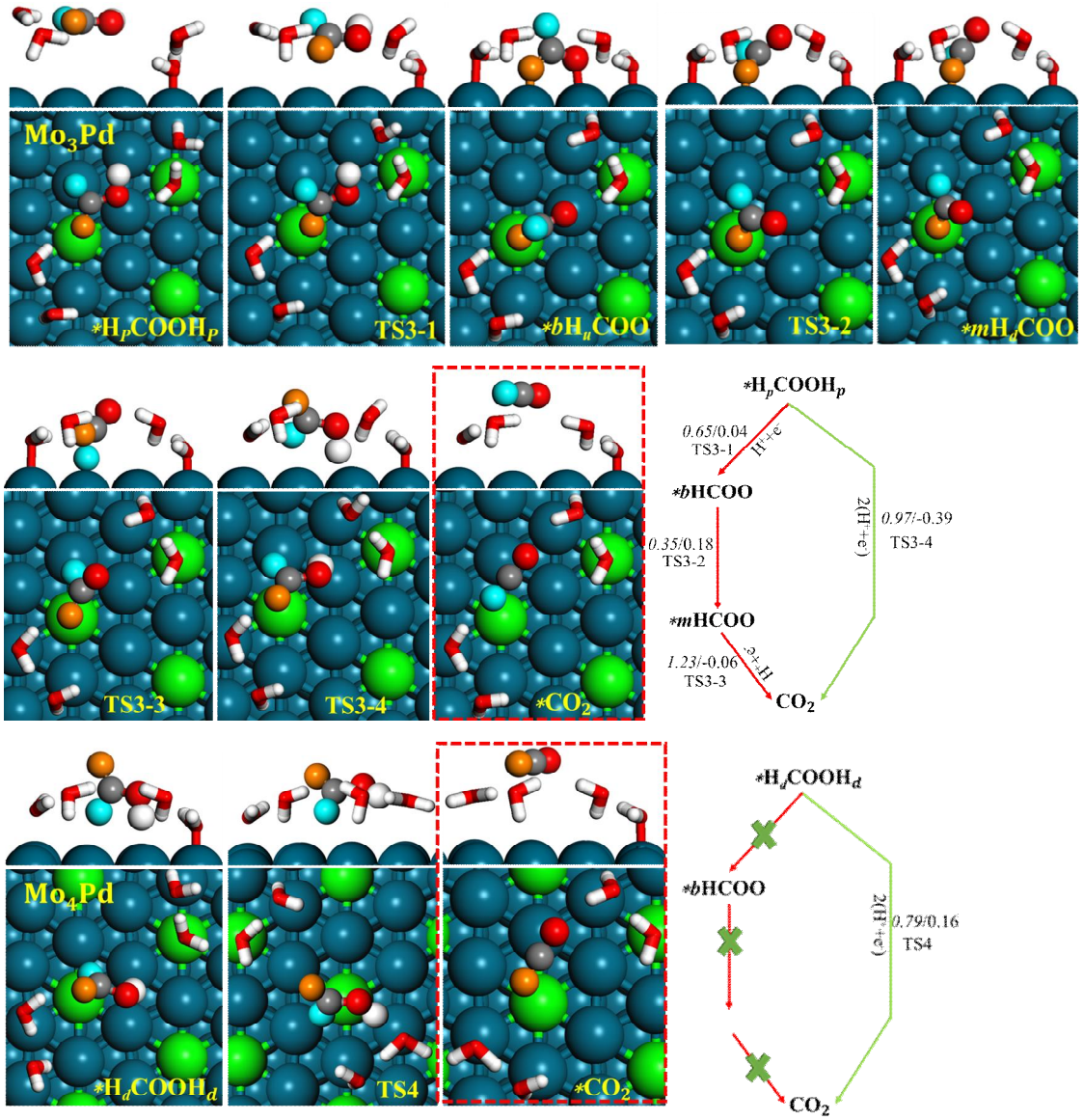

Figure 5.5 Optimized structures of *HCOOH adsorbed on (a) Ru@Pd(111) and (b) Pd(111). Binding energy (BE, in eV) of *HCOOH were marked.

Table 5.2 Binding energy (BE, in eV) of *HCOOH, *CO_2, *CO and *H_2O with most stable configuration on MoPd(111) calculated, where CO_2, CO were used their gas-phase and H_2O, HCOOH were used their aqueous phase as reference.

Catalyst	*HCOOH	*CO_2	*CO[a]	*H_2O
Mo_1Pd	-0.84	-0.12	-1.43	-0.27
Mo_2Pd/DI	-1.06	0.00	-1.46	-0.25
Mo_2Pd/LI	0.14	-0.54	-1.40	-0.24
Mo_3Pd	-0.27	-0.11	-1.40	-0.26
Mo_4Pd	-0.27	-0.14	-1.44	-0.27

[a]The most stable configuration of CO adsorption is 3-fold hollow of Pd-Mo-Pd.

Table 5.3 Binding energies (BE)[a] of the adsorbed species with the most stable configuration on Mo@Pd(111) calculated.

Catalyst	*HCOOH	*bH$_u$COO	*mH$_d$COO
Mo_1Pd	**-1.09**	-0.56	-0.25
Mo_2Pd/DI	**-1.32**	-0.64	X
Mo_2Pd/LI	-0.22	-0.58	-0.29
Mo_3Pd	-0.52	-0.66	-0.31
Mo_4Pd	-0.52	-0.71	X

[a]The Binding energies (BE) is defined as E[CHxOy] = E[CO_2] + [(4+x-2y)/2]*E[H_2] - (2-y)*E[H_2O], calculated using gas-phase CO_2, H_2 and H_2O energy as the reference.

Table 5.4 Zero-point energy (ZPE, in eV) and entropy corrections (TS, in eV) at T = 298.15 K for gaseous molecules.

Molecules	ZPE	TS
H_2	0.27	0.40
HCOOH	0.90	0.75
CO_2	0.30	0.14

Table 5.5 Zero-point energy (ZPE, in eV) and entropy corrections (TS, in eV) at T = 298.15 K for adsorbates.

Catalyst	*HCOOH		*bH$_u$COO		*mH$_d$COO	
	ZPE	TS	ZPE	TS	ZPE	TS
Mo_1Pd	0.85	0.13	0.59	0.13	0.56	0.10
Mo_2Pd/LI	0.90	0.16	0.59	0.19	0.56	0.10
Mo_3Pd	1.00	0.07	0.72	0.10	0.56	0.10
Mo_4Pd	0.90	0.16	-	-	-	-

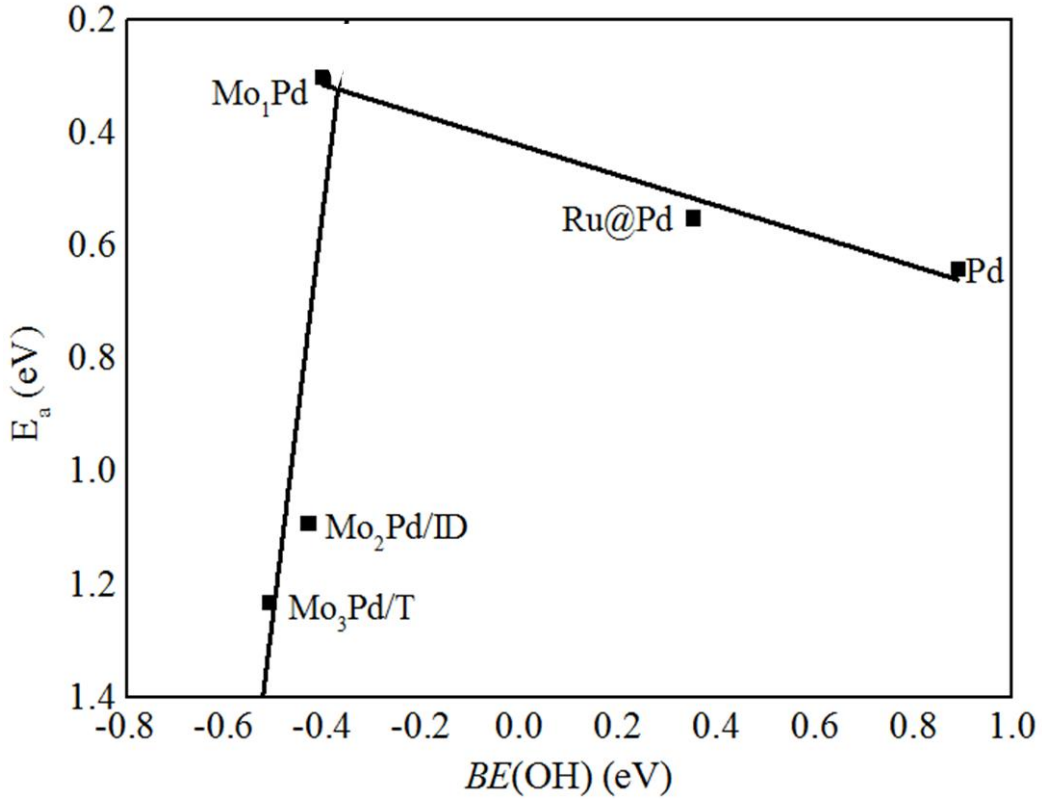

Figure 5.6 Correlation of activation energy (E_a) of PDS as a function of *OH binding energy (BE).

5.4 Conclusions

In this work, we theoretically investigated mechanism for FAO on MoPd alloy and the coverage degree is from 1/16ML to 4/16 ML. It is revealed that alloyed Mo atom can not only act as active site for FAO but also affect the reactivity of nearest-neighboring Pd atoms via the ligand effect (charge transfer). The decoordination of *HCOO from bidentate to monodentate adsorption mode (i.e., *bH$_u$COO→ *mH$_d$COO) followed by the facile carbonyl-H abstraction forming CO_2 + (H^++e^-) is identified as the PDS with a free energy barrier of 0.30 eV on Mo1Pd. The simulated polarization curves agree reasonably well with the experiment, showing Mo1Pd for promoting FAO via primarily the direct mechanism: HCOOH →*HCOO (formate) → CO_2 + 2H^+ + 2e^-. It is predicted that Mo1Pd owing to the modest oxyphilicity could be the most promising catalyst for FAO. As such, the binding strength *OH can be used as an effective descriptor of for fast screening of high-performance FAO catalysts. However, the coverage degree is up to 4/16 ML, the reaction route is changed as : HCOOH → CO_2 + 2H^+ + 2e^-.

REFRENCES

[1] X. Yu, P.G. Pickup, Recent advances in direct formic acid fuel cells (DFAFC), J. Power Sources, 182 (2008) 124-132.

[2] B.C. Ong, S.K. Kamarudin, S. Basri, Direct liquid fuel cells: A review, Int. J. Hydrogen Energy, 42 (2017) 10142-10157.

[3] Antolini., Ermete., Palladium in fuel cell catalysis, Energy Environ. Sci., 2 (2009) 915-931.

[4] K. Jiang, H.X. Zhang, S. Zou, W.B. Cai, Electrocatalysis of formic acid on palladium and platinum surfaces: from fundamental mechanisms to fuel cell applications, Phys. Chem. Chem. Phys., 16 (2014) 20360-20376.

[5] L. Sui, W. An, Y. Feng, Z. Wang, J. Zhou, S.H. Hur, Bimetallic Pd-Based surface alloys promote electrochemical oxidation of formic acid: Mechanism, kinetics and descriptor, J. Power Sources 451 (2020) 227830.

[6] A.O. Neto, M. Linardi, E.V. Spinacé, Electro-oxidation of ethylene glycol on PtSn/C and PtSnNi/C electrocatalysts, Ionics, 12 (2006) 309-313.

[7] S. Ueda, M. Eguchi, K. Uno, Y. Tsutsumi, N. Ogawa, Electrochemical characteristics of direct dimethyl ether fuel cells, Solid State Ion, 177 (2006) 2175-2178.

[8] F. Meng, M. Yang, Z. Li, R. Zhang, HCOOH dissociation over the Pd-decorated Cu bimetallic catalyst: The role of the Pd ensemble in determining the selectivity and activity, Appl. Surf. Sci., 511 (2020) 145554.

[9] P.N. Duchesne, Z.Y. Li, C.P. Deming, V. Fung, X. Zhao, J. Yuan, T. Regier, A. Aldalbahi, Z. Almarhoon, S. Chen, D.E. Jiang, N. Zheng, P. Zhang, Golden single-atomic-site platinum electrocatalysts, Nat. Mater., 17 (2018) 1033-1039.

[10] W. Zhong, Y. Qi, M. Deng, The ensemble effect of formic acid oxidation on platinum–gold electrode studied by first-principles calculations, J. Power Sources, 278 (2015) 203-212.

[11] W. Gao, J.A. Keith, J. Anton, T. Jacob, Theoretical elucidation of the competitive electro-oxidation mechanisms of formic acid on Pt (111), JACS, 132 (2010) 18377-18385.

[12] H.-F. Wang, Z.-P. Liu, Formic acid oxidation at Pt/H2O interface from periodic DFT calculations integrated with a continuum solvation model, J. Phys. Chem. C, 113 (2009) 17502-17508.

[13] W. Gao, J.E. Mueller, Q. Jiang, T. Jacob, The Role of Co‐Adsorbed CO and OH in the Electrooxidation of Formic Acid on Pt (111), Angew. Chem. Int. Ed., 51 (2012) 9448-9452.

[14] S. Meenakshi, K. Nishanth, P. Sridhar, S. Pitchumani, Spillover effect induced Pt-TiO2/C as ethanol tolerant oxygen reduction reaction catalyst for direct ethanol fuel cells, Electrochim. Acta, 135 (2014) 52-59.

[15] G. Kresse, J. Furthmüller, Efficient iterative schemes for ab initio total-energy calculations using a plane-wave basis set, Phys. Rev. B, 54 (1996) 11169-11186.

[16] G. Kresse, J. Hafner, Ab initio molecular dynamics for liquid metals, Phys. Rev. B, 47 (1993) 222-229.

[17] A. Rabis, P. Rodriguez, T.J. Schmidt, Electrocatalysis for polymer electrolyte fuel cells: recent achievements and future challenges, Acs Catalysis, 2 (2012) 864-890.

[18] G. Kresse, D. Joubert, From ultrasoft pseudopotentials to the projector augmented-wave method, Phys. Rev. B, 59 (1999) 1758-1775.

[19] P.E. Blöchl, Projector augmented-wave method, Phys. Rev. B, 50 (1994) 17953-17979.

[20] H.J. Monkhorst, J.D. Pack, Special points for Brillouin-zone integrations, Phys. Rev. B, 13 (1976) 1746-1747.

[21] G. Henkelman, B.P. Uberuaga, H. Jónsson, A climbing image nudged elastic band method for finding saddle points and minimum energy paths, J. Chem. Phys., 113 (2000) 9901-9904.

[22] A. Heyden, A.T. Bell, F.J. Keil, Efficient methods for finding transition states in chemical reactions: Comparison of improved dimer method and partitioned rational function optimization method, J. Chem. Phys., 123 (2005) 224101.

[23] G. Henkelman, H. Jónsson, A dimer method for finding saddle points on high dimensional potential surfaces using only first derivatives, J. Chem. Phys., 111 (1999) 7010-7022.

[24] G. Henkelman, A. Arnaldsson, H. Jónsson, A fast and robust algorithm for Bader decomposition of charge density, Comput. Mater. Sci, 36 (2006) 354-360.

[25] A.O. Elnabawy, J.A. Herron, J. Scaranto, M. Mavrikakis, Structure Sensitivity of Formic Acid Electrooxidation on Transition Metal Surfaces: A First-Principles Study, J. Electrochem. Soc., 165 (2018) J3109-J3121.

[26] J.K. Nørskov, J. Rossmeisl, A. Logadottir, L. Lindqvist, J.R. Kitchin, T. Bligaard, H. Jonsson, Origin of the overpotential for oxygen reduction at a fuel-cell cathode, J. Phys. Chem. B, 108 (2004) 17886-17892.

[27] H. Wang, W. An, Promoting the oxygen reduction reaction with gold at step/edge sites of Ni@AuPt core–shell nanoparticles, Catal. Sci. Technol., 7 (2017) 596-606.

[28] F. Alcaide, G. Álvarez, P.L. Cabot, H.-J. Grande, O. Miguel, A. Querejeta, Testing of carbon supported Pd–Pt electrocatalysts for methanol electrooxidation in direct methanol fuel cells, Int. J. Hydrog. Energy, 36 (2011) 4432-4439.

[29] J. Yang, L. Shi, X. Liu, Y. Wen, K. Cho, Y. Zhao, R. Chen, B. Shan, Unravelling origins of Pd ensembles' activity in CO oxidation via state-to-state microkinetic analysis, J Catal, 371 (2019) 276-286.

[30] J. Tayal, B. Rawat, S. Basu, Bi-metallic and tri-metallic Pt–Sn/C, Pt–Ir/C, Pt–Ir–Sn/C catalysts for electro-oxidation of ethanol in direct ethanol fuel cell, Int. J. Hydrog. Energy, 36 (2011) 14884-14897.

[31] Y. Feng, W. An, Z. Wang, Y. Wang, Y. Men, Y. Du, Electrochemical CO2 reduction reaction on M@ Cu (211) bimetallic single-atom surface alloys: mechanism, kinetics and catalyst screening, ACS Sustainable Chem. Eng., (2019).

[32] Y. Zhao, L. Fan, J. Ren, B. Hong, Electrodeposition of Pt–Ru and Pt–Ru–Ni nanoclusters on multi-walled carbon nanotubes for direct methanol fuel cell, Int. J. Hydrog. Energy, 39 (2014) 4544-4557.

[33] A. Cuesta, G. Cabello, M. Osawa, C. Gutiérrez, Mechanism of the Electrocatalytic Oxidation of Formic Acid on Metals, ACS Catal., 2 (2012) 728-738.

[34] J. Joo, T. Uchida, A. Cuesta, M.T. Koper, M. Osawa, Importance of acid-base equilibrium in electrocatalytic oxidation of formic acid on platinum, JACS, 135 (2013) 9991-9994.

[35] L. Xing, J. Jia, Y. Wang, B. Zhang, S. Dong, Pt modified TiO2 nanotubes electrode: preparation and electrocatalytic application for methanol oxidation, Int. J. Hydrog. Energy, 35 (2010) 12169-12173.

[36] W. Kohn, L.J. Sham, Self-consistent equations including exchange and correlation effects, Phys. Rev., 140 (1965) A1133.

[37] J.Y. Wang, H.X. Zhang, K. Jiang, W.B. Cai, From HCOOH to CO at Pd electrodes: a surface-enhanced infrared spectroscopy study, JACS, 133 (2011) 14876-14879.

[38] S. Hu, F. Che, B. Khorasani, M. Jeon, C.W. Yoon, J.-S. McEwen, L. Scudiero, S. Ha, Improving the electrochemical oxidation of formic acid by tuning the electronic properties of Pd-based bimetallic nanoparticles, Appl. Catal., B, 254 (2019) 685-692.

[39] H. Miyake, T. Okada, G. Samjeske, M. Osawa, Formic acid electrooxidation on Pd in acidic solutions studied by surface-enhanced infrared absorption spectroscopy, Phys. Chem. Chem. Phys., 10 (2008) 3662-3669.

[40] M.-S. Kim, B. Fang, N.K. Chaudhari, M. Song, T.-S. Bae, J.-S. Yu, A highly efficient synthesis approach of supported Pt-Ru catalyst for direct methanol fuel cell, Electrochim. Acta, 55 (2010) 4543-4550.

[41] L. Ou, J. Chen, Y. Chen, J. Jin, Mechanistic Study of Pt-Catalyzed Electrooxidation of HCOOH in Acid Medium: Kinetic Considerations on the Effect of Solvation, J. Phys. Chem. C, 122 (2018) 24871-24884.

[42] J.A. Herron, J. Scaranto, P. Ferrin, S. Li, M. Mavrikakis, Trends in Formic Acid Decomposition on Model Transition Metal Surfaces: A Density Functional Theory study, ACS Catal., 4 (2014) 4434-4445.

[43] Y. Wang, Y. Qi, D. Zhang, C. Liu, New Insight into the Decomposition Mechanism of Formic Acid on Pd(111): Competing Formation of CO2 and CO, J. Phys. Chem. C, 118 (2014) 2067-2076.

[44] W. Tokarz, G. Lota, E. Frackowiak, A. Czerwiński, P. Piela, Fuel cell testing of Pt–Ru catalysts supported on differently prepared and pretreated carbon nanotubes, Electrochim. Acta, 98 (2013) 94-103.

[45] R. Dillon, S. Srinivasan, A. Arico, V. Antonucci, International activities in DMFC R&D: status of technologies and potential applications,J. Power Sources 127 (2004) 112-126.